Design Principles for Nanocrystal Assembly Using Anisotropic Building Blocks

by

William E. Zygmunt

A dissertation submitted in partial fulfillment
of the requirements for the degree of
Doctor of Philosophy
(Chemical Engineering)
in The University of Michigan
2020

Doctoral Committee:

Professor Sharon C. Glotzer, Chair
Professor Greg van Anders
Professor Nicholas A. Kotov
Professor Xiaoming Mao
Professor Robert M. Ziff

William E. Zygmunt

wzygmunt@umich.edu

ORCID iD: 0000-0001-6631-3307

For mom and dad.

ACKNOWLEDGEMENTS

I would first like to thank my advisor, Sharon C. Glotzer, whose extensive knowledge helped me to direct and focus my research into new frontiers. Your expertise and boundless excitement for scientific discovery inspired me to create good science. I also want to thank my committee for all of their feedback on my research: Professors Nicholas A. Kotov, Xiaoming Mao, Robert M. Ziff and Greg van Anders, who also worked with me on my first publication and whose mentorship helped me to get started in the group. Josh Anderson, thanks for helping me refine my research and for helping me think about better ways to write my simulations. Karen Coulter, thanks for everything you did to keep me moving in the right direction, your management skills are legendary. I would also like to thank Dr. Jeffrey Potoff, who gave me the opportunity to do research for the first time, it seems like doing simulations was the right direction after all!

There are so many great people in this group who I have had the pleasure to have known over the past five years. Erin Teich, thanks for being my friend, you made my first year much easier and I appreciate your mentorship. Thi Vo, with whom discussions improved my scientific process and helped me to think in the larger scale of things, thanks for helping me become a better scientist and for being a great friend. Shannon Moran, grad school would have been much harder without your brightness and friendship to help carry me through hard days. Now that my thesis is complete,"Polo". Vyas Ramasubramani and Luis Rivera-Rivera, it was fun having

you both in my graduating class, and thanks for always being there to help me do better science.

Graduate school is a long, very hard journey, and I was lucky to have many people supporting me! Emily Moran, I love you very much and I am forever grateful to be able to come home after a long day of research to spend it with you. Tim Zygmunt, you're the best brother a guy could ask for, thanks for being my best friend and for always being there for me. Mom and dad, you raised me to be a scientist, and look where I am now! Thank you both for inspiring me and elevating me to my full potential. I have too many good friends to name them all here, but thank you all for listening to me when I needed it and making me laugh when I needed it more.

TABLE OF CONTENTS

LIST OF FIGURES

ABSTRACT

Self-assembly of soft matter is a phenomena that can be influenced by multiple factors including particle shape, ligand decoration and thermodynamic properties such as temperature and pressure. In this highly anisotropic landscape of particle properties, it is crucial to understand the set of attributes that can contribute to the self-assembly of nanomaterials with novel physical properties including photonic and plasmonic response to be utilized in materials application.

We determine and then employ different set of design rules that allow us to govern the nanoarchitecture that results from the assembly. We demonstrate that topologically protected colloidal matter at maximum pressure preserves topological order that can persist when no longer at maximum pressure, and that this is general to systems that can be described via topological sets of nanoparticle packings. We also show that the self-assembly of regular, patchy polygons with highly anisotropic patch distribution can be controlled into selecting specific desired morphologies with novel void shape, and that hierarchical self-assembly can be applied for even more complicated structures. Lastly, we show how ligand architecture can control the self-assembly behavior of nanoplates, and that ligand coated nanoplates can have controllable orientation in the plane when subjected to similar ligated cubes. This dissertation delivers roadmaps for the rational design of specific and highly targeted materials with tunable physical features and will help to realize new materials with complex order in experiment.

CHAPTER I

Introduction

1.1 Self-Assembly of Nanoparticles

Self-assembly is the process under which nanoparticles spontaneously order themselves into organized crystalline structures with long-range translational and/or rotational order. Recent developments in the ability to tune particle size, shape and surface interaction [4] have allowed for the employment of many different building blocks to be utilized in studies of self-assembly, characterized along a series of alchemical dimensions [1]. In this dissertation, I will explore the affect of various anisotropy dimensions on the assembly of nanoparticles, including faceting (Chapters 2 and 3), patchiness (Chapters 3, 4, 5) and variations in ligand architecture (Chapters 4 and 5).

Hard particles are particles that interact through volume exclusion alone (i.e. particles are not allowed to overlap with one another). Hard particles of many different geometries have been synthesized in experiment [5, 6, 7] and can be packed into their densest packing at high pressure [2], leading to their usage in material applications such as plamonics [8]. When systems of hard particles becomes sufficiently dense, particles seek to maximize their entropy and spontaneously self-assemble into crystalline structures [9, 10], and such mechanisms have been shown to be unrelated to

their packing phase [11].

Patchy particles are a class of materials that harbor interactions between designated sites on the particle surface, where highly-directional interactions can be programmed for complex interaction [12]. Patches may be entropic [13] in the sense that particles will tend to align along larger facets (entropic patches) or enthalpic, where patches are made up of some surface functionalization via DNA [14, 15], polymers [16, 17], or other material [18]. Patchy particles in the past were typically described as spheres [19], particularly the Janus particle [20] which is named for the two-faced Roman god Janus since it has two faces, one hydrophobic and one hydrophilic, but in reality, any shape can be enthalpically patchy if decorated with some complex interaction [21, 22, 23]. Patchy particles are useful in many applications due to their highly-directional nature and can be used to target porous structures which can be used in photonics applications [24], gas storage materials [25], molecular sieves [26, 27] and many others.

1.2 The Need for Design Rules

Given that there is such an expansive space of potential nanocrystalline candidates to be considered, scientists are always looking for ways to filter out the search space for material candidates that will assemble crystals with their desired properties. Studies of the self-assembly of hard polyhedra [28] showed that the different assembly categories (liquid crystals, plastic crystals, crystals and disordered phases) could be predicted via calculable parameters of the particles themselves, such as the fluid phase coordination number CN_f and the isoperimetric quotient IQ. This work investigated 145 convex polyhedra and showed that that by using these parameters, polyhedra could be grouped into such categories. In another work [2], the densest

packing of several truncation families of similar polyhedra was studied, which allowed for the determination of different densely packed phases solely based on the shape truncations applied to cubes, octahedrons, etc. The same families were studied in the assembly limit [29] and showed that different crystalline phases (FCC, BCC, etc.) could be predicted from shape truncations as well. The anisotropy dimension considered here is faceting alone, since these materials do not require ligands or other decoration to be assembled in experiment [5].

Nanoparticle self-assembly can become far more complicated when extra anisotropy dimensions are introduced, especially if assembly becomes highly dependent on two or more dimensions. Figure 1.1 demonstrates some of the different anisotropy dimensions that could be considered and how they could potentially be combined into a large design space. One example of a complicated design space is the self-assembly of DNA grafted nanoparticles into superlattices where the final lattice might have particles of different sizes, lattice spacing or crystallographic symmetry. Design rules were developed [30] which consider factors such as the hydrodynamic radii, nanoparticle core radii and the DNA linker ratio between two sets of nanoparticles sharing a DNA bond which allow for the assembly of nine distinct colloidal crystal structures. Many nanoparticles possess anisotropic cores which can have odd or complex geometry but additionally have ligands which surround the core to facilitate the bonding to other nanoparticles, which makes this design rule approach relevant and useful.

In this dissertation, we demonstrate work that takes advantage of the natural intersection of different anisotropy dimensions that occur when considering the packing/assembly of nanoparticles. In Chapter 2, we demonstrate design rules that take advantage of the topological nature of the densest packing of nanoparticles in order to stabilize their crystalline order against thermal fluctuation. In this work, the
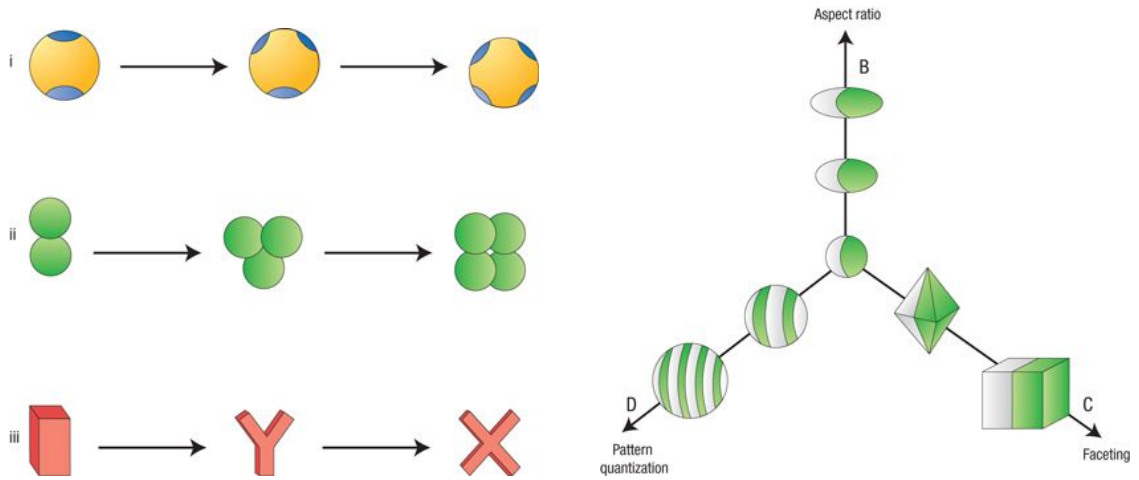
Figure 1.1: Different anisotropy axes all demonstrating branching (patchiness (i), roughness (ii), faceting (iii) (left)). Anisotropy space combining three different measures of anisotropy (right). Image reproduced from [1].

anisotropy dimensions are simple (two axes of faceting) and define the construction of all packing structures considered in the work. In Chapter 3, we consider nanoplates consisting of regular polygons, decorated with various edge-patterning representing A-B attraction of short ligands, and demonstrate that they can be assembled into a wide variety of different morphology. This represents a combination of two anisotropy dimensions, faceting and patchiness, but one could imagine expanding such a space to include varied ligand design, including length and bulkiness. Chapter 4 considers the effect of ligand bulkiness explicitly on rhombic nanoplates and demonstrates that ligand design can effect the partitioning of ligands onto a nanoparticle surface and control the final layer-by-layer morphology. Finally, Chapter 5 demonstrates that one can use inverse design to investigate the effect of ligand architecture on the self-assembly of binary systems, and then use that information to target complex co-assembly of these species.

CHAPTER II

Topological Order in Densely Packed Anisotropic Colloids

This chapter is adapted from Ref. [31], a publication in Physical Review E, authored in 2019 by W. Zygmunt, E. G. Teich, G. van Anders and S. C. Glotzer.

2.1 Introduction

Topological phases are exotic states of matter that are typically associated with strongly interacting quantum systems, in which topological protection stabilizes certain physical behaviors against environmental perturbations [32]. In quantum systems, protection of this type can be invaluable in applications for which coherence is crucial. In a similar spirit, many applications for classical soft matter systems of colloidal nanoparticles would benefit from topological order in the presence of environmental perturbations. In colloidal systems, entropic effects are important [10, 29, 33] and typical interaction strengths are on the order of the thermal scale. Indeed, recent work has shown that thermal fluctuations in soft systems can, in a variety of contexts, drive structural reconfiguration [34, 35, 36, 37], an important feature of functional nanomaterials. However, for other applications, the preservation of structural order against thermal fluctuations is vital. If soft matter was topologically ordered, it could be used in building structures with robust features.

Recent work [38] has shown that topological states can exist in specialized clas-

sical mechanical systems, and that the dynamics of classical systems can manifest topological effects [39, 40]. The topological states that occur in those systems are expressed in terms of Witten indices, whose existence relies on the spectrum of excitations in nearly-isostatic lattices. Additionally, topologically protected phases exist in a variety of classic phononic [41, 42, 43, 44, 45, 46] and photonic [47] systems.

Here, we show that the point-set topology of contacts that distinguishes structures of hard colloids at infinite pressure (aka "putative densest packings") [2] leads to the existence of topologically distinct phases. We prove perturbatively that, in general, topologically distinct putative densest packings lead to the existence of associated thermodynamic phases away from infinite pressure. We demonstrate numerically that topological order persists at finite pressure. Surprisingly, we find that thermodynamic phases that are topologically protected at the highest possible packing densities preserve near-perfect topological order at packing densities sufficiently low that topological protection need not persist.

Our approach provides a general framework for investigating and classifying the structure of thermodynamic systems of hard colloids near the dense packing limit. The topological order we observe is of a strikingly different origin – and consequently, has different properties – than topological states in quantum matter. Ref. [38] showed that the existence of topological phases is not uniquely the preserve of strongly interacting quantum matter, and our results raise the possibility that topological order is a widespread phenomenon in classical systems.

2.2 Analytical First-Order Phase Transition at Infinite Pressure

Ref. [2] showed that, for families of hard anisotropic shapes at infinite pressure, continuous deformations of particle shape result in continuous changes in putative
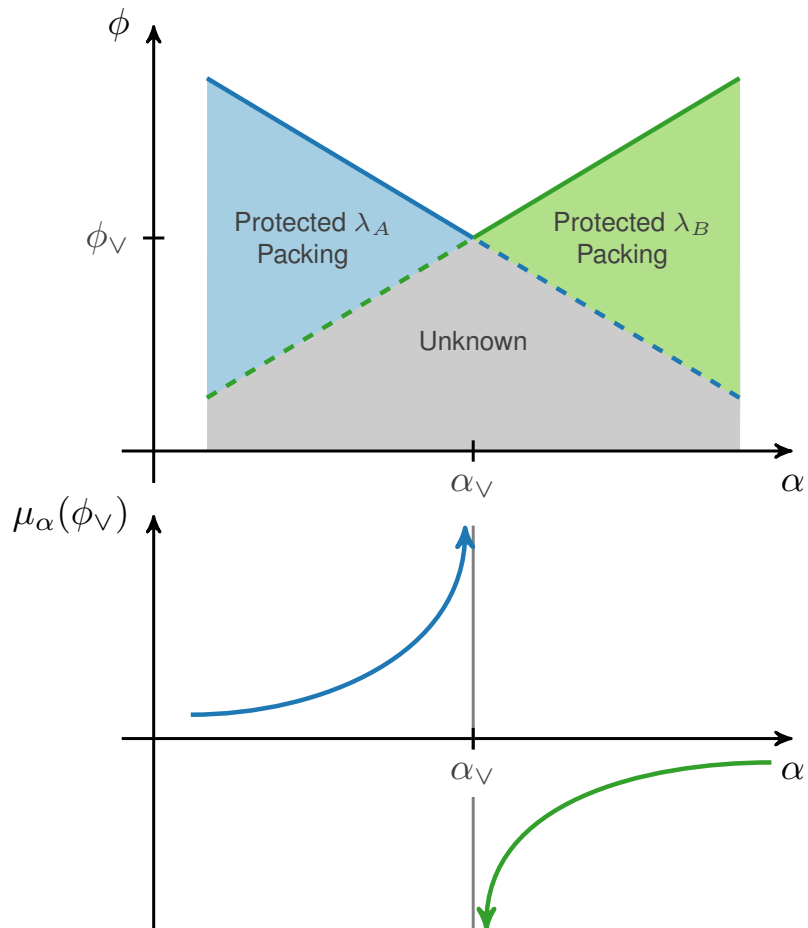
Figure 2.1: Surfaces (solid blue and green lines) of maximal packing density (ϕ_d) as a function of particle shape (α) have been shown [2], in general, to exhibit non-analytic behavior at the point ($\alpha_\vee, \phi_\vee$) that is associated with a change in the topology of contacts between adjacent particles. Within the blue and green triangular regions, dense packings exhibit topological distinction by particle contacts. However, within the gray region bounded above by the dashed blue and green lines, it is unknown, in general, whether topological contact types persist (top panel). We show that there is a first-order phase transition, indicated by the divergence of the so-called alchemical potential [3] near the valley packing discontinuity (bottom panel).

densest packings. It was also shown that non-analytic behavior in curves, surfaces, or hypersurfaces $\phi_d(\alpha_i)$ of maximal packing density ϕ_d as a function of particle shape α_i occur if and only if there is a change in the point-set topology of contacts between particles in the dense packing structure; Figure 2.1 illustrates this point. We argue that, generically, this leads to distinct, solid thermodynamic phases away from infinite pressure. Since pressure is defined in units of $k_B T$, we can think of the infinite pressure limit as a sort of zero temperature limit of the system, which may be a more useful way to think about these hard particle systems in reference to other works involving topological order. Note that the focus of this analysis is to draw a distinction between adjacent solid phases, rather than on the existence of distinct solid and liquid phases.

We make our argument using the framework of digital alchemy [3]. Digital alchemy extends the traditional thermodynamic ensemble for particle self-assembly through consideration of thermodynamically conjugate variables (termed "alchemical potentials" μ) coupled to changes in particle attributes. Here, we consider changes in particle shape as the alchemical variable for the packings in [2] and the associated alchemical potential is given by

$$(2.1) \qquad\qquad \mu_\alpha = \frac{1}{N}\frac{\partial F}{\partial \alpha} \ ,$$

where N is the number of particles in the system, F is the free energy, and α is a shape parameter. To understand the phase behavior of dense suspensions of anisotropic colloids away from infinite pressure, it is convenient to study the alchemical potential in the vicinity of the intersection of two packing curves, where there is a change in the topology of particle contacts ($\alpha_\vee, \phi_\vee$ in Figure 2.1).

It was previously shown [2] that for generic, anisotropic colloids, each fragment of the dense packing surface is a topologically distinct packing. We will assert that

in each topological equivalence class of packings there are the same number of "microstates" or entropy. This is a reasonable assumption because in most cases there is only one topologically allowed dense packing, and in the cases where there are sliding surfaces, the sliding surfaces should be topologically equivalent. We assume that, for some shape with alchemical parameter α describing the particle shape, there is a densest packing ϕ_d. We can find the free energy at a lower packing density ϕ via thermodynamic integration according to

$$(2.2) \qquad F(\phi, \alpha) = F(\phi_d(\alpha), \alpha) - \int_{\phi}^{\phi_d} d\phi' \frac{\partial F(\phi', \alpha)}{\partial \phi'}.$$

Using the relationship between packing density and volume, and the definition of pressure, this can be written as

$$(2.3) \qquad F(\phi, \alpha) = F(\phi_d(\alpha), \alpha) - \int_{\phi}^{\phi_d} d\phi' \frac{N\ell^d P(\phi')}{\phi'^2},$$

where ℓ is a characteristic length scale for the system, which we take to be the particle size, and assume that changes in α preserve the particle volume. For convenience, we will take $P^* = \ell^d \beta P$ to be the dimensionless pressure (where β is inverse temperature).We decompose the free energy into the kinetic part and the configurational part. We assume that the configurational part $\tilde{F}(\phi_d(\alpha), \alpha)$ is constant along a single topological family of packings, and the kinetic part F_k does not depend on density, so that

$$(2.4) \qquad F(\phi, \alpha) = F_k(\alpha) + \tilde{F}(\phi_\vee, \alpha_\vee) - \int_{\phi}^{\phi_d} d\phi' \frac{N P^*(\phi')}{\beta \phi'^2},$$

where we are following the notation of [3] for decomposing the free energy into kinetic and configurational parts [1]. Take $\Delta\alpha$ as the range over which the packing is optimal,

---

[1]Strictly, $\tilde{F}$ should be evaluated at $\phi_d(\alpha_\vee^-), \alpha_\vee^-$ because the free energy of the packing at $\alpha_\vee^+$ might be different; we use $\tilde{F}(\phi_\vee, \alpha_\vee)$ for convenience.

and also take $\delta\alpha$ so that

$$(2.5) \qquad\qquad 0 < \delta\alpha \ll \Delta\alpha.$$

We then approximate $F(\phi_\vee, \alpha_\vee - \delta\alpha)$ using the midpoint rule as

$$(2.6)\quad F(\phi_\vee, \alpha_\vee - \delta\alpha) \approx F_k(\alpha_\vee - \delta\alpha) + \tilde{F}(\phi_\vee, \alpha_\vee) - \frac{N(\phi_d - \phi_\vee)}{2\beta}\left(\frac{P^*(\phi_d)}{\phi_d^2} + \frac{P^*(\phi_\vee)}{\phi_\vee^2}\right)$$

where ϕ_d is evaluated at $\alpha_\vee - \delta\alpha$. We can approximate

$$(2.7) \qquad\qquad \phi_d(\alpha_\vee - \delta\alpha) - \phi_\vee \approx \delta\alpha\left.\left|\frac{\partial\phi_d}{\partial\alpha}\right|\right|_{\alpha=\alpha_\vee}$$

so that

$$
\begin{aligned}
(2.8)\quad F(\phi_\vee, \alpha_\vee - \delta\alpha) \approx & F_k(\alpha_\vee - \delta\alpha) + \tilde{F}(\phi_\vee, \alpha_\vee) \\
& - \frac{N\delta\alpha}{2\beta}\left.\left|\frac{\partial\phi_d}{\partial\alpha}\right|\right|_{\alpha=\alpha_\vee}\left(\frac{P^*(\phi_d)}{\phi_d^2} + \frac{P^*(\phi_\vee)}{\phi_\vee^2}\right).
\end{aligned}
$$

We can estimate the alchemical potential in the limit that α approaches $\alpha_\vee$ from the left as

$$
\begin{aligned}
(2.9)\quad \mu_\alpha \approx & \frac{1}{N\delta\alpha}\Big(F_k(\alpha_\vee) - F_k(\alpha_\vee - \delta\alpha) \\
& + \frac{N\delta\alpha}{2\beta}\left.\left|\frac{\partial\phi_d}{\partial\alpha}\right|\right|_{\alpha=\alpha_\vee}\left(\frac{P^*(\phi_d)}{\phi_d^2} + \frac{P^*(\phi_\vee)}{\phi_\vee^2}\right)\Big)
\end{aligned}
$$

so that

$$(2.10) \qquad \mu_\alpha \approx \frac{1}{N}F_k'(\alpha_\vee) + \frac{1}{2\beta}\left.\left|\frac{\partial\phi_d}{\partial\alpha}\right|\right|_{\alpha=\alpha_\vee}\left(\frac{P^*(\phi_d)}{\phi_d^2} + \frac{P^*(\phi_\vee)}{\phi_\vee^2}\right).$$

The first term in Eq. 2.10 is a correction factor that comes from differentiating the trace of the moment of inertia tensor. As long as the shape parametrization is continuous, this term is finite and in [2] it certainly always is. However, $P^*(\phi_d)$ is formally infinite. That means $\mu_\alpha \to \infty$ as $\alpha \to \alpha_\vee^-$. If we carry out the same consideration for $\alpha_\vee + \delta\alpha$ everything carries through up to Eq. 2.10, except that the

sign of the second term is reversed. This means $\mu_\alpha \to -\infty$ as $\alpha \to \alpha_\vee^+$. A sketch of this result is in Figure 2.1.

μ_α is a first derivative of the free energy, which means that $\phi_\vee, \alpha_\vee$ is a first order thermodynamic phase transition. Another way of seeing this is the fact that the alchemical potential diverges near $\alpha_\vee$, meaning that at $\phi_\vee$ for any finite alchemical potential the system will have a thermodynamically preferred α that is a finite distance from $\alpha_\vee$. This means that if we regard α as an order parameter, there is no way at $\phi_\vee$ of having it take the value of $\alpha_\vee$, so that it must change discontinuously. We note that μ_α can also be interpreted as a stress that results from a strain $d\alpha$ [3]. This transition exists solely because of the non-analytic behavior of the dense packing surface, which reflects the topology of contacts among densely packed particles.

2.3   Delineation of Topological Phases

Next we consider what happens below maximum packing density. We consider packings λ_i where $i \in \{A, B\}$; λ_A and λ_B are on either side of the phase transition shown schematically in Figure 2.1. To distinguish between these packings, we construct an order parameter that takes advantage of the way λ_A and λ_B are defined topologically. Ref. [2] defines each packing according to the types of contacts (face-face, face-vertex, face-edge, vertex-vertex, vertex-edge and edge-edge) shared between adjacent particles. These contacts map to a set of intersection equations that mathematically describe each contact by relating particle shape parameters to the geometry of the two particle unit cell of the packing, described by vectors for the lattice and particle(s) within the unit cell. Each packing λ_i has K_i unique (meaning unshared with the other packing) intersection inequalities $|C_{i,k}| \geq 0$ (where $k = 1, 2, \ldots, K_i$) that define the packing. As an example, a packing λ_A might be

described by a relation $C_{A,1} = [a \cdot < -1, 1, 1 > -(\alpha_a + \alpha_c)]$, where a is a lattice vector and α_a and α_c are parameters that describe particle shape. Note that the range of parameters could include any lattice vector (a, b, c), the displacement vector between the two particles in the unit cell (d), or any of three shape parameters $(\alpha_a, \alpha_b, \alpha_c)$. Three shape parameters fully characterize the family of particle shapes [2] considered in this paper; we describe them fully in the next section.

When the shape parameters and unit cell geometry correspond to densest packing, all the $C_{i,k} = 0$. If the geometry of the unit cell does not correspond to the densest packing, then some $|C_{i,k}| \geq 0$. Changes in unit cell geometry (while particle shape is fixed) effectively provide a means of measuring changes to particle contact; at lower packing densities, then, the saturation or near-saturation of the intersection inequalities (i.e. all $C_{i,k} \approx 0$) would imply that particle contacts have (through thermal fluctuation) remained approximately equal to the particle contacts at infinite pressure, preserving unit cell geometry and topological order.

We now define an order parameter of the form θ_{ij} where i represents a stable or metastable thermodynamic phase that is putatively isostructural with λ_i [2] and λ_j is the packing against which the state will be evaluated. For example, θ_{AA} is defined as the evaluation of a packing λ_A in its own intersection equations (those of λ_A), and it evaluates to unity at maximal packing density by construction. Conversely, θ_{AB} (pertaining to the same packing λ_A evaluated in the intersection equations of λ_B) evaluates to zero at maximal packing by construction.

To construct θ_{ij}, several variables must first be defined. The packing λ_i is a function of particle shape α and packing density $\phi \leq \phi_d$ by definition. We define ξ_{ij} (a function of particle shape α and packing density ϕ) to reflect the evaluation of

---

[2]Note that if subsequent evaluation of the order parameter indicates the state is not isostructural with λ_i it implies those structures are thermodynamically unstable

packing λ_i in the intersection equations of packing type λ_j as

$$(2.11) \qquad \xi_{ij}(\phi, \alpha) = e^{-\frac{1}{K_j} \sum_{k=1}^{K_j} \left| C_{j,k}(\lambda_i(\phi,\alpha)) \right|}.$$

When $\phi = \phi_d$, ξ_{ij} describes the saturation of λ_j's intersection equations by λ_i at its maximum packing density, lying on its putative densest packing surface. We thus denote this special case by

$$(2.12) \qquad \xi_{ij}^{\text{ideal}} = \xi_{ij}(\phi_d, \alpha).$$

To construct a generalized order parameter for a set of two adjacent packings λ_A and λ_B, we then compute four quantities $(\xi_{AA}, \xi_{AB}, \xi_{BA}, \xi_{BB})$ that consider all four evaluation types in $i \in \{A, B\}$ and $j \in \{A, B\}$, which we use to build vectors that represent coordinates in the $[\xi_{iA}, \xi_{iB}]$ plane

$$(2.13) \qquad \mathbf{D_A} = \left[\xi_{AA}, \xi_{AB} \right] \quad , \quad \mathbf{D_B} = \left[\xi_{BA}, \xi_{BB} \right].$$

Similarly, we construct vectors to represent the maximum density packings

$$(2.14) \qquad \mathbf{D_A^{ideal}} = \left[\xi_{AA}^{\text{ideal}}, \xi_{AB}^{\text{ideal}} \right] \quad , \quad \mathbf{D_B^{ideal}} = \left[\xi_{BA}^{\text{ideal}}, \xi_{BB}^{\text{ideal}} \right].$$

The distance between the ideal structures in the $[\xi_{iA}, \xi_{iB}]$ plane is

$$(2.15) \qquad \mathbf{D_{AB}^{ideal}} = \sqrt{(\mathbf{D_A^{ideal}} - \mathbf{D_B^{ideal}}) \cdot (\mathbf{D_A^{ideal}} - \mathbf{D_B^{ideal}})}.$$

Finally, we define θ_{ij} to distinguish the topology of the two packings, making a generalized expression for any packing λ_i evaluated in the intersection equations of a packing type λ_j

$$(2.16) \qquad \theta_{ij} = 1 - \frac{\sqrt{(\mathbf{D_i} - \mathbf{D_j^{ideal}}) \cdot (\mathbf{D_i} - \mathbf{D_j^{ideal}})}}{\mathbf{D_{AB}^{ideal}}}.$$

Since we do not have a method to directly measure the topological invariant of a packing, we use our order parameter to estimate topological order of a packing λ_i

being evaluated using the intersection equations of a packing type λ_j. We find that our order parameter, in some specific packings, can tend to underreport topological order by a small amount but visual inspection confirms that the same contacts still manifest themselves in these packings. Since we are trying to show the mere existence of topological order in these systems, a slight underreport does not affect our overall conclusions.

2.4 Numerical Methods

Topologically distinct packings can be found for a range of families of anisotropic colloids. For concreteness, we considered packings in the two-parameter family of triangle invariant polyhedral shapes, Δ_{323}, reported in Ref. [2]. This family of shapes includes three Platonic solids (tetrahedron, octahedron, cube) and truncations thereof. The family can be described by two independent shape parameters, α_a and α_c (following the convention of [37]), denoting shape edge truncation and vertex truncation respectively. In [2], these variables are instead called u and v respectively. A third shape parameter that appears in the intersection equations, α_b, is equal to 1 in this shape family. Authors in [2] showed the existence of 75 topologically distinct two-particle dense packings of polyhedra in this family. This family has the largest number of closely spaced packings, which one might expect could reduce stability, making this set of systems a suitable candidate for investigating stability. Also, because the number of adjacent packing states is too large to study exhaustively, we arbitrarily chose two for extensive study. We chose two distinct packing boundaries (valleys which have a packing λ_i on either side, where $i \in \{A, B\}$), with one boundary (I) located between phases labelled '52' and '58' and the other boundary (II) between phases labelled '74' and '69' (numbering convention can be found in Ref.

[2]).

For each boundary, we chose one shape parameter (either α_a or α_c) to remain constant, and then moved along the axis of the other α. For boundary I, we studied a range of constituent particles in $\alpha_a = [2.80, 2.88]$ and set $\alpha_c = 1.52$ (the difference in topology of these packings is shown in Figure 2.2). In the packing labelled '52', both particles in the unit cell have a coordination number of 14 (coordination numbers were measured using the particles located in the first nearest neighbor shell), across the range of α_a studied. Similarly, in the packing labelled '58', both particles in the unit cell have a coordination number of 14, across the range of α_a studied. For boundary II, we set $\alpha_a = 1.80$ and studied a range of constituent particles in $\alpha_c = [1.90, 1.96]$ (the difference in topology of these packings is shown in Figure. 2.3). In the packing labelled '74', both particles in the unit cell have a coordination number of 12, across the range of α_c studied. However, in the packing labelled '69', both particles in the unit cell have a coordination number of 12 near $\alpha_c = 1.90$ but eventually have a coordination number of 13 near $\alpha_c = 1.96$.

We initialized systems of 1024 identical particles in both λ_A and λ_B at various densities. Particle positions and orientations were well defined for initialization in [2]. We sampled systems in the isochoric ensemble using the hard particle Monte Carlo (HPMC) [48] extension of the simulation toolkit HOOMD-blue [49, 50]. Although the volume remained fixed, box shear and aspect ratio moves were allowed, and move sizes were tuned such that acceptance ratios were approximately 0.3. We computed pressure during these simulations via the scaled distribution function [51], whose measurement is implemented in HPMC [48]. Ensemble averages were taken over five replicates and five snapshots per replicate simulation, where each simulation snapshot was separated by 10^6 MC timesteps, well beyond the calculated autocorrelation time
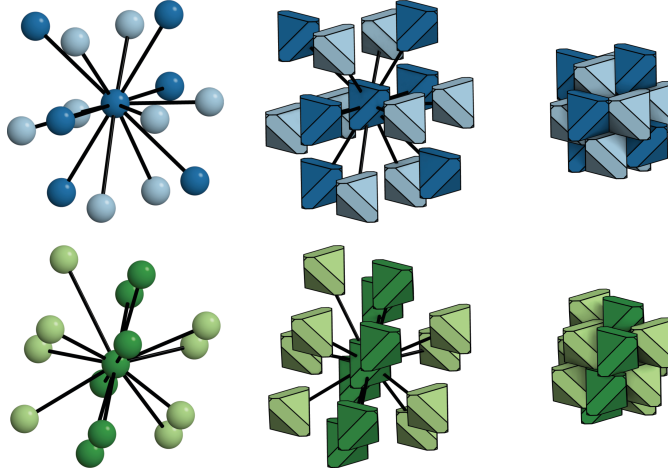
Figure 2.2: Example dense packing structures (where packing $\lambda_{A=52}$ is blue and packing $\lambda_{B=58}$ is green) of anisotropic shapes, including "exploded" views that show the location and orientation of neighboring particles, and densely packed units.

of the system pressure. For each data point, we constructed a system in the ideal putative densest packing structure and then expanded this structure to the target packing density.

Free energies were computed via the Frenkel-Ladd [52, 53] method. The Einstein crystals for these simulations were the same packings described above, with an expansion performed down to the desired packing density at the beginning of the simulation. An external force field Λ tethered particles to their crystal sites with a spring constant of $k = \exp(25)$ in units of $k_B T$. We fixed length units by taking particles to have unit volume. Every 1.4×10^5 timesteps, k was linearly decreased until it was eventually 0; each time k was changed, move sizes were tuned, 10^5 timesteps were run for equilibration, and the lattice energy was computed in the remaining 4.0×10^4 timesteps.
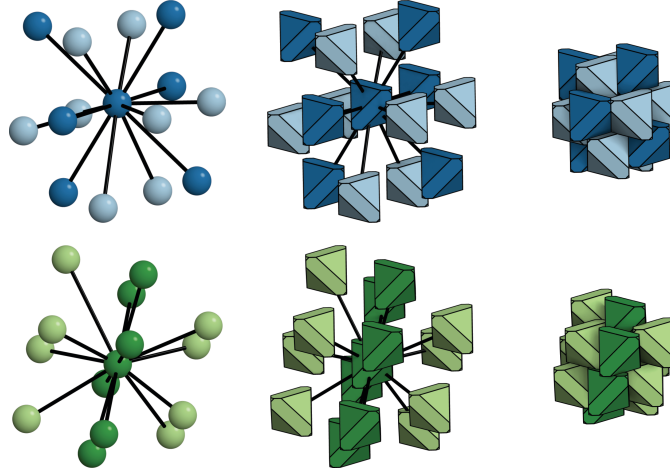
Figure 2.3: Example dense packing structures (where packing $\lambda_{A=74}$ is blue and packing $\lambda_{B=69}$ is green) of anisotropic shapes, including "exploded" views that show the location and orientation of neighboring particles, and densely packed units.
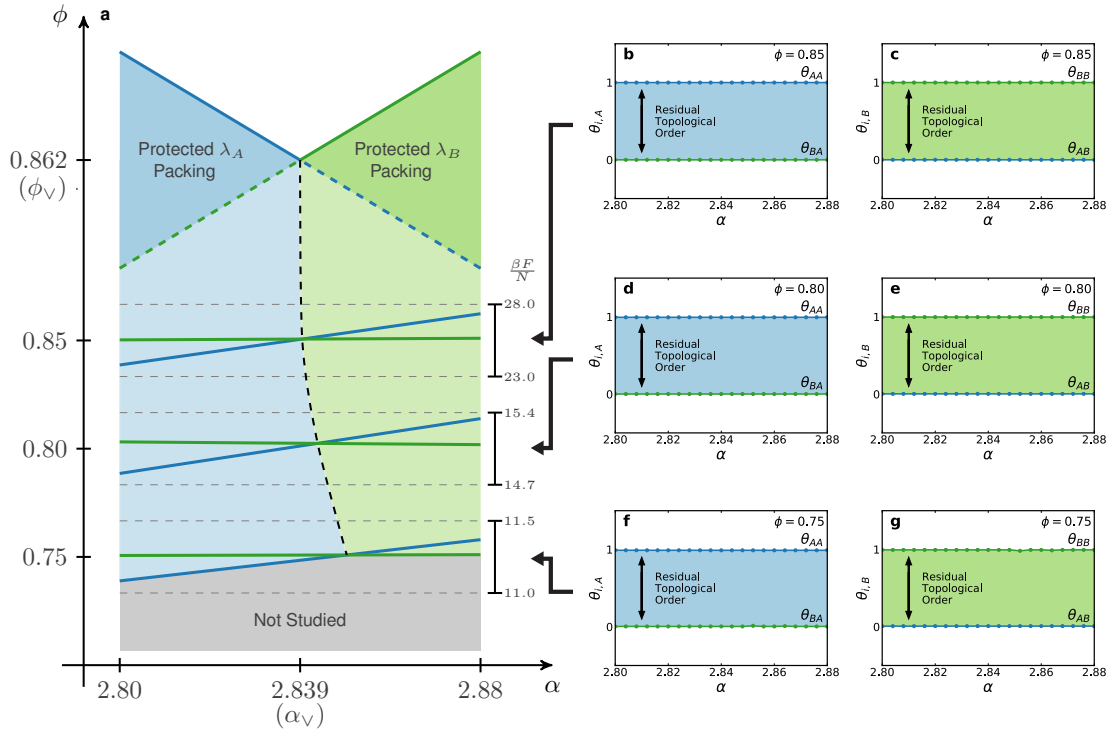
Figure 2.4: Panel (a) shows the curves of maximal packing density at $\phi_\vee$, outlining the two protected packing regions, where packing $\lambda_{A=52}$ is blue and packing $\lambda_{B=58}$ is green. Lower curves indicate computed free energies at three packing densities (0.85, 0.80, 0.75). Darker shaded colors indicate protected regions, while lighter shaded colors indicate free energy preferred regions of the (α, ϕ) phase diagram. The gray region is a region where the preferred phase is unknown. Panels (b, d, f) indicate topological order evaluated using the intersection equations for $\lambda_{A=52}$ and panels (c, e, g) indicate the same using the intersection equations for $\lambda_{B=58}$. The dotted black line roughly demarcates boundaries between thermodynamically preferred packings as a function of packing density, and is meant to guide the eye.
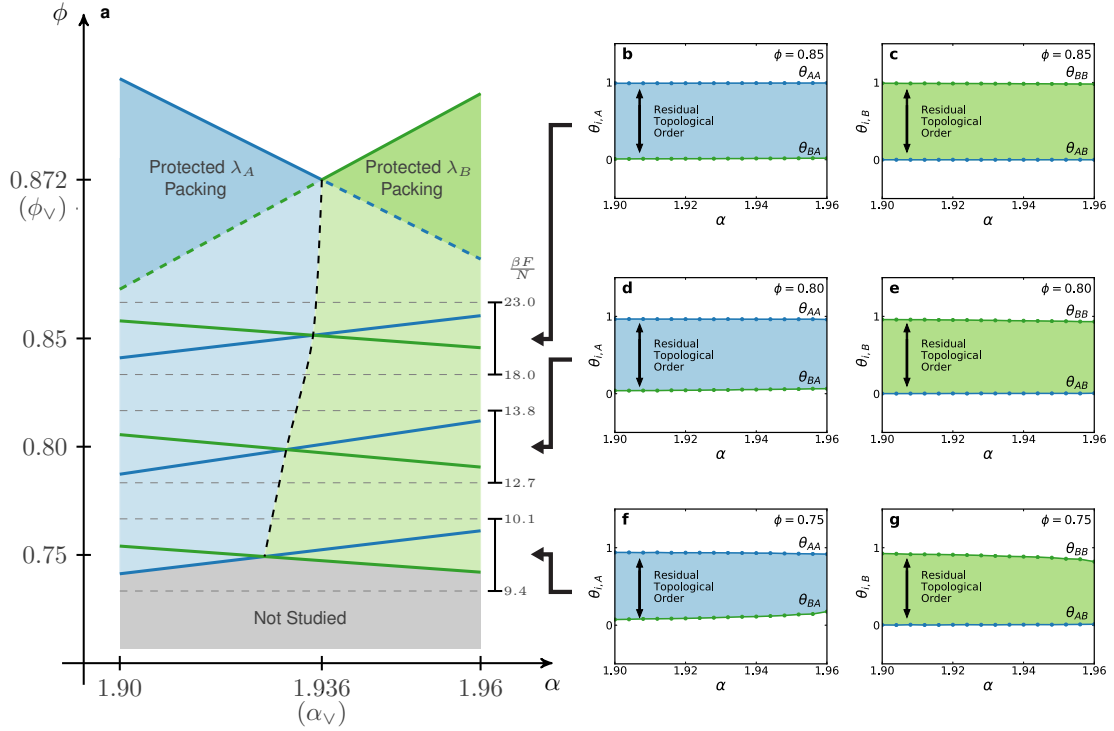
Figure 2.5: Panel (a) shows the curves of maximal packing density at $\phi_\vee$, outlining the two protected packing regions, where packing $\lambda_{A=74}$ is blue and packing $\lambda_{B=69}$ is green. Lower curves indicate computed free energies at three packing densities (0.85, 0.80, 0.75). Darker shaded colors indicate protected regions, while lighter shaded colors indicate free energy preferred regions of the (α, ϕ) phase diagram. The gray region is a region where the preferred phase is unknown. Panels (b, d, f) indicate topological order evaluated using the intersection equations for $\lambda_{A=74}$ and panels (c, e, g) indicate the same using the intersection equations for $\lambda_{B=69}$. The dotted black line roughly demarcates boundaries between thermodynamically preferred packings as a function of packing density, and is meant to guide the eye.

2.5 Results

2.5.1 Boundary I

Figure 2.4(a) shows the curves of maximal packing density ϕ_d for each packing type, indicating the protected regions in darker shading under them. Below that are curves of free energy as a function of both packing and shape at various packing densities ϕ well below the maximum packing density ϕ_d. Several possibilities exist below ϕ_d, and we test for these possibilities:

- Packing states could become thermodynamically unstable at any finite packing density below ϕ_d, meaning that packing is a kind of singular limit with no associated thermodynamic phase.

- Distinct phases persist below ϕ_d, but these phases do not preserve topological order, which would occur if other contacts proliferate in the lower packing density phases.

- Distinct phases with topological order persist.

To rule out non-existent phases, we compute the free energy of decompressed packing states. Plots of free energy (Figure 2.4(a)) show that even at packing densities well below ϕ_d, two phases persist up to some crossing. The location of this crossing at packing densities below $\phi_\vee$ need not be at $\alpha_\vee$, and we find that it does deviate from $\alpha_\vee$ at lower packing density. The thermodynamically preferred regions are colored in lighter shades of the protected regions. To verify that the two phases at finite pressure have persistent and distinct topology of particle packing, we compute the relevant order parameters from Eq. 2.16 for each structure. This calculation is performed by extracting the unit cells of the thermalized packings of λ_A and λ_B at a packing density ϕ.

To rule out the possibility that the phases lose topological order, we computed the θ_{ij} order parameters in the phases corresponding to thermodynamic states in our free energy calculations. We find that at packing densities well below $\phi_\vee$, phases identified by the free energy calculation correspond to phases that differ in the topology of particle contacts measured through the order parameters θ_{ij}. In Figure 2.4(b, d, f) we evaluate the order parameter θ_{iA} on structures λ_i where $i \in \{A = 52, B = 58\}$ and find that over a range of packing densities, θ_{iA} evaluates to near unity on λ_A and vanishes on λ_B. Conversely, in Figure 2.4(c, e, g) we evaluate the order parameter θ_{iB} on λ_A and λ_B and find that over a range of packing densities, θ_{iB} evaluates to near unity on λ_B and vanishes on λ_A.

These results indicate that the phases can be identified by the topology of the related putative densest packings, and possess residual topological order, or order that matches the order of a topological state at a packing density where topological protection has not been proven to exist. The residual topological order we observe in Figure 2.4 suggests that crystal structures present in densely packed colloidal suspensions maintain a topologically consistent set of contacts between particles at densities where other competing contact topologies could exist, but are unlikely to do so due to the existence of a more thermodynamically favorable topological state.

2.5.2 Boundary II

Figure 2.5(a) contains similar results for the 2nd boundary studied in this work, as it shows that a free energy crossing exists at packing densities well below the maximal packing density. In Figure 2.5(b, d, f) we evaluate the order parameter θ_{iA} on structures λ_i where $i \in \{A = 74, B = 69\}$ and find that over a range of packing densities, θ_{iA} evaluates to near unity on λ_A and vanishes on λ_B. Conversely, in Figure 2.5(c, e, g) we evaluate the order parameter θ_{iB} on λ_A and λ_B and find that over

a range of packing densities, θ_{iB} evaluates to near unity on λ_B and vanishes on λ_A. Again, these results indicate that the phases can be identified by the topology of the related putative densest packings, and possess residual topological order. These results also suggest that this type of residual topological order can be found at valleys throughout this packing landscape, and that this type of behavior is generalizable to many different dense colloidal packings.

In this system though, it should be noted that there is noticeable deviation in the order parameters θ_{BA} and θ_{BB} as α_c approaches the value of 1.96. θ_{BA} (in Figure 2.5(f)) trends slightly upward and θ_{BB} (in Figure 2.5(g)) slightly downward, and it is a subtlety of the packing ($\lambda_{B=69}$) that, when captured by our order parameter, produces such deviation. We do not believe that this slight deviation indicates a change in topology.

2.6   Discussion

The topologically distinct phases of dense suspensions of anisotropic colloids that we find here are dissimilar to topological phases in quantum matter in almost all respects, except in their stability against perturbations. For instance, whereas the topological entropy of ground-state degeneracy that arises from entanglement is important in quantum systems [54], in our systems, instead, shape entropy [10] quantifies ground state degeneracy. Moreover, whereas the geometric topology that underlies topological order in quantum systems allows a considerable mathematical apparatus to be brought to bear in understanding those states, the point-set topology that underlies the classical, topological order we identify here is more limited. Nevertheless, despite the rudimentary form of the topological order reported here, colloidal systems remain robust against perturbation, since they persist even at lower

packing densities where topological protection is no longer required. This robust persistence would be a key desirable feature for applications in regimes away from the infinite pressure limit. Moreover, because the form of topological order is more rudimentary, previous work [2] demonstrating that topological features (such as particle contact types between faces, edges and vertices) generically distinguish phases of densely packed colloids suggests that this form of topological order is widespread in colloidal systems [55, 56, 57, 58, 59].

To leverage this topological order in experiment we note that though our order parameters are based on contact types that nominally arise at infinite pressure, we showed that topological order persists at finite pressure, meaning that alterations in contact do not proliferate at lower packing densities. This finding is potentially useful in constructing plasmonic materials that have robust response in the presence of thermal fluctuations, changes in particle shape [13] or the behavior of stabilizing ligands [60, 61]. It is known that the plasmonic response of systems of anisotropic nanoparticles depends strongly on the type of contacts between nanoparticles [8]. We find that the topology of contacts between anisotropic nanoparticles is stable over a broad range of packing densities. When situated in the context of the zoo of distinct sets of contact types that has been shown to exist [2] in families of anisotropic nanoparticles and the variety of synthesis techniques that can readily produce such particles in the laboratory [5, 6, 7, 62], our work points to potential avenues for creating nanomaterials with a diversity of robust forms of plasmonic response.

CHAPTER III

Design Rules for the Self-Assembly of Regular Polygons

This chapter is adapted from a publication in preparation, authored by W. Zygmunt, T. Vo, J. A. Anderson and S. C. Glotzer.

3.1 Introduction

The desire for porous 2D nanostructures is driven by a plethora of applications, including their use as molecular sieves [26, 27], gas storage materials [25] and photonic applications [24]. These materials can possess novel physical properties such as negative Poisson's ratio [63, 64] and tunable pore size, useful for applications such as gas filtration [65]. Such studies often involve the usage of patchy particles [12], which can often be defined by a decoration of a nanocrystalline core with attractive and highly-directional tethers. Much work has gone recently into designing patchy protostructures which have the ability to self-assemble into complex open structures including work on building blocks with tunable pore size [66, 67], colloidal building blocks with tunable specificity [67], patchy non-convex hexagonal platelets [68] and atom-mimicking patchy spheres [69]. Studies of selective patches on patchy rhombi [70] have also been shown to allow tuning from close-packed tilings structures to open lattices using specific sets of design interactions and in a further work showed how protostructures procured here could be used to perform self-assembly in a hierarchical

fashion [71].

Regular polygons are materials that can be synthesized with relative ease [72, 73, 74], which makes them ideal candidates for such design considerations. In fact, regular polygons were shown to self-assemble into the Archimedean tilings via a set of design rules [22] which used edge-specific, A-B attraction between pairs of such polygons. Such design rules allowed for the targeting of each tiling based on the shapes and interactions involved in the self-assembly process. Design rules such as these are powerful tools, as they allow for classification of the space of particle features that contribute to the the self-assembly, of which there can be many [1]. Design rules have been used in many self-assembly studies, from establishing rules for how to create cage compounds to form faceted polyhedra [75] to rules established for nanoparticle superlattice engineering [76]. In the latter, such rules account for the interplay of the size ratio of nanoparticle size ratio and DNA linker ratio to account for all possible self-assembly outcomes.

In [22], regular polygons were patterned to *specifically* target the Archimedean tilings, and the question remains: what other structures can be achieved through selective edge-edge binding, and are there more structures that can be predicted via the way one chooses to pattern the edges of regular polygons? In this work, we consider a set of design rules that focuses strictly on the self-assembly of pairs of regular polygons via complementary A-B binding. Each polygon has some subset of it's edges that are allowed to participate in attraction, which allows for selective edge-edge binding between pairs of polygons. We consider all members of a polygon's edge-pattern family (see Methods section), which is the set of different ways one can permute edges that can act as available sites for binding (we define these families mathematically in the Methods). We show that when the members of a shape's

edge-pattern family is set up to self-assemble with members of another shapes's edge-pattern family, a clear set of design principles emerge which can be used to target specific morphological classes.

Our design rules consider multiple factors that contribute to the assembly, including the number of edges and patch structure of both particles (which includes the symmetry and number of patches along the polygon edge) as well as the stoichiometry ϕ_A. The design rules developed here allow for the targeting of a variety of different morphology including terminal structures, fibers, rings and lattice structures (packing and open structures). Additionally, we demonstrate and describe how many of these morphology may be used in various hierarchical design schemes [77, 78] in order to target open structures for various applications. Our design rules also describe how the stoichiometry should be set in order to obtain certain morphology, and how the number of patches is a good predictor of the void fraction of lattice structures.

3.2 Methods

3.2.1 Binary Systems of Edge-Pattern Polygon Families

In order to understand how many patchy polygons could exist for some regular polygon with n sides, we first must establish a method for counting every way one could permute such patches. This problem can be represented as a k-ary necklace of length n, an equivalence class of n-length of which each element is assigned some state k. Consider a regular polygon with n sides and that each side can have no attractive patch or an attractive patch ($k = 2$ options). Then, the number of members in an n-sided polygon's edge-pattern family N is given by:

$$
(3.1) \qquad N(n,k) = \frac{1}{n} \sum_{i=1}^{v(n)} \phi(d_i) k^{n/d_i} - 1
$$

25

where d_i are divisors of n, $v(n)$ are the number of divisors of n and $\phi(x)$ is Euler's totient function. The subtraction of 1 is to account for the state where there are no patches on the particle.

In this work, we aim to explore the self-assembly behavior of all members of a shape's edge-pattern family against all members of a second shape's edge-pattern family (for example, this could be triangles and squares ($N(3,2)$ against $N(4,2)$) or triangles with themselves ($N(3,2)$ against $N(3,2)$). Consider two general shapes, the first with n_A sides and the second with n_B sides; the total number of patchy polygon pairs are:

$$(3.2) \qquad P(n_a, n_b) = \begin{cases} N(n_a, 2) \times N(n_b, 2) & n_a \neq n_b \\ \frac{1}{2}\left[N(n,2)^2 + N(n,2)\right] & n = n_a = n_b \end{cases}.$$

As an example, we take the case of regular triangle and regular squares, which we study in this work as one of the basis for our rules. Using Eq. 3.1, one can calculate the number of members of the triangle edge-pattern family as $N(3,2) = 3$ and the square edge-pattern family as $N(4,2) = 5$, which can be seen in Figure 3.2(a). Therefore, there are $P(3,4) = 3 \times 5 = 15$ total combinations of members of the triangle and square edge-pattern families that should be explored with self-assembly simulations.

The motivation for these design rules can be shown from the math; for example, if one wanted to determine the number of patchy polygon pairs that would have to be simulated in order to understand the self-assembly behavior of all patchy hexagons with all patchy octagons, you would need 455 simulations, far more than is computationally feasible.

3.2.2 Potential for Ligand-Ligand Interaction

In order to connect our simulations to experimentally relevant systems, we first compute an effective potential of interaction between patchy particles that explicitly accounts for the distribution of ligands mediating directed self-assembly. Here, we assume that ligands are uniformly distributed within a given patchy region. However, for anisotropic particles, the effect of local curvature on ligand confinement must be explicitly considered. Previous works involving both theory and simulations [17, 79, 80, 81] have rigorously shown that, for uniform grafting, ligands attached to locations of lower curvature on the particle's surface experience increased crowding from nearby grafts. This local confinement forces ligands to extend further out from the particle surface in order to minimize their steric repulsion with neighboring grafts. As a result, the probability $P(h, \Omega)$ of finding an interacting ligand end necessarily depends on both the distance h away from the particle surface as well as the local curvature Ω. Employing a developed scaling relation for predicting ligand extensions [82], we can write the probability of finding a ligand end at position R away from the surface as $P \sim \exp(-\beta F)$ where $\beta F \sim \frac{R^2}{Nb^2} + \frac{\nu N^2}{(\Omega R)^3}$ and $R \sim N^{1/3}\Omega^{-1}$ for short ligands. Here, b is the ligand size, ν defines the excluded volume of the ligand (taken as νb^3) and N is the ligand length. The effective potential between two neighboring patches is then

$$(3.3) \qquad V(r) \sim \int_0^r P_i(r', \Omega_i)P_j(r' - h, \Omega_j)dr'd\Omega.$$

Figure 3.1 shows the functional form of the computed potential between neighboring patchy particles with interacting patches facing each other. We note that the functional form of the effective potential of interaction between patchy particles is
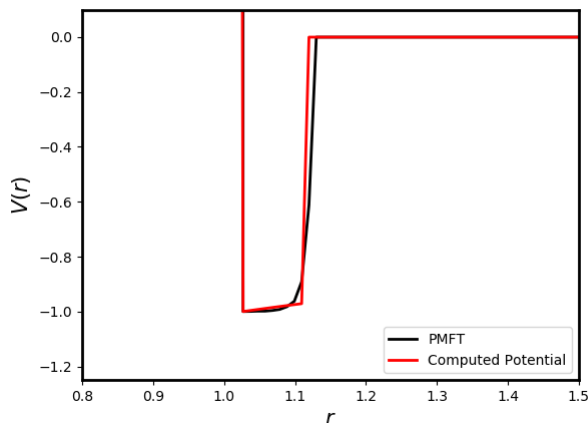
Figure 3.1: Comparison of the edge-edge interaction computed from the PMFT to the computed potential employed in this work.

similar to a square-well potential with an approximate $1/r$ decay in the well depth (Figure 3.1)

$$(3.4) \qquad V(r) = \begin{cases} \infty & r < \sigma \\ -\epsilon/r & \sigma < r < \sigma + h_m \\ 0 & r > \sigma + h_m \end{cases} .$$

Thus, for computational efficiency, we employ Eq. 3.4 within our simulations to approximate this interaction.

3.2.3 Simulation Methods

We performed simulations using HOOMD-blue's [83] HPMC package [48] for Monte Carlo simulations. We implement the pair potential described above between A and B particles in our simulation and let the system equilibrate by performing translational and rotational moves on particles in the system. We also perform cluster moves via the geometric cluster algorithm [84] and use line reflections [85], which allow us to move large clusters of particles by performing pi rotation around an axis

for our anisotropic particles.

The A-B attraction simulations are conducted with two particle types where one polygon (with n_A sides, p_A patch distribution and m_A number of patches) has the described attractive forces to a second polygon (n_B, p_B, m_B). For each statepoint, we initialize 1024 particles into a simulation box with a stoichiometry of ϕ_A and perform NPT simulations ($\beta P = 1.0$ unless otherwise noted) where we allow the box volume and shape to fluctuate during the course of the simulation. Initially, we run these systems without A-B attraction for 1 M timesteps to randomize them from their initial configuration and then tune the box moves so they have an acceptance ratio of 0.3. We estimated ϵ_m (the inverse temperature around where we anneal our simulations) for each statepoint by implementing a slow ramp from $\epsilon = 0.0$ to $\epsilon = 20.0$ over 10 M timesteps and employ a clustering algorithm from Freud [86] to generate a logistical function, used to approximate ϵ_m. Next, we slowly ramped up to ϵ_m over 5.4 M timesteps and then anneal for an additional 30 M timesteps to assure that our final structure is indeed the equilibrium structure. Lastly, we ramp ϵ up to $\epsilon = 20.0$ over 5 M timesteps to freeze remaining single particles in place.

3.3   Design Rules

We establish a set of design rules which we determined from binary Monte Carlo simulations of all members of the simplest edge-pattern families (triangles against triangles, squares against squares, triangles against squares) (Figure 3.2(a) shows the members of these families). We use a modulated, square-well potential to represent the functionalization of selected edges of two polygons with short ligands (described in the Methods) and perform Monte Carlo simulations using HOOMD-blue [83]. Briefly, simulations were implemented over a variety of stoichiometry

($\phi_A = [0.1, 0.2, ...0.9]$) and pressure was held constant at $\beta P = 1.0$ (unless otherwise stated) (see Methods for more details). With each rule, we discuss these morphology in the context of a hierarchical design framework (if appropriate) and how they can be utilized for higher-order structures.

3.3.1 Terminal Structures

Terminal structures can be obtained if at least one particle in the pair of polygons has a single patch, provided particle shape allows for binding at adjacent edges.

We define *terminal structures* as structures where all available edges for binding on both particles become satisfied. These structures are not subject to the typical kinetic traps found in systems of patchy particles, due to the lack of choice in binding sites. The rule is designed so that if one particle (A) has $m_A \geqslant 1$ patches and the other (B) only has one, then B particles will bind to A particles and close off any available growth sites. For example, consider Figure 3.2(b), where we demonstrated that a one-patch triangle with cover a four-patch square in order to form four-arm isotoxal stars. Stoichiometry controls the yield and for this shape, the maximum yield occurs when there is a 4:1 ratio of triangles to squares. This rule applies only when particles can bind along adjacent edges of the particle with more patches; if they can, then the ideal stoichiometry can always be determined by computing the following equation (where m_i is the number of patches):

$$(3.5) \qquad\qquad \phi_A = \frac{m_B}{m_A + m_B}$$

In binary systems of triangles, we demonstrate the formation of a variety of *composite shapes* (Figure 3.3) including rhombuses, trapezoids, and larger regular triangles in perfect yield at the appropriate stoichiometry. In binary systems of squares,
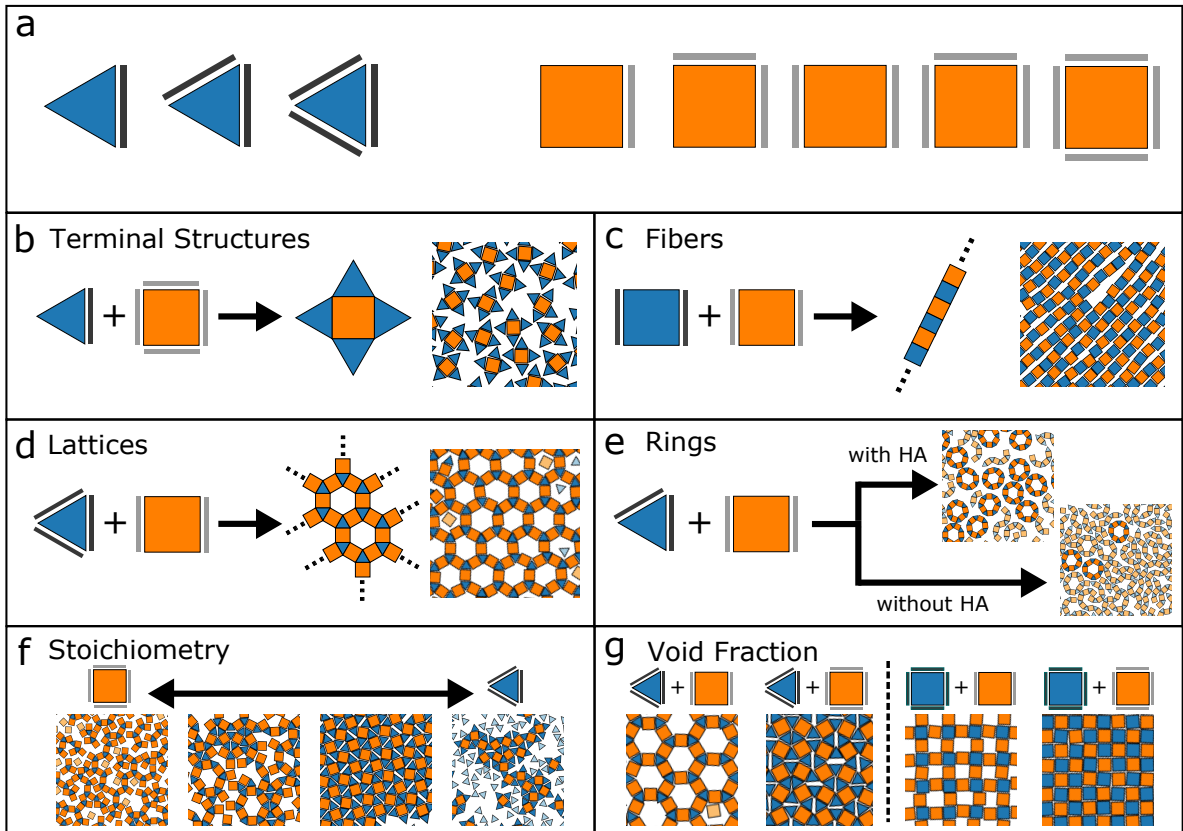
Figure 3.2: Edge-pattern families for both regular triangles and regular squares (a). Design rules demonstrate the formation of different structures from members of these families, including self-terminating structures (b), fibers (c), lattice structures (d), and ring structures (e). Ring structures can be assembled in higher yield with the addition of hierarchical assembly (HA) to overcome kinetic effects. We show that stoichiometry can control the final structure and has a sizable affect on yield (f). Lastly, we demonstrate that the void fraction is dependent on the number of patches on each particle and can be used to control void shape (g).
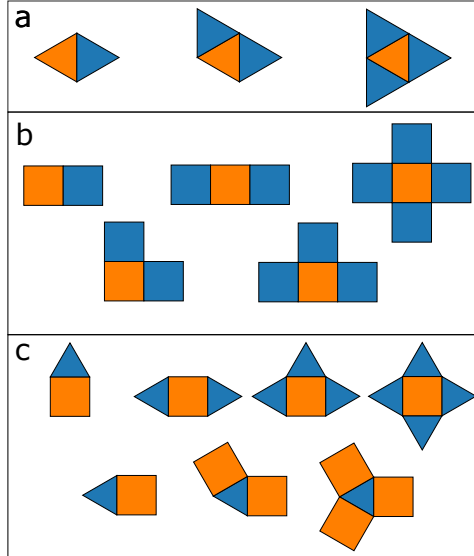
Figure 3.3: Composite shapes for triangle-triangle (a), square-square (b) and triangle-square (c) terminal assembly rule.

we are able to produce a variety of different polyominoes [87] including the concave plus-sign shaped pentomino; given that a square can, at most, harbor four attractive edges, pentominoes are the largest terminal structure that systems of binary squares can assemble. Triangle-square systems give by far the most diverse morphology, allowing us to access concave shapes such as the four-arm isotoxal star (shown in Figure 3.2(b)), the elongated hexagon (whose self-assembly is well-understood [21]) and concave nonagons. We demonstrate formation of the plus-sign pentomino in Figure 3.4(a, left snapshot) and the four-arm star in Figure 3.4(b, left snapshot).

Given that the goal of this work was to target open structures, it became clear that the concave shapes might be the most interesting candidates for a hierarchical design approach, where the first stage consists of assembling the composite shape from regular polygons and the second stage consists of compression into an ordered structure. To do this, we first took the plus-sign pentomino and the isotoxal star and extracted the vertices of these shapes to make a composite concave shape for Monte Carlo simulation under compression. We initialized these shapes in the fluid

and compressed them by stepping up the pressure by $\beta P = 0.1$ every 5×10^4 steps until we reached a final pressure of $\beta P = 10$ and formed a square tiling for the plus-sign pentominoes (Figure 3.4(a, right snapshot)) and an open structure with periodic rhombic voids for the four-arm star (Figure 3.4(b, middle snapshot)).

The composite shapes we've studied under compression also have the distinction that they are motifs which appear in two different Archimedean tilings (the square tiling and the snub square tiling). We explored the possibility of co-assembly of our composite shapes with the complementary shapes required to form such tilings. The plus-sign pentomino packs neatly into it's densest packing and the squares forming these shapes form a square tiling, so additional squares will not affect the final assembly. The four-arm star motif is present in the snub square tiling (which is a densest packing of triangles and squares) but is lacking the squares that sit in the gaps between these motifs. We added squares to our starting fluid of the four-arm stars (in a 1:1 ratio) and co-assembled a snub square tiling with a 11213 coloring; this coloring is different than the one achieved by isotropically patchy triangles and squares (11212), because the extra squares added for the co-assembly do not necessarily need to be the same ones used to form the four-arm stars.

In order to test the extendability of this rule to regular polygons with even more sides, we show the self-assembly of hexagram shaped particles from one-patch triangles and isotropically-patterned hexagons (Figure 3.4(c, left snapshot)) and that subsequent compression leads to another open structure densest packing, this time an Archimedean tiling (the snub hexagonal tiling), possessing triangular voids (Figure 3.4(c, middle snapshot)). In the presence of extra hexagons, we demonstrate co-assembly into the space-filling trihexagonal tiling (Figure 3.4(c, right snapshot)). Self-assembly of patchy hexagrams have been studied in prior work [88] and have
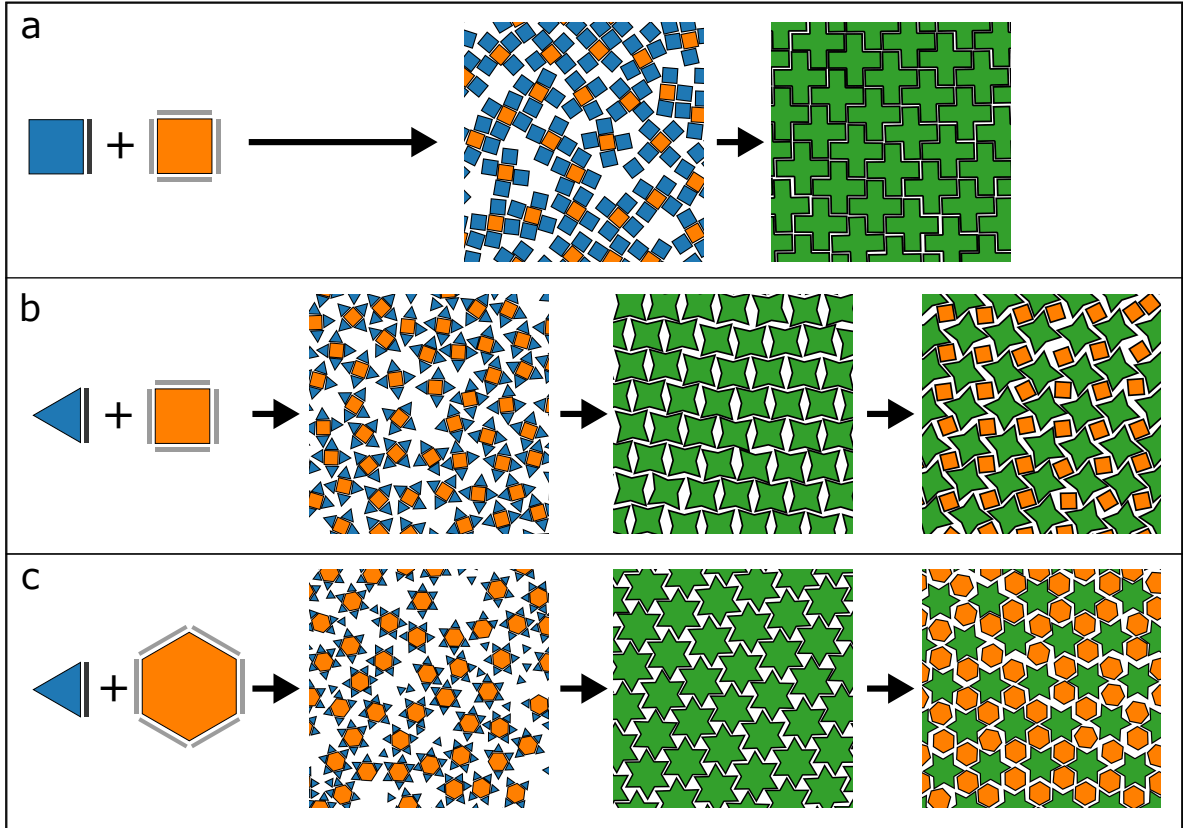
Figure 3.4: Hierarchical design approaches for lattices obtained from the terminal structure rule. Squares assemble into plus-sign pentominoes which pack into a square lattice (a). Four-arm isotoxal stars pack into an open structure with rhombic voids and co-assemble into a snub square tiling with free squares (b). Triangles and hexagons assemble into hexagrams which pack into a snub hexagonal lattice and co-assemble into a trihexagonal tiling with free hexagons (c).

been shown to form ordered lattices with rhombic voids when patches are applied on the tips of the triangular arms, and this rule could assist in forming the starting material with the core (hexagon) and the spikes (triangles) using potentially different materials.

3.3.2 Fibers

Fibers will be obtained if both particles in the pair of polygons have two patches on parallel edges.

Fiber formation encompasses a very limited scope of our self-assembly space, due

to the small number of cases where they can form. Fibers in our context consist of long, straight chains of polygons of alternating type. In this construction, patches must exist perfectly on the opposite edges of both particles, because deviation from perfectly parallel edge locations will induce an angular dependency in the growth front and disrupt the straight nature of fiber growth. When considering binary systems of triangles, fibers will not form because triangles contain no parallel edges, and therefore, growth cannot occur along one consistent direction; this similarly prevents the formation of fibers in binary triangle-square systems. Fibers made of alternating squares are possible however, since they meet this criteria. Stoichiometry controls the yield of fibers, with no kinetic traps present because rotation of either particle will not change the orientation of locking. Maximal yield always occurring at $\phi_A = 0.50$ where particles can maximize their alternating motif. We demonstrate that for binary systems of squares that we form long fibers of alternating square types as demonstrated in Figure 3.2(c).

We further demonstrate that fibers also form when we pattern hexagons with two patches on their parallel edges (Figure 3.5(bottom, d)) and in general, we expect that any pair of polygons with even numbers of edges will form fibers, as long as patches appear on parallel edges, meaning that would occur in pairs of squares, hexagons, octagons, etc. Additionally, we see that these fibers line up against each other in an attempt to minimize the space between them (fibers of squares and fibers of hexagons can form Archimedean tiling structures when lining up is perfect).

3.3.3 Lattices

Lattice structures can form if both particles in the pair of polygons have patch distributions that can bind symmetrically.

Formation of lattice structures are the fastest route to finding open structures, since they do not require additional hierarchical stages beyond the initial formation of the lattice. It is an open question, however, of how to best pattern shapes with patches to effectively assemble such lattices such that kinetic traps are not an issue in the formation. Consider the shapes shown in Figure 3.2(d) and the lattice structure they form, the rhombitrihexagonal tiling; note that if connecting the triangle to the square, one could rotate each shape to another patch in the patch distribution and not change the directionality of the other patches. This prevents kinetic traps in the formation, since the symmetrical binding abilities of the patch set eliminates random branching from patches pointing in random directions incommensurate with the lattice structure.

Considering the triangle and square systems, we find that triangles have one particle that fits this description (patches on all three edges) and squares have two (the square with patches on parallel edges and the square with patches on all four edges). We demonstrate that combinations of these patchy polygons lead to lattice formation, with an exception in the case of the two-patch square with another two-patch square leading to fiber formation (Figure 3.5(top, e)). As a consequence of the way the lattice rule is designed, we find that the rule for fibers is actually a subset of this rule, since the particles described in the fiber rule fall naturally under the description of particles with symmetrically-binding patch sets. Lattices found include the triangular tiling, the open rhombitrihexagonal tiiling, the snub square tiling, the square tiling (1213 uniform coloring) and the square tiling (1212 uniform coloring) (Figure 3.5(top, (a, b, c, f, i))). The remaining lattices (d, g, h) are simply recoloring of the same lattices shown in (b, c, f).

Stoichiometry of these lattices are indicated as ϕ_A where A represents the particles

on the y-axis (the blue particles). The stoichiometry for lattices must be considered carefully as deviation from the optimal value can have one of the following effects on formation: it can simply depress the yield of the desired lattice or it can completely suppress the lattice formation. We find that if a lattice can form by saturating every patchy edge in the system, it will always do so, and stoichiometry only controls the yield of the lattice. Some systems, such as the snub square tiling shown in Figure 3.5(top, c), require the presence of open patchy edges (one triangular edge must be kept open) and there, stoichiometry must be carefully considered (see Section 3.3.5). Pressures were constant for all of these lattices at $\beta P = 1.0$, but we had to compress the snub square tiling after crystallization had concluded in order to achieve the tiling structure which is free of voids resulting from the unbonded triangle-triangle edge.

In order to verify that this rule holds for a larger range of polygons, we perform similar simulations on the patchy triangle that fits the description dictated by this rule along with all patchy hexagons that do so (the hexagon with patches on parallel edges, the three-patch hexagon with three-fold symmetry and the hexagon with patches on all six edges). Like in the triangle-square systems, the two-patch hexagon simulated with another two patch hexagon form hexagonal fibers (Figure 3.5(bottom, d)), confirming the intersection of these two rules.

Triangle-hexagon lattice-forming particles form a few variations of the trihexagonal tiling with hexagram voids, a cantic hexagonal tiling (which has triangular voids) and the space-filling trihexagonal tilings (Figure 3.5(bottom, (a, b, c))). Hexagon-hexagon lattice formers make different constructions of the hexagonal tiling including an open structure with a concave octadecagon void, an open structure with a hexagonal void and several variations of the space-filling hexagonal tiling (Figure

3.5(bottom, (e, h, f, i, l))). The remaining lattices (g, j, k) are simply recoloring of the same lattices shown in (e, f, i). All lattices were formed at $\beta P = 1.0$ except for Figure 3.5(bottom, (e, g)) which due to it's large void fraction would only form at $\beta P = 0.25$.

While this rule serves as a good predictor of lattice formation, it's weakness is its inability to distinguish between open structures and space-filling tilings and tilings. The only way to guarantee an open structure is to encapsulate the void via a ring of nanoparticles, which can be formed uniformly and then self-assembled into the higher-order open structure.

3.3.4 Rings

Rings can be formed if both particles in the pair of polygons have two patches, and at least one of them does not have them on parallel edges.

Rings are useful candidates for hierarchical design if the shape of the ring can be assembled into a higher-order structure, since that order effectively orders the hollow centers into a periodic and open structure. The ring design rule requires two particles, each with a set of two patches (where at least one does not have those patches on parallel edges) that connect in an alternating fashion; this rule is specific as to avoid the conditions for the fiber rule (both particles with two patches on parallel edges). It is possible to select two-patch candidates that will not form open rings, so care must be taken so the selected particles close an open ring. We study two cases of rings: square rings with square holes (formed by two kinds of patchy squares) and dodecagonal rings with hexagonal holes (formed by a patchy triangle and a patchy square). Stoichiometry must be fixed at $\phi_A = 0.50$ in order to guarantee ring closure (since particles have A-B attraction and particles connect in an alternating fashion).
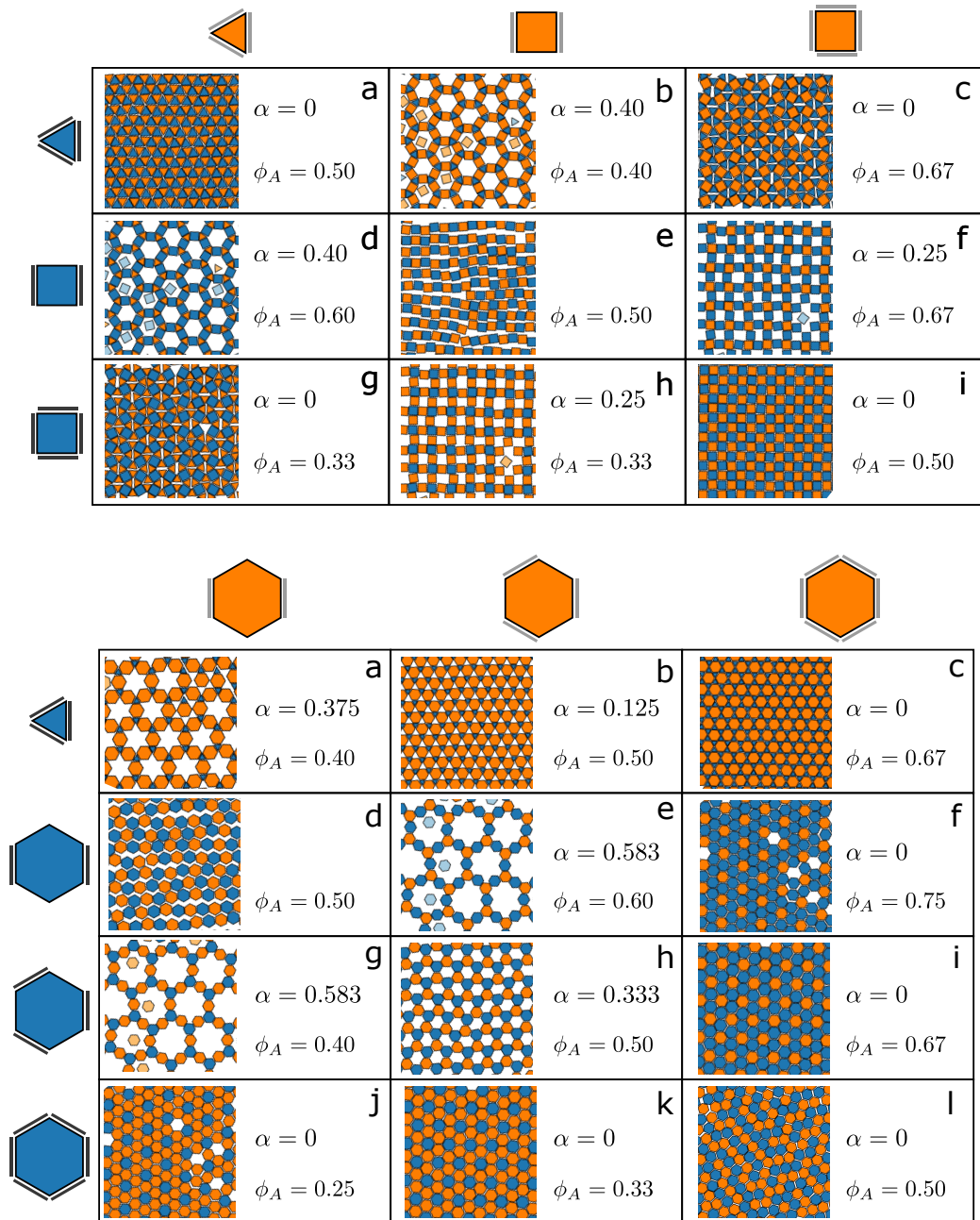
Figure 3.5: We demonstrate the application of the lattice rule to the edge-pattern families of triangles against triangles, squares against squares and triangles against squares (top) as well as triangles against hexagons and hexagons against hexagons (bottom). The shapes along the axis indicate the symmetrically patchy polygons used in the pairing, where the edges of blue shapes (A) are attracted to edges on orange shapes (B). We denote the packing fraction required to form the lattice (ϕ_A) as well as the ideal void fraction (α) calculated from the unit cell.

39

Initial simulations of both systems demonstrate some ring formation, but high-yield self-assembly is precluded by the presence of kinetic traps.

At least one of the particles, by design, must have patches on non-parallel edges and because of this, the remaining open patches could point in different directions on attachment to the next particle. When this particle attaches, it may connect via either of its two patchy sites and since they are not on parallel edges, one connection is "correct" (leading to ring formation) and the other leads to a kinetically trapped structure. At every stage of particle addition to a ring, it is possible to form such kinetic traps, making it difficult to achieve high yield of rings without misconnection occurring and precluding ring formation. Simulations of $N = 1024$ particles (chosen so that our maximum yield is $1024/8 = 128$ rings) over five replicates (where we annealed for 40 M timesteps) gave a yield of 50.6 ± 6.5 % (Figure 3.6(a)) which is low, and observations of the system show the formation of structures incommensurate with ring formation.

We implement a series of hierarchical design choices which help to close off some of the routes leading to such kinetic traps, similar to the approach in [89] in which they use pre-assembled subunits to reduce the conformational freedom in micelle structures. In process 1 (Figure 3.6(c)) we utilize our terminal structure rule to create "corner" particles and then self-assemble those with two-patch squares; this process lowers the number of particle attachments required to form the final ring (from eight down to four) and gives an improved yield of 70.9 ± 4.0 %. However, we can boost yield even further by following process 2 (Figure 3.6(e)) which reduces the number of particle attachments and also makes two of the four particles involved in the self-assembly have the ability to bind symmetrically, lowering the number of kinetically trapped microstates even further, boosting our yield to 88.5 ± 0.7 %.

Consider the larger dodecagonal ring, consisting of 12 particles, where one would expect the yield to be lower for each process, simply due to the increased number of correct connections that must be made. Indeed, the yield for the original process for making such rings (Figure 3.6(b)) has a very low yield of 5.0 ± 2.2 % ($N = 1296$ particles, chosen so that our maximum yield is $1296/12 = 108$ rings), (we annealed here for 60 M steps due to the larger system size). We implemented processes similar to those for the squares (demonstrated in Figure 3.6(d and f) and find increased yields of 18.7 ± 3.1 % and 62.4 ± 1.7 % for process 1 and 2, respectively. Finally, we demonstrate the generalizability of this rule by applying it to hexagonal rings (with star-shaped voids) formed by patchy triangles and squares Figs. 3.6(g). In this case, we do not attempt assembly via the non-hierarchical route or the hierarchal route with lower yield, instead opting for the route with the highest yield informed by our understanding of which process leads to the fewest kinetic traps.

Figs. 3.6(e, f, g) demonstrate robust assembly of ring structures, all of which contain voids of varying shape. Self-assembling rings is difficult due to the presence of kinetic traps but since a void is guaranteed (if you choose the right starting materials) the extra effort makes the process desirable. These particular rings were chosen because they can support voids in their interior, and also for the fact that they all have densest packings of the rings themselves, allowing for compression into these structures for an ordered open structure. The square rings and the hexagonal rings will pack easily into their regular tilings and the dodecagonal rings will pack into a truncated hexagonal tiling [90], where there will be periodic void shapes (the hexagonal hole developed here and the triangular void that results from compression).
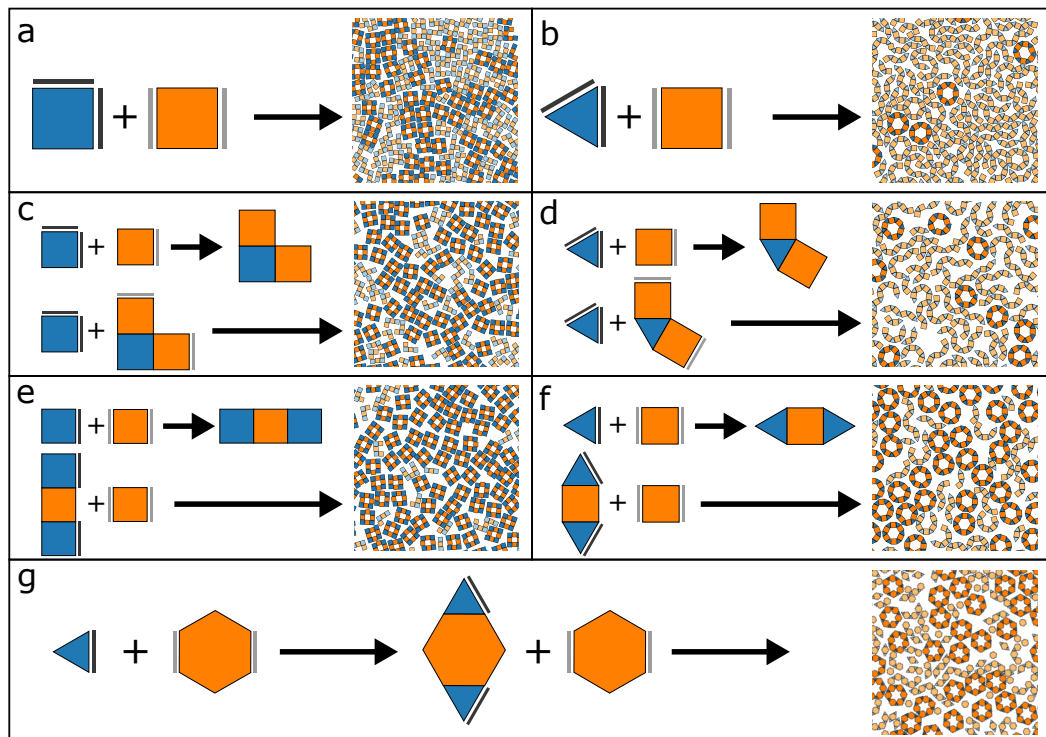
Figure 3.6: Ring structures can be formed by patterning two particles with two patches each. We attempt formation of square and dodecagonal rings without the use of a hierarchical assembly process (a, b) and find that kinetically trapped structures lower the yield of rings. We apply two different sets of hierarchical self-assembly processes for square rings (c, e) and dodecagonal rings (d, f) and find that these processes improve the reported yield. Lastly, we use the best form of hierarchical design rule to make hexagonal rings (g) in good yield.

3.3.5 Stoichiometry

Stoichiometry can control the yield of a desired structure and sometimes preclude its formation.

So far, each design rule has some stoichiometric element attached to it. In the rules for terminal structures, fibers and rings, the stoichiometry gives an effective control over the yield of the final structure, but doesn't change the actual structure that is formed. In the cases of lattices, there are two kinds of structures that can form: those that form with exposed patchy edges and those that do not. If the final structure doesn't have any such sites, then stoichiometry will again control only the yield, since the same bond types will be formed over and over, without the possibility of a secondary structure appearing. If a desired structure has such sites, then stoichiometry can control how and where particles attach, and studies have demonstrated that stoichiometry can control the final structure of certain crystalline structures, in systems of spherical nucleic acid nanoparticle conjugates [91] and DNA-grafted nanoparticles [92]. In the latter, the authors note that deviations away from ideal stoichiometry force the system to behave similarly to a series of competing parallel reactions, which we think could also represent the attempted formation of other less ideal structures in our systems.

We first consider the case of the snub square tiling first shown in Figure 3.5(top, c), which forms in systems of isotropically-patterned triangles and squares, with an optimal stoichiometry of $\phi_{square} = 0.67$. As can be seen from the simulation snapshot, one attractive edge of the triangle is always exposed in forming the tiling. Due to this requirement, stoichiometry should be balanced so that the number of squares never overtakes the number of triangles in a way that could lead to capping of all patchy

triangular edges. In order to quantify the presence of the desired snub square tiling, we use environment matching (implemented in Freud [86]) to compute the motif that each square makes along with the four squares that it's vertices make contact with. Briefly, environment matching checks each square in the system to see if the four vectors which connect it to its four square neighbors are similar, up to a threshold of $0.3 \times D$, where $D = \frac{1+\sqrt{3}}{2}$ is the magnitude of the vector connecting a center square to a neighbor (the motif created by these squares is shown in Figure 3.7(top, a)). We compute this matching over the final frame of our simulation, averaged over three replicates for a range of stoichiometry and show that the snub square environment presence peaks at the optimal stoichiometry (Figure 3.7(top, b)). We do not expect the matching to reach 100%, since squares on the edge will by construction not match the desired environment.

Next, we show the consequence of stoichiometric control in a case where a set of particles have the ability to form more than one lattice. Isotropically patchy squares and hexagons can form one of two lattices: a square tiling with hexagons acting as bridges between the squares (when $\phi_{square} = 0.33$) and a rhombitrihexagonal tiling (when $\phi_{square} = 0.75$) (Figure 3.7(bottom, a)). Once again, we simulated three replicates at stoichiometry from 0.1 to 0.9, including the ideal stoichiometry for the two lattices in question. At low amounts of squares, the system favors the structure where the square lattice arrangement occurs, and each hexagon gets two attached squares; the squares are completely covered by hexagons, due to their low amount in the system. At higher amounts of squares we observe the formation of the Archimedean tiling, formed by the excess squares isotropically covering the hexagons and allowing formation of the tiling. We compute presence of two environments with thresholds of $0.3 \times D_i$, where $D_1 = 1 + \sqrt{3}$ for the first environment (purple) and

$D_2 = \frac{1+\sqrt{3}}{2}$ for the second environment (green). Figure 3.7(bottom, b) shows peaks which match the ideal stoichiometry for both lattices shown.

3.3.6 Void Fraction

Void fraction is controlled by the number of patches on each particle; the more patches between particles, the smaller the void fraction.

We've demonstrated methods to target open structures through various means, such as hierarchal self-assembly of concave terminal structures and rings, and the formation of lattices via particles with patch sets that allow for symmetric binding. One useful aspect of the lattice rule is the ability to set up tables (such as those in Figure 3.5) which allow us to walk along the axis of these particles with symmetric binding, and observe potential trends in material characteristics as we add patches along this axis. One such observation is that when lattices are concerned (ignoring the fibers that this rule intersects), the void fraction of each lattice drops as a patch is added to either particle in the pair. We compute the void fractions of the ideal structure from the unit cell.

Consider first the lattices formed by a three-patch triangle and both the two- and four-patch squares (Figure 3.5(top, (b, c))). The rhombitrihexagonal tiling has a void fraction of 0.40 (with large hexagonal voids) and the snub square tilings has no voids, which suggests that adding patches to the square tends to make the lattice less open. We make the same observation with the lattices formed by a four-patch square and both the two- and four-patch squares (Figure 3.5(top, (f, i))) where the void fraction drops from 0.25 to zero via two kinds of square lattices. In order to make certain that these trends extend to other particle pairings we test them on the triangle-hexagon and hexagon-hexagon lattices and find similar behavior. In Figure
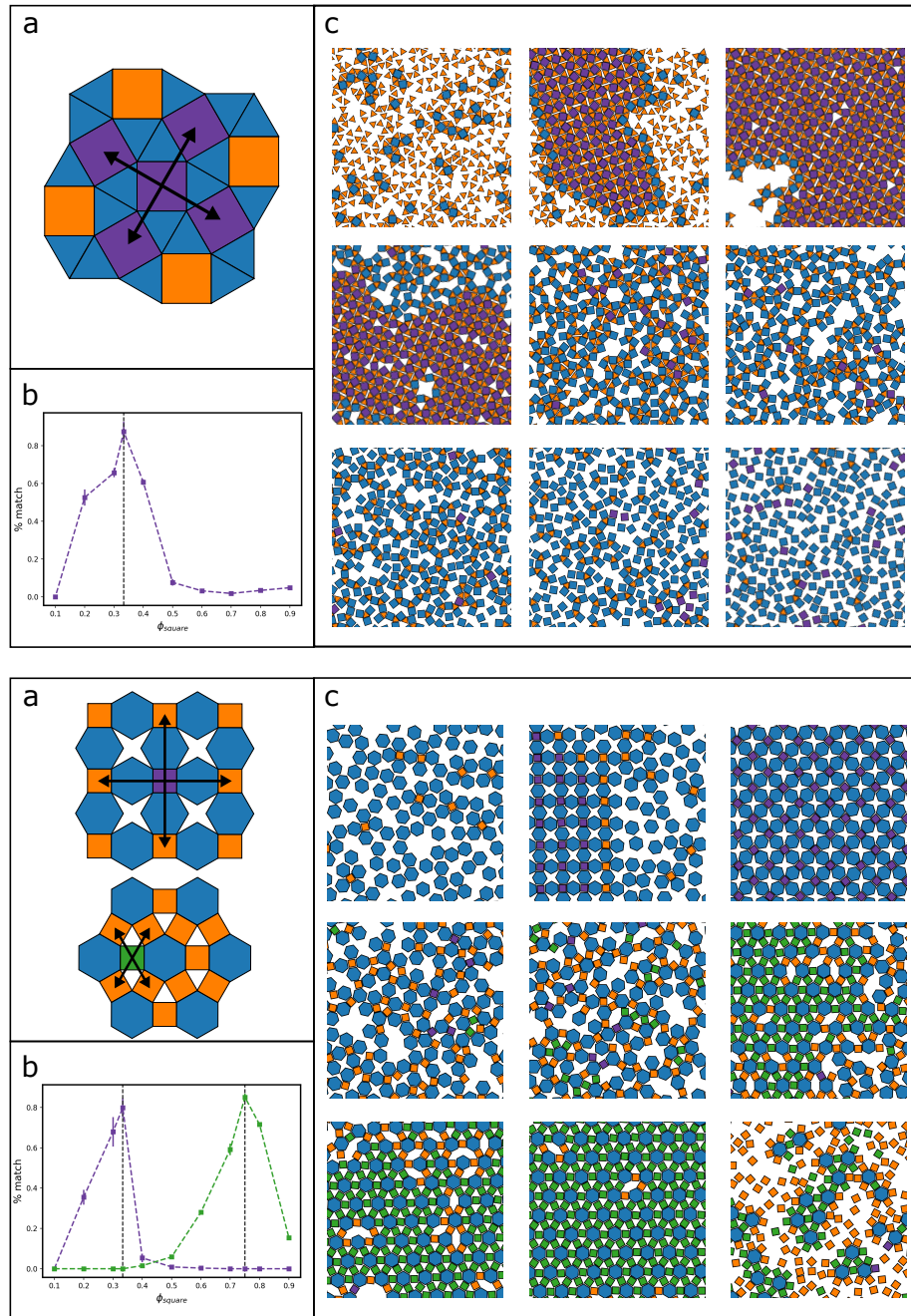
Figure 3.7: We demonstrate the effect of stoichiometry on two different particle pairings. First, we demonstrate the formations of the snub square tiling motif (top, a) and calculate the number of squares matching that environment as a function of the stoichiometry (top, b). We present snapshots of simulations where $\phi_{square} = 0.1, 0.2, 0.333, 0.4, 0.5, 0.6, 0.7, 0.8, 0.9$ (left-to-right, top-to-bottom) (top, c) and squares matching that environment are colored purple. Next, we demonstrate the way stoichiometry controls the formation of two different lattices, the motifs of each are shown (bottom, a) and the number of squares matching each environment as a function of the stoichiometry (bottom, b). Finally, squares are colored by which environment they belong to where $\phi_{square} = 0.1, 0.2, 0.333, 0.4, 0.5, 0.6, 0.7, 0.75, 0.9$ (left-to-right, top-to-bottom)) (top, c).

46

3.5(bottom), we observe that moving from a two- to three- to six-patch hexagon drops the void fraction when paired with three-patch triangle Figure 3.5(a, b, c) and with any other symmetrically-binding hexagon. The ability to control the void fraction is useful in many material applications where robust control over pore size is critical.

3.4 Conclusions

We have demonstrated that in the large space of anisotropic-patterned regular polygons that one can extract a series of design principles that allow for targeting of specific morphology, and that these rules can be used to target open structures desirable in material applications. Rules for terminal structures allow us to access exotic shapes which may be experimentally difficult to access and that such shapes can be utilized in higher-order processes for forming open structures. Our rule for lattices informs us of what shape patterning are most likely to form lattices and from this, we learn that void fraction drops with the addition of patches. Our ring rule gives us the most effective way to access open structures and informs us of the best ways to avoid kinetic traps during formation. All of these rules we also shown to work outside of the realm of triangles and squares, and may give experimentalists a road map to designing the open structures required for novel material properties.

CHAPTER IV

Dendrimer Ligand Directed Nanoplate Assembly

This chapter is adapted from Ref. [82], a publication in ACS Nano, authored in 2019 by K. C. Elbert*, T. Vo*, N. M. Krook, W. Zygmunt, J. Park, K. G. Yager, R. J. Composto, S. C. Glotzer, and C. B. Murray (* indicates co-authorship). My major contributions to this work included contributing to design of simulation protocol and testing (Section 4.3.3) as well as discussions/contribution to the story of the paper.

4.1 Introduction

Anisotropic nanocrystals (NCs) have been employed to create a wide variety of assembled superlattices, giving access to novel properties of the resulting films [93, 94, 95]. Control and uniformity of film architecture is of the upmost importance for NC technology; however, there is still much to be understood about the formation of these assemblies. Contributing factors during assembly include NC-NC interactions [30, 74, 96], NC shape [10, 97], ligand effects [98, 99, 100], and fabrication method, which encompasses a variety of variables such as subphase polarity [101, 102], drying rate [103], and electric fields [104, 105]. Although many of these factors have been investigated previously, typically, these studies utilize commercially available organic ligands, whereas few examples exist for intentionally designed combinations [18, 106], particularly for anisotropic NCs. It is well-known that self-assemblies of NCs rely

on both organic and inorganic components of the NC building blocks [107]; however, ligand design and direct comparisons to elucidate ligand effects on NC assemblies still remain a rich area for research into diverse superlattices.

Ligand effects on NC assembly can be emphasized by employing anisotropic NCs, as differences between ligand grafting densities on various facets of the NCs can have a large effect on the resulting assembly [106, 108, 109]. Previous work has shown that longer ligands of DNA preferentially bind to different faces of NC cubes due to ligand-igand interactions on the surfaces of the NCs [81]. Simulation and theoretical approaches aimed at characterizing the degree of ligand partitioning as a function of faceting and relative curvature have revealed a critical interplay between ligands and the core geometry that results in the formation of nontrivial ligand shells [79]. Self-assembly into larger superlattices is then influenced by such anisotropic coronas, resulting in various symmetry-breaking morphologies that have not been previously observed [21, 81].

A variety of plate assemblies due to ligand or organic surfactant effects have been observed in previous studies for 3D micron-sized superstructures [110, 111]; however, investigations of thin films have largely focused on 2D assemblies in monolayer films [112]. In this work, we investigate ligand effects on anisotropic NC assembly through the use of dendrimer ligands of varying generation and cone angle in combination with rhombic plate NCs. The resulting films were analyzed with transmission electron microscopy (TEM) and grazing-incidence small- and wide-angle X-ray scattering (GISAXS and GIWAXS) to further describe their structure. Multilayered self-assembled films exhibit a distinct, highly controlled, offset architecture between layers of NCs, where the amount of offset increases with increased steric bulk of the ligand grafted on the surface of the NCs. Monte Carlo (MC) and molecular dynamics

(MD) studies were conducted to elucidate the formation of these structures, explicitly accounting for nonuniform grafting densities on the anisotropic NCs. The results of these simulations show that ligand structure and steric interactions are both important considerations for NC film design, particularly for anisotropic NCs, as we aim to further understand these principles to effectively employ rational engineering of choice systems.

4.2 Methods

4.2.1 Modeling of Ligand Corona and Lattice Energy Computation

Here, we adapt a scaling theory developed for grafting of linear ligands to an anisotropic core to account for nonlinear ligands. We define a chain swelling parameter, α, that explicitly accounts for chain branching ($\alpha^5 \ N^{1/2}\text{v}[N\Lambda]^{-\frac{3}{16}}$), where N is chain length, v is excluded volume, and Λ is the degree of branching. The derivation for the scaling theory using the new swelling parameter is analogous to that of linear chain. Scaling analysis gives the free energy of ligand grafting at various positions on the particle surface that can then be used as a Boltzmann weight factor for the probability of chain grafting P. A metropolis algorithm was then employed to place chains onto the particle surface, weighted by P. The number of chains grafted are set by the grafting density. The effective corona is then computed from averaging over 1×10^6 MC simulated coronas. PMFs are then calculate between two particles with explicit coronas at various positions and relative orientations. The computed PMFs are then feed into the Wertheim-style lattice prediction approach proposed by Lu et al. to compute the excess free energy of lattice formation relative to a bare particle limit [81, 113, 114, 115, 116].

4.2.2 Molecular Dynamics Simulation of Ligand-Grafted Particles

We first compute the partitioning probability of ligands on the surface of the nanoplate. This is performed via generating grid points on the particle surface and computing partitioning probability from our scaling theory. A set of potential mean forces was then computed between two grafted particles. While exact, creating a unique bead type for each point, the particle surface becomes prohibitively expensive for a molecular dynamics simulation. To reduce the complexity, we categorize the continuous probability distribution into three distinct groups based on the value, P, of the scaled grafting probabilities: low for $P \in [0, 0.33)$, medium for $P \in [0.33, 0.5)$, and high for $P \in [0.5, 1]$. NVT simulations are then performed at $T^* = 0.5$ for a system of 2744 NCs. Each NC contains roughly 100 beads making up the rigid body, giving a total of 274,400 particles in each simulation. A driving force was applied to each particle to push them to a wall (mimicking the liquid-air interface) placed at the top of the simulation box. The wall also has an LJ-type interaction with the beads making up the NC. The driving force was turned off after 1 M time steps, at which time there are enough NCs at the interface to nucleate crystallization. The system was then allowed to further equilibrate for 5 M time steps, followed by a production run of 10 M time steps.

4.3 Results and Discussion

4.3.1 Component Design

A series of ligands were designed and synthesized to study how different generation and cone angle of dendrimer ligands affect NC self-assembly. The complete series is shown in Figure 4.1, where two different generations, as well as different cone angle, or steric bulk, within the same generation are highlighted. This series allows for a

direct comparison of the effects of these ligands on NC self-assembly processes. The specific ligand architecture used in this study was selected based on excellent control of NC assemblies previously studied, where interparticle spacing could be controlled effectively based on dendrimer generation [117]. Additionally, the larger generation dendrimer provided sufficient steric bulk to overcome NC-NC attractive forces to maintain interparticle spacing across various spherical particle sizes [117, 118]. Given the structure of dendrimer ligands, they can provide surface protection of spherical particles, as they can pack effectively around a curved surface due to their cone angle [119]. These previous findings lead to questions of how ligands of these geometries bind to the surfaces of anisotropic NCs, and if their distinct geometries can lead to distinct or precisely controlled NC assemblies.
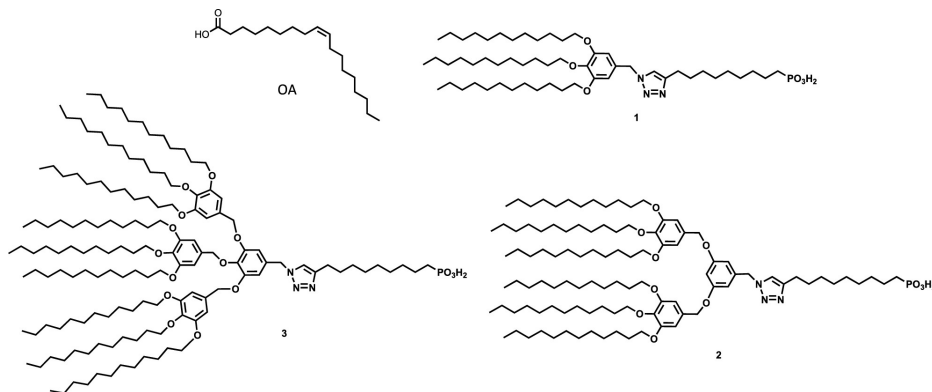
Figure 4.1: Structures of dendrimer ligands 1, 2, and 3 and oleic acid (OA) used in this study.

Complete synthetic details for the series of ligands used in this study are described in the Supporting Information. Briefly, using a similar synthetic strategy as was previously utilized due to its synthetic tunability [117], targeted molecules 2a and 3a were obtained by reacting 5-(chloromethyl)-1,2,3-tris(dodecyloxy)benzene with 3,5-dihydroxybenzoate or methyl 3,4,5-trihydroxybenzoate, respectively, using Williamson etherification. The subsequent esters were reduced with LiAlH$_4$, chlorinated, and then reacted with NaN$_3$ to obtain valuable intermediates 2d and 3d. To

attach the selected surface binding group, phosphonic acid, which is known to bind to rare-earth-based NCs [120], "click" chemistry was used to isolate final ligands 1, 2, and 3 [121].

Separately, NCs of Gd$_3$:Yb/Er (20/2 mol %) were synthesized using previously reported methods [95, 120, 122].These NCs are rhombic plates that have dimensions of 16.6 and 19.8 nm on their short and long sides, respectively, with a thickness of 3 nm, and have oleic acid (OA) on their surfaces after synthesis. Subsequently, the NCs were functionalized with each of the various dendrimers using a ligand exchange procedure [123] where the structure of the inorganic NCs is unchanged. Previous studies have used NMR to confirm the successful ligand exchange procedure [117]; however, the paramagnetic nature of the NCs in this study limits the characterization techniques. Successful ligand exchange was confirmed by thermogravimetric analysis [120] where NCs functionalized with OA show the organic decomposition at 190°C, whereas the dendrimer ligands all decompose above 300°C. This is additionally confirmed by observation of increased interparticle spacing of NC assemblies, which will be discussed in detail in the following discussion.

4.3.2 Interfacial Assembly

These dendrimer-NC hybrid materials (denoted ligand@NC) were then assembled using a liquid-air interface method [124], where subphases of varying polarity were investigated, as the Murray group has previously shown that the subphase of the assembly can tune the NC orientation, parallel or perpendicular, relative to the surface [101]. For the case of OA@NC, on commonly employed diethylene glycol, the NCs assemble into a mixture of columnar and lamellar grains, which corresponds to the NCs aligned either parallel (face-on) or perpendicular (edge-on) to the surface, respectively; however, the lamellar structure is the dominant film orientation, as

shown in Figure 4.2(a). This confirms previous findings, where a less polar subphase, such as tri- or tetraethylene glycol, favors the columnar structure and a more polar subphase directs the NCs toward a lamellar liquid-crystalline structure. The lamellar orientation was attributed in part due to the hydrophobicity of OA, as this would create repulsive interactions between the ligands and polar subphase.
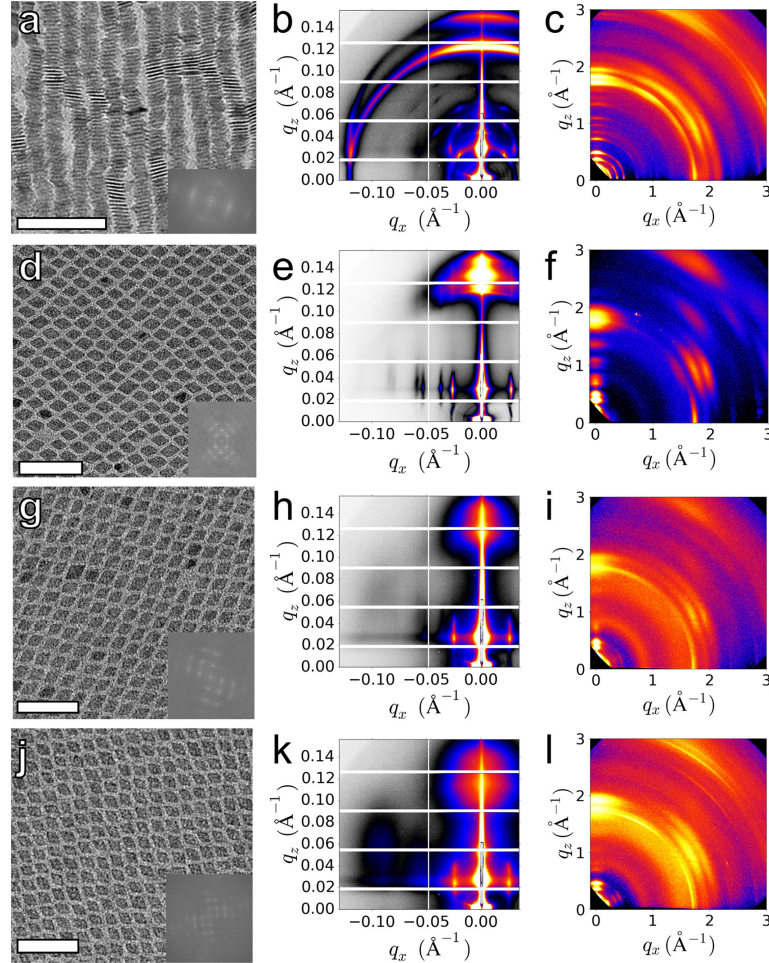
Figure 4.2: (a) TEM image of self-assembled OA@NC with calculated fast Fourier transform inset. (b) GISAXS and (c) GIWAXS of the same film. (d) TEM, (e) GISAXS, and (f) GIWAXS of self-assembled 1@NC. (g) TEM, (h) GISAXS, and (i) GIWAXS of self-assembled 2@NC. (j) TEM, (k) GISAXS, and (l) GIWAXS of self-assembled 3@NC. Scale bars are 100 nm.

Interestingly, for each dendrimer ligand, the dendrimer-NCs only align parallel to the subphase for each subphase investigated, shown in Figure 4.2(d, g, j). In all cases, the same assembly architecture is observed. Four subphases of varying polarity

were selected: ethylene glycol, diethylene glycol, triethylene glycol, and tetraethylene glycol. Due to the hydrophobicity of the ligands studied, it was hypothesized that an extension of previous results would be observed, as there should be an increase in the repulsive interactions between the ligands and a polar subphase. However, this change in monolayer orientation suggests that there must be additional factors during the self-assembly process that have a strong influence on the final film morphology. Thus, further characterization of this film morphology was conducted to fully assess the films.

The addition of the dendrimer ligands also allows for monolayer films to be achieved, a challenge that was not easily accomplished in previous studies, as these NCs form multilayer films rapidly due to their interparticle attractive forces [101]. Successful monolayer assemblies exhibit the same film architecture, with only changes in the interparticle spacing. The interparticle spacing measured for 1@NC from TEM images is 5.39 0.71 nm, whereas it increases to 6.28 1.17 and 6.89 0.87 nm for NCs with larger ligands 2 and 3, respectively.

These films were characterized using GISAXS and GIWAXS, allowing for a complete investigation of centimeter length-scale films transferred onto silicon wafers, confirming film uniformity, as well as the interparticle spacing and particle orientation in the films. The 2D GISAXS images are shown in Figure 4.2, highlighting the difference between panel b (OA@NC) and panels e, h, and k (1@NC, 2@NC, and 3@NC). The peak positions from these GISAXS patterns show the differences in NC alignments and are further confirmed qualitatively from the GIWAXS data. Films formed on each of the subphases were analyzed with GISAXS.

Line cuts along the in-plane direction, q_r, are shown in Figure 4.3, where fitting the primary peak was used to determine the repeat-spacing value for each lattice.

For the case of OA@NC, the value from the primary peak of the line cut in this direction provides the stacking distance in the z-direction, as the plates are edge-on to the substrate. As 1@NC, 2@NC, and 3@NC are all face-on to the substrate, fitting the primary peak in these cases provides the plate-to-plate distance in the xy plane, which are 4.7, 5.2, and 5.7 nm, respectively, in good agreement with the measured distance from TEM.
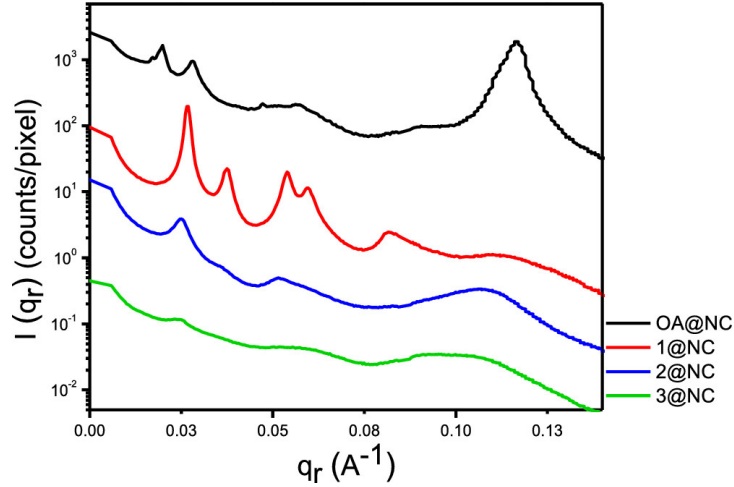
Figure 4.3: Line cuts for qr values from 2D GISAXS patterns shown in Figure 4.2.

For multilayer films, typically the NC-NC interactions dictate NC alignment into a columnar architecture when the NCs align face-on to the substrate [101]; however, when the dendrimer ligands are grafted onto the surfaces of the NCs, a distinct architecture is observed. For each layer of the assembly, the particles are directionally offset, as highlighted in Figure 4.4, and this architecture can be achieved over large length scales. These films were characterized with TEM tilt tomography, as shown in Figure 4.4 where an offset of 18.4 2.4, 19.1 3.0, and 23.3 3.2% relative to the NC side lengths were observed for 1@NC, 2@NC, and 3@NC, respectively. This offset is calculated as the distance between the edges of the two plates in the bilayer, highlighted in Figure 4.4, and converted to a percentage compared to the slide length

of the NC. The observed architecture is most likely due to the large dendrimer ligands that were employed, as additional NC "softness" has been shown to lead to a variety of moir patterns and binary superlattices in NC thin films [117, 125]. With an increased "softness", the NC-NC interactions are diminished, making these differences in morphology of multilayer films achievable. However, no other 3D morphologies were observed, that is, changes in the architecture in the z-direction, as each layer of NCs was observed to be directionally offset from the previous layer. If NC "softness" is the dominant driving force of this morphology, it is expected that additional 3D geometries would be observed, such as a rotation between NC layers, as previous studies have shown a large variety of moir patterns present in similar NC systems [117]. This is due to an increase in the organic component in the overall NC material, or the "softness", which causes slipping between NC layers. Due to the high level of control of 3D assembly while employing such large ligands on the NCs, further investigation of how the ligands so effectively direct assembly was conducted.

4.3.3   Monte Carlo and Molecular Dynamics Simulations of Hybrid Systems

To elucidate the role of the ligands in the formation of this set of films and provide insights for future ligand and NC design, a series of simulations and theoretical predictions were performed. Previous studies involving the distribution of ligands on anisotropic particles have shown a natural partitioning of ligands to surface locations of increased curvature [17, 79, 80, 81]. This partitioning can be understood as follows: for moderate to high grafting densities, local crowding drives each ligand to extend to its fully stretched configuration. The effect of crowding is expected to be uniformly distributed for an isotropic core but not for an anisotropic core. At positions of high curvature on anisotropic particles, ligands can occupy a larger volume going radially outward while retaining the same solid angle. The increase in accessible volume re-
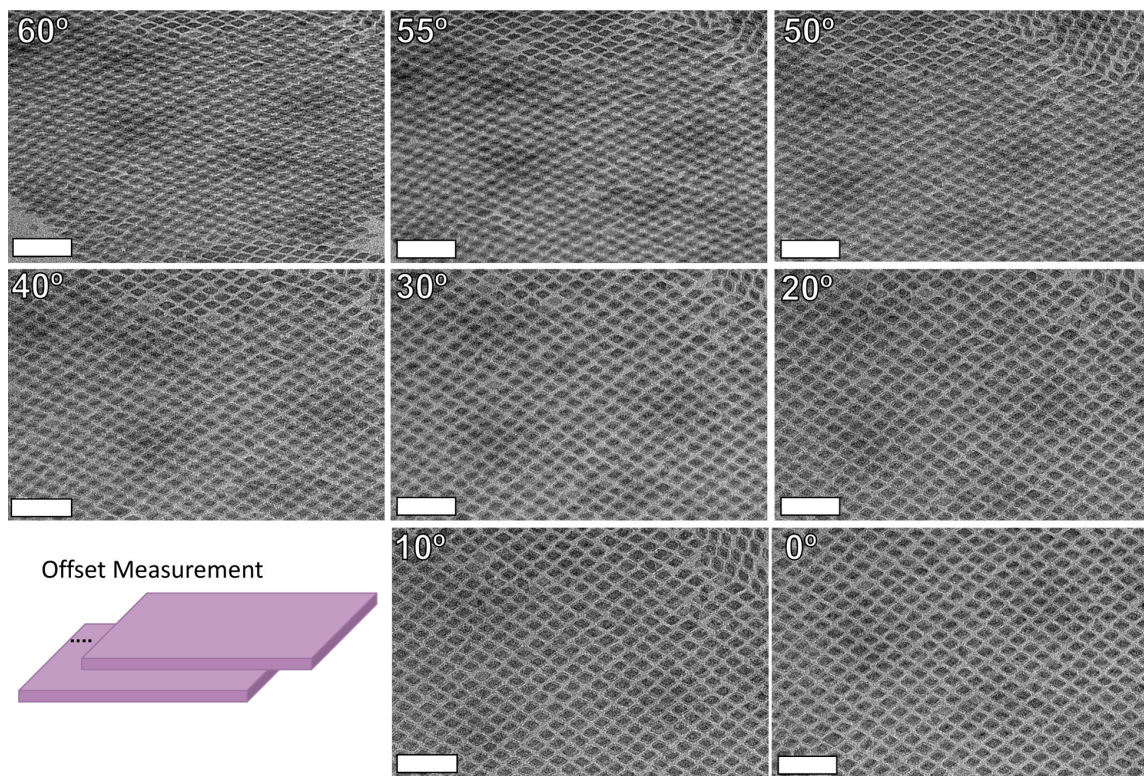
Figure 4.4: TEM tilt tomography of bilayer self-assembled 2@NC. Degree of tilt axis from the x-axis is provided in the top left, and a cartoon representing how the offset measurements were taken. Scale bars are 50 nm.

duces the degree of crowding felt by the ligand from its neighbors, allowing it to relax toward an equilibrium configuration. This gain in both rotational and translational entropy associated with ligand conformation exceeds the loss in configurational entropy due to ligand partitioning and results in an anisotropic surface distribution. To the best of our knowledge, theories developed to capture such transitions have focused on linear ligand architecture [17, 81]. A similar trend was demonstrated for models of simple ligands with large head groups [79], but for branching motifs, the degree to which ligand partitioning will be affected is unknown.

To provide insight into any additional forces that might emerge due to the branched ligand architecture and to quantify the degree of partitioning, we developed a scaling theory that explicitly accounts for the effect of nonlinear grafts through a combination
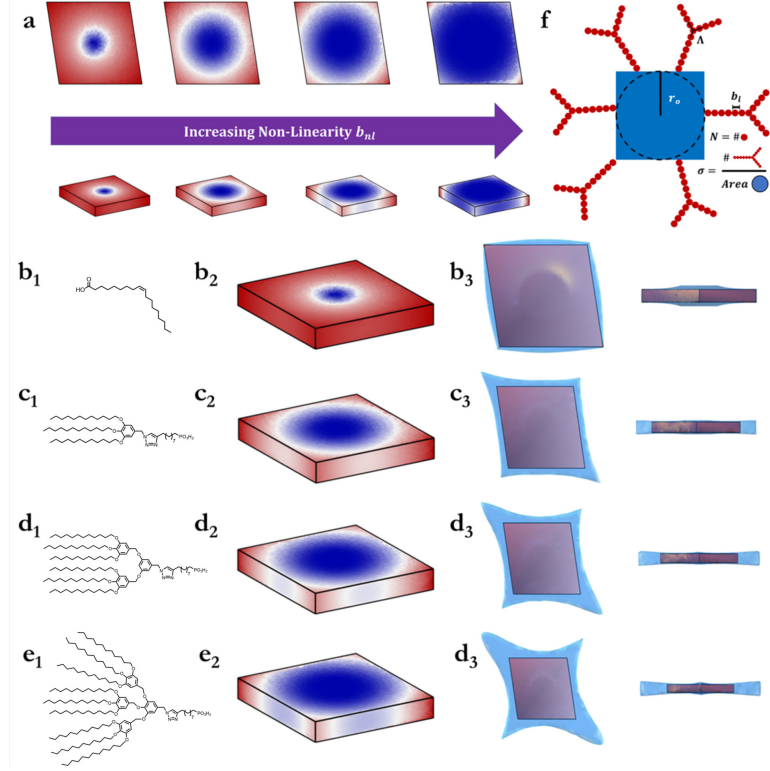
Figure 4.5: Scaling predictions for different ligand architectures. (a) Predicted ligand partitioning as a function of nonlinearity parameter b_{nl}. Colors indicate grafting probabilities (scaled between 0 and 1) at various locations on the rhombus surface. Top row shows a top-down view. Bottom row shows a side view (b-e). Predictions for the specific ligand synthesized experimentally. Subscript 1 shows the ligand; subscript 2 shows the partition probability for the given ligand; subscript 3 shows the effective ligand corona about the rhombus (f). Cartoon describing definitions of parameters employed. We observe more ligand partitioning as b_{nl} increases. The effective corona about the rhombus also transitions from conformal to concave, which then dictates the self-assembled morphology.

of both star polymer and branching scaling theories [81, 126, 127, 128, 129, 130, 131].

Our main result defines a ligand end-to-end distance that scales as

$$(4.1) \qquad R \sim r_o \sigma^{\frac{1}{5}} \nu^{\frac{1}{5}} b^{\frac{2}{5}} \left[\frac{Nb}{\Omega r_o} \right]^{\frac{3}{5}} \left[\frac{r_o \sigma^{\frac{1}{2}}}{N \Lambda \Omega^{\frac{3}{2}}} \right]^{\frac{1}{10}}$$

where r_o is the size of the in-sphere radius of the anisotropic core, σ is the core grafting density, b is the statistical segment length of the ligand, v is the excluded volume of the ligand, N is the degree of polymerization, and Λ is the effective degree of ligand nonlinearity. The parameter Ω is a shape term that defines both the shape

of the grafting core and specific position on the particle surface. R can then be used to define the free energy of a ligand at various positions on the particle surface as

$$(4.2) \qquad \beta F \sim \frac{R^2}{N^{\frac{7}{16}} \Lambda^{-\frac{1}{16}}} + \nu \frac{N^2 \sigma r_o^2}{(\Omega R)^3}.$$

The probability of finding a ligand at different surface position is simply

$$(4.3) \qquad P \sim e^{-\beta F}.$$

Figure 4.5(a) plots the predicted partitioning probability, P, projected onto the respective surface positions on the nanoplate for ligands of increasing nonlinearity. Here, coloring is scaled such that the location of lowest partitioning probability is set to 0 and the highest is normalized to 1. In the limit of a linear ligand (no branching), we predict a slight partitioning away from the center of the larger facets (top and bottom faces) and a near isotropic distribution about the smaller faces (along edges) of the NC. Increasing ligand nonlinearity augments the preference for the smaller faces but also produces a secondary partitioning toward the vertices associated with the longer diagonal of the NC. Comparison of linear to branched scaling behavior reveals that the observed secondary effect arises due to an increase in the effective size of the ligand's statistical segment length that can be directly quantified as

$$(4.4) \qquad b_{nl} \sim b_l \left(\frac{\sigma^{\frac{1}{2}} r_o}{N \Lambda} \right)^{\frac{1}{4}}$$

where b_{nl} is the effective size of the nonlinear ligand and b_l is the size of the linear ligand. A schematic further clarifying the definitions of the above parameters are shown in Figure 4.5(f). These results suggest that we can employ branching ligand architecture as an additional handle to fine-tune the surface partitioning of

ligands and possess a systematic, theoretical approach to estimate the effective increase in statistical segment size of nonlinear, grafted ligands relative to their linear counterparts.

The predicted probability, P, is then used to compute the average corona about the core. Briefly, the core is approximated as a series of surface mesh points that are roughly equidistant from each other. Each surface point has a ligand attachment probability P. A metropolis algorithm was then employed to place chains onto the particle surface, weighted by the probability. The number of chains grafted are set by the grafting density. The effective corona is then computed from averaging over 1×10^6 MC simulated coronas. Figure 4.5(c-e) shows the predicted partitioning and ligand coronas for the experimentally synthesized ligands scaled relative to a linear ligand (Figure 4.5(b)). As expected, we observe an increase in the grafting probability with increasing ligand nonlinearity (Figure 4.5(b2-e2)), which in turn tunes the effective corona morphology about the nanoplates (Figure 4.5(b3-e3)) [48]. Here, we show a top-down view on the left and a side view on the right. We note here that the coronas around the NC become increasingly nonconformal with increasing ligand branching. Additionally, the corona morphology near the vertices grows larger in the z-direction, producing an additional concavity in the top and bottoms faces of the NC. These nonconformal coronas highlight the nontrivial interactions between rhombus-shaped NCs that dictate the final self-assembled morphology.

We performed MD simulations of the ligand-grafted NCs across a wide range of ligand nonlinearity b_{nl} using the HOOMD-Blue simulation engine [50]. The predicted coronas (Figure 4.5(b3-e3)) indicate the likelihood of finding a ligand at a given surface position and are directly related to how that specific location interacts with another surface position on a neighboring particle. Thus, we can create a rigid body

of smaller surface beads that sit on the NC surface and attribute interaction strengths to each bead based on the grafting probability at their respective positions. To reduce the complexity of the simulation model, we categorize the continuous probability distribution into three distinct groups based on the value, p, of the scaled grafting probabilities: type A for $p \in [0, 0.33)$, type B for $p \in [0.33, 0.5)$, and type C for $p \in [0.5, 1]$. Interactions between each bead type are Lennard-Jones (LJ) with ε and cutoffs computed from our scaling theory. Simulations were then initialized with 2744 NCs isotropically distributed. Each NC contains roughly 100 beads making up the rigid body, giving a total of 274,400 particles in each simulation. A driving force was applied to each particle to push them to a wall (mimicking the liquid-air interface) placed at the top of the simulation box. The wall also has an LJ-type attraction with the beads making up the NC, again with ε computed from our scaling theory. Simulations were run in an NVT ensemble at $T^* = 0.5$. The driving force was turned off after 1 M time steps, at which time there are enough NCs at the interface to nucleate crystallization. The system was then allowed to further equilibrate for 5 M time steps, followed by a production run of 10 M time steps. The left panels of Figure 4.6 show the final simulation snapshots for systems ran at the b_{nl} parameters corresponding to the synthesized ligands, and additional viewpoints from these simulations are also provided in Figure 4.6. Comparison with experimental TEM images (Figure 4.6(b, d, f, right panels)) shows nice agreement between simulation and experimental results. For the nonlinear ligands, there is an experimentally observed offset between subsequent layers of the NCs below the liquid-air interface that is not present in the linear ligands. The amount of offset (scaled relative to the NC side length) observed in the experimental images is 18.4 2.4, 19.1 3.0, and 23.3 3.2% as compared with the values computed from our

simulations of 16.3 2.0, 18.6 2.0, and 20.2 2.0%.
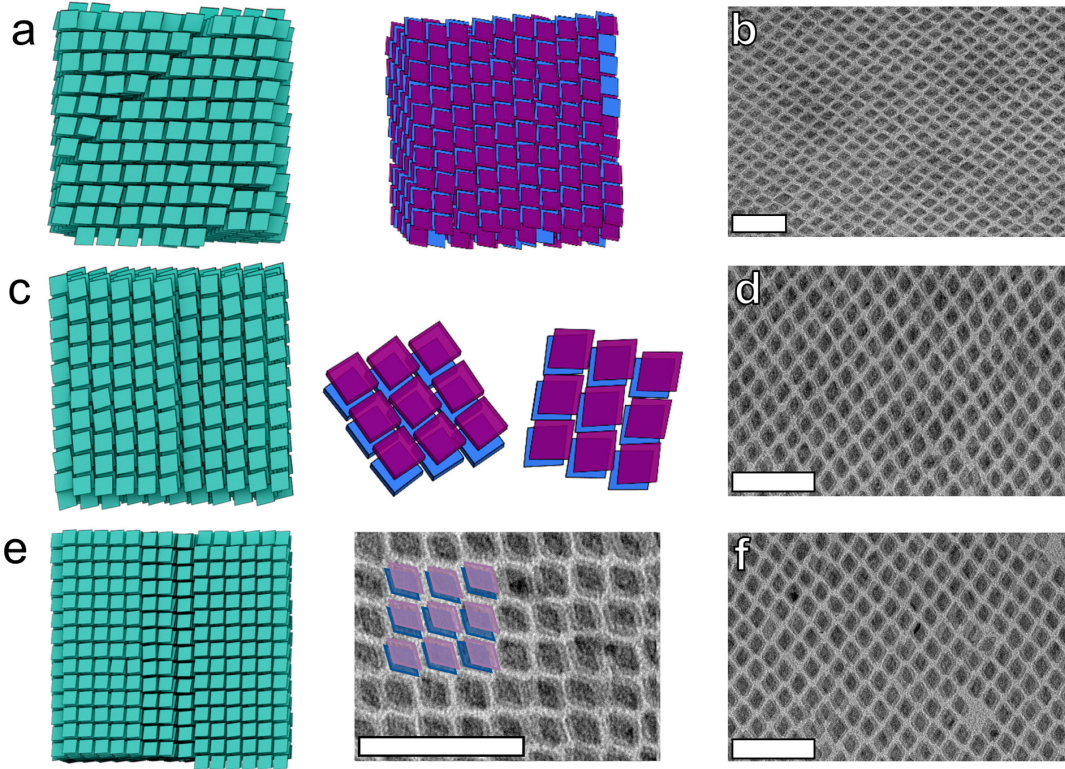
Figure 4.6: Comparison between simulation and experimental TEM images for multilayer assemblies: (a, b) 1@NC; (c, d) 2@NC; and (e, f) 3@NC. Analysis of the offset from simulation produces values of 16.3, 18.6, and 20.2 2.0% as branching increases, in good agreement with experimental values of 18.4 2.4, 19.1 3.0, and 23.3 3.2%. Additional images from simulations at various view points and microscopy with false coloring are provided to highlight NC offsets between layers. Scale bars are 100 nm.

To better explain the selective transitions between offset versus lamella stacking morphologies seen in both simulations and experiments, we utilize a Wertheim-like, first-order perturbation theory to predict the free energy of the NCs in both configurations, analogous to applications of Wertheim theory proposed by Lu et al. for DNA-mediated self-assembly [81, 113, 114, 115, 116]. Briefly, the theory calculates the change in the energy of formation for particles arranged on a lattice upon transitioning from a repulsive, "hard-particle" reference state to one where a given surface distribution of interaction sites gives rise to a net attraction. To properly capture the physics governing our NC system, we expand the range of solid angles available

to each surface site to interact with other particles in order to better model the more isotropic ligand-ligand interaction, as opposed to directed, hybridization driven interactions in DNA. Figure 4.7(a) plots the measured offset from simulations compared to theoretical predictions, revealing good agreement in the transition from a lamella to an offset motif at $b_{nl} \sim 3.5$. Figure 4.7(c1-c3) plots the predicted optimal sets of relative orientations and positions between the nanoplates using our theory at b_{nl} parameters of 1, 3, and 5, corresponding to a linear ligand, a nonlinear ligand before the transition, and a nonlinear ligand after the transition, respectively. For clarity, we visualize the NCs using their coronas to better represent how the shift in surface partitioning controls the observed morphologies.
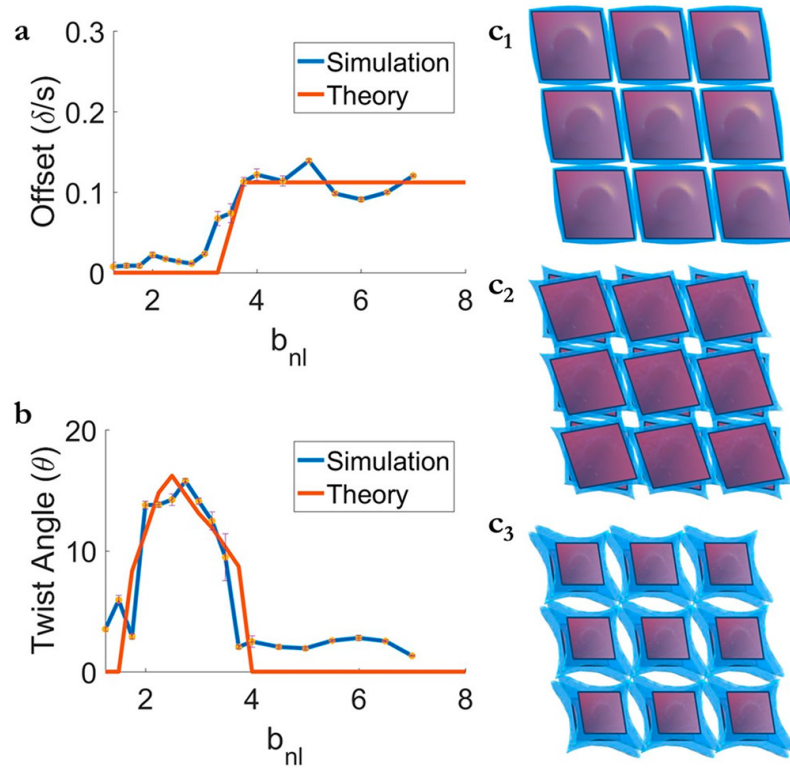
Figure 4.7: Theoretical predictions for lattice self-assembly. (a) Offset prediction as a function of ligand nonlinearity b_{nl} compared versus measured values from simulation. δ is the offset value, and s is the side length of the rhombus. (b) Prediction of relative twisting angle between layers as a function of ligand nonlinearity b_{nl} compared versus measured values from simulation. (c) Predicted lattice morphology for b_{nl} of 1 (c1), 3 (c2), and 5 (c3) corresponding to a linear ligand, a nonlinear ligand before the offset transition, and a nonlinear ligand after the offset transition, respectively.

Our results clearly indicate that the lamellae to offset transition is dictated by ligand crowding at the vertices with increasing graft nonlinearity (Figure 4.7(a)). For low crowding, particles can easily increase their net total ligand-ligand interactions with a slight twist relative to the layer above/below it. Twisting creates a lock-and-key interaction motif in-plane such that the vertex fits into the newly formed concave regions along the edge of the neighboring NCs while simultaneously creating additional vertex-vertex contacts with the layers above/below (Figure 4.7(c2)). However, as crowding increases, this simple twist is not enough. Ligands partitioned toward vertices on the nanoplate are forced to extend by an additional amount as indicated by larger protrusions observed in the coronas, thus increasing their interaction range (Figure 4.5(b3-e3)). Concurrently, increased partitioning leads to a deficit of ligand concentration toward the center of the NCs, creating a concave motif for the top and bottom faces (Figure 4.5(b3-e3)). The increased extension leads to more favored vertex-vertex interactions in-plane, untwisting the NCs. However, the face-face contacts with the layers above and below the particles are no longer favored, as the corona is now concave. As a result, the system shifts layers upward along the xy direction relative to the previous layer. This shift increases ligand-ligand interactions by introducing additional vertex-vertex contacts between layers. Furthermore, shifting places vertices with high ligand concentration closer to the center of concave faces belonging to particles below it, creating another lock-and-key motif that maximizes out-of-plane ligand-ligand interactions, analogous to the driving force governing offsets observed in graphene layer-by-layer stacking (Figure 4.7(c3)) [132]. Direct quantification of the degree of twisting between layers further corroborates the idea of lock-and-key driven transition as we again observe a peak in the twist angle in both simulation and theory (Figure 4.7(b)).

4.4 Conclusions

Ligand design plays an important role in NC applications, as they can direct many of the resulting properties of the organic-inorganic hybrid materials, including self-assembly of NCs. This work highlighted how varying dendrimer ligand generation and steric interactions can be used to tune NC orientation as well as interparticle spacing and offset between layers of NCs in multilayer films. These films were characterized using GISAXS to confirm the film morphology, as well as TEM tilt tomography. MC and MD simulations with ligand probability distributions obtained from scaling theory were used to elucidate the ligand grafting distribution on the NCs, and perturbation theory was employed to characterize the driving forces governing self-assembly. As a result, we now possess a detailed molecular understanding of the how to control architectures found in multilayer films. These studies emphasized how ligand grafting distribution is an important consideration when designing systems for self-assembly, particularly for anisotropic NCs. For NC plates, large ligands create a corona around the NCs, which force an offset architecture in multilayer films due to a lock-and-key type of motif. In 2D films, this ligand corona leads to the corners and edges of the NC plates having more repulsive interactions between the more polar subphase used for assembly, resulting in the NC plates assembling parallel to the subphase surface. Our findings not only emphasize the idea that an anisotropic graft distribution plays a crucial role in controlling self-assembly but provide a systematic way to theoretically predict the resulting morphology purely from experimental design parameters such as core shape, grafting density, solvent condition, and ligand architecture. Such a model serves as a natural input into an inverse design framework that will enable us to a priori select for the best set of

parameters to use in order to achieve a targeted self-assembled structure [133].

CHAPTER V

Inverse Design of Directional Nanotriangle Assembly Through Nanocube Doping and Co-Assembly

This chapter is adapted from a publication in preparation, authored by K. C. Elbert*, W. Zygmunt*, T. Vo, C. M. Vera, D. J. Rosen, N. M. Krook, S. C. Glotzer and C. B. Murray (* indicates co-authorship).

5.1   Introduction

Recent advances in synthetic capabilities have opened up access to an extensive library of experimentally realizable anisotropic nanocrystal (NC) building blocks [95, 134, 135, 136, 137] Consequently, successes in shaped particle synthesis have directed attention towards their usage in self-assembly as they have been shown to give rise to a wide range of exciting, emergent morphologies [5, 21, 138, 139, 140, 141]. However, a common hinderance to such an approach revolves around the high degree of kinetic traps along the path towards realizing a specific, targeted structure [142]. These kinetic barriers result from particles now having to balance their spatial as well as orientational distributions relative to each other. As a result, the current challenge lies not in synthesis but rather in defining design strategies aimed at selecting the optimal assembly parameters to reliably and reproducibly drive their ordering into targeted architectures.

In this regard, employing thin film assembly processes for NCs is highly desirable due to its ability to provide a high degree of order within films. This strategy has been utilized for to create films consisting of differing NCs, particularly binary superlattices, where NC shapes and ratios have been optimized to prepare films with stoichiometric amounts of each component [74, 143, 144]. However, while many of these studies have focused on NCs with either complementary NC composition or size, there are few examples of co-assembly of two distinct anisotropic systems [145, 146, 147, 148]. These anisotropic NCs are of particular interest, as NC orientation within a film has been shown to affect the overall properties of a material [101, 149]. Additionally, extensions to multicomponent materials are of specific interest as the ability to combine NCs of different compositions opens up access to metamaterials with enhanced properties [150, 151, 152, 153, 154]. Furthermore, the ability to dope controlled ratios of NCs into a film of dissimilar NCs would allow for a spectrum of stoichiometry to be realized [118, 155], providing an additional handle to tune the metamaterial's properties. However, similar to how adding orientational degrees of freedom produces kinetic barriers in the assembly of shaped particles, mixing in an extra building block species correspondingly results in extra barriers working against the formation of ordered morphologies. Control of NC orientation, interparticle spacing, and component ratio are all adjustable variables that contribute to co-assembly and film crystallinity in addition to NC composition, dimensionalities, and surface chemistry. The combination of kinetic traps, the large phase space of potential design parameters, as well as the ever increasing library of building blocks for multicomponent systems make it so that a systematic laboratory search across all possible combinations of assembly parameters is experimentally intractable. For these reasons, the reverse approach where we employ an

experimentally validated theoretical model to target the relevant design parameters for assembly is conceptually appealing.

Here, we take advantage of the success of our previous modeling approach for capturing the interfacial assembly of dendrimer coated nanoplates [82] as the underlying theory governing the selection of relevant parameters for the co-assembly of two anisotropic building blocks - two-dimensional triangular plates and three-dimensional cubes. Each building block is selected due to its size and shape uniformity, as well as for being distinctly different components, LaF_3 and PbTe, respectively. LaF_3 is a dielectric material that was selected as a two-dimensional building block due to its size and shape uniformity [156] as well as its size tunability. PbTe cubes were chosen as a model cube NC because of their optical and semiconducting properties [157, 158] as well as the interest in assemblies of cubes as models for anisotropic NCs [159]. These two materials are known to phase segregate within films and therefore provide a challenge in their co-assembly. We optimize across three experimental handles - ligand types, plate to cube stoichiometric ratio, and annealing temperature - and select for the composite set of parameters that counter-balance against the segregating tendency between plates and cubes. We then show that experimental realization of our choice of design parameters produce the targeted self-assembled morphologies. Lastly, we extend our developing principles of co-assembly to an example using two two-dimensional plates of differing shape: LaF_3 triangular plates and GdF_3 rhombic plates. These two materials typically phase segregate within films but by again changing the surface chemistry, we achieve co-assembly as well as the first example of substitutional doping with two anisotropic NCs.

5.2 Theory and Inverse Design

In order to understand the driving forces underlying the conditions required to drive interfacial co-assembly of cubes and triangular plates, we construct a phase diagram of relevant morphologies using a Wertheim-like thermodynamic perturbation theory (TPT). Briefly, our TPT calculations start by defining a "hard-particle" reference for cubes and triangular plates arranged in the various co-assembled morphologies of interest. The change in lattice free energy of formation is then computed by first assigning a distribution of interaction sites to both cubes and triangular plates. For any given distribution surface sites, a potential of mean force (PMF) can be computed between pairs of particles. We can then combine the PMFs and particle configurations (defined by the "hard-particle" reference) to compute the equilibrium constant for that lattice of interest as

$$(5.1) \qquad K = \prod_i \sum_j \frac{\rho_j^{s_{ij}}}{s_{ij}!} \int f_{ij}^{s_{ij}} g_{ij,c}(r) d\vec{r}$$

where the product over i is over the types of interactions in the system and the summation over j is over all particle types within each interaction types. $f_{ij}(r)$ is the traditional Mayer-f function obtained from standard cluster expansion procedure and is equivalent to $e^{-\beta V} - 1$ where V is the PMF. The product over interaction types is analogous to the classical thermodynamic limit of defining a net equilibrium constant for a series of reactions as the product of each reaction's individual equilibrium constant: that is $K_{net} = \prod_i K_i$. ρ is the system density, $g_c(r)$ is the radial distribution function of the reference state, and s is a coordination number defined by the given crystal structure. The pre-factor $\rho_j^{s_{ij}-1}/s_{ij}$ accounts for indistinguishably and probability of finding $s - 1$ particles that are of interaction type i and species j

within the cutoff interaction distance. A full derivation of the theory can be found in the SI of our previous works on DNA-mediated self-assembly [81, 160]. The lattice free energy of formation ΔG can then be computed via the standard thermodynamic relation $\Delta G = -kT \ln K_{net}$. We can then compute ΔG for the set of relevant competing structures for the cube/plate system and construct a phase diagram across the design handles of stoichiometric ratio and potential well depth (directly related to inverse temperature for experiments).

To evaluate Eq. 5.1, we first need to compute the PMFs for cube-cube (CC), plate-plate (PP) and cube-plate (CP) interactions. Doing so requires a selection to be made regarding the ligand grafted onto each particle. Previous experimental works have shown that oleic acid (OA) has been effective at direct colloidal assembly into a wide range of crystalline structure and therefore provides a good starting point for our study. In the limit of short oligomers like OA scaling arguments predict an isotropic ligand distribution on both cube and triangular plate surfaces [82] and the PMF between all interactions can be computed. To apply Eq. 5.1 we generate the reference radial distribution function $g_{ij,c}(r)$ by creating periodic images of the unit cell for each lattice to be tested and calculate the respective CC, CP and PP distribution functions. Evaluating Eq. 5.1 then yields the phase diagram shown in Figure 5.1(a). By inspection, theory does predict the formation of the desired co-assembly lattice. However, the size of the co-assembly regime is relatively small compared to those of competing structures, presenting potential challenges for experimental realization as assembly could get stuck in kinetic traps and form the competing lattices and this motivates us to reassess our selection of ligand type. Along this vein, recent studies on ligand mediated self-assembly have suggested that dendrimeric ligands can help enhance both the yield and stability of unary colloidal crystals [82, 119]. Taking

advantage of this knowledge, we now select for the simplest of a series of dendrimers, a polycatenar ligand, that a previous work has employed to successfully control the ordering of rhombus nanoplate self-assembly. Using the same scaling argument as before, we first determine the polycatenar (PC) ligand distribution on the surface of both cubes and plates and compute each respective CC, PP, and CP PMFs between particle pairs. Reconstructing the phase diagram now yields the result shown in Figure 5.1(b).
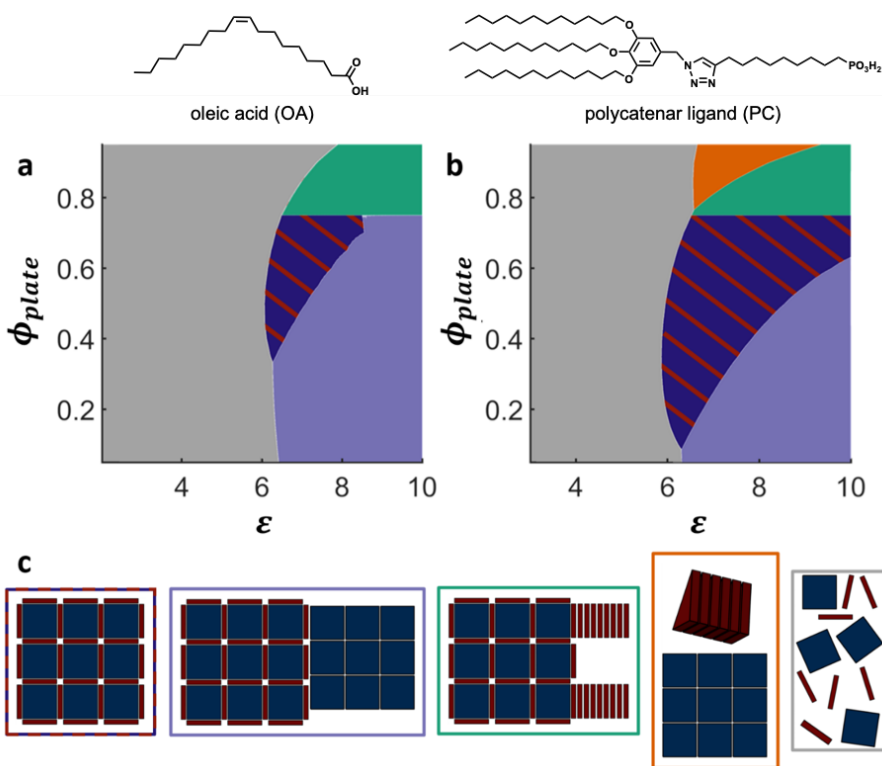
Figure 5.1: Phase diagram for cube and triangular plate co-assembly for (a) oleic acid ligand and (b) PC ligand with ligand structures shown above. (c) Representative snapshots of the crystal structures employed in construction of the phase diagrams with border coloring corresponds to each respective phase.

Direct comparison between Figure 5.1(a) and 5.1(b) reveals a large growth in the co-assembly region of interest along both the inverse temperature and stoichiometric ratio axis. To explain the fundamental driving forces governing the expansion in the co-assembly regime, we now dissect the composite term in Eq. 5.1 by overlaying

the individual $g_{ij,c}(r)$ for the co-assembled lattice of interest with their respective PMF. Additionally, we superimposed PMFs computed for OA and the PC ligand to highlight differences between predicted interactions, as shown in Figure 5.2(b-d).
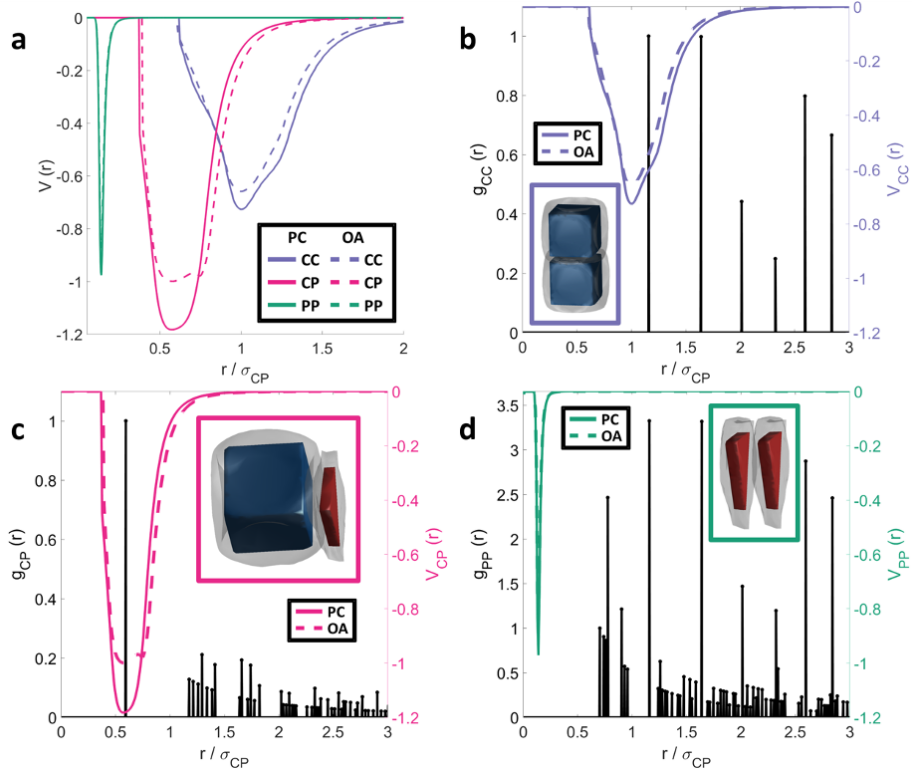
Figure 5.2: a). Computed potential mean force (PMF) for cube-cube (CC), plate-plate (PP), and cube-plate (CP) interactions. b). Radial distribution function for CC, $g_{CC}(r)$, overlaid with PMF for CC. c). Radial distribution function for CP, $g_{CP}(r)$, overlaid with PMF for CP. d). Radial distribution function for PP, $g_{PP}(r)$, overlaid with PMF for PP. All PMF are the for relative orientational between particles shown in the inset for b)-d). For all panels, dashed lines indicate PMF for oleic acid (OA) and solid line is PMF for polycatenar ligand (PC).

Before we compare the differences between PMFs for oleic acid versus the polycatenar ligand, it is instructive to note several interesting features that emerge from both sets of PMFs in Figure 5.2. The most striking observation is that the computed PMFs show the strongest net attraction for CP interactions. The naive expectation is such that CP and PP interactions should be on par with each other as both interactions are dictated by the larger facet on the triangular plate. However, for CP interactions, the plate's face only takes up roughly 43% of the cube's face, leaving

excess ligands to interact with those occupying the edge faces on the plate. This additional face-edge contact serves to favor CP over PP interactions (as seen in the computed PMF), pushing the system to favor co-crystallization. Furthermore, within the co-assembled lattice, all PP contact distances - peaks in $g_{PP}(r)$ - fall well outside the interaction range as defined by the PP's PMF (Figure 5.2(d)). On the other hand, the first peak in $g_{CC}(r)$ does fall inside the range of the computed PMF for CC (Figure 5.2(b)). Physically, these features suggest that CC interactions further stabilize the co-assembled lattice. In other words, the introduction of cubes into systems of triangular plate serves as a handle to tune plate assembly. Due to the strong CP face-face interactions, introducing cubes into the system induce a favoring of face-face contacts between cubes and plates. Now the system simply builds off of the initial cube-plate motif to account for varying cube to plate stoichiometric ratios. PP interactions win for low cubes fraction, driving the stacking of plates away from a cube's face. In other words, cubes serve as the nucleation sites for growing perpendicular PP stacking. Upon increasing cube concentration, the CC interactions start to contribute, shifting the system towards co-assembly as the resultant morphology provides more CP interactions while simultaneously gaining CC contacts.

We now discuss the enhancement in the region of co-assembly stability upon transition from oleic acid to the polycatenar ligand. By inspection of each respective PMFs show in Figure 5.2(a), we see that the CP interaction well depth is significantly deeper for the polycatenar ligand than oleic acid, whereas both CC and PP remain relatively the same. Within the morphologies tested in the construction of our phase diagram, the co-assembly lattice favors CP contacts the most as it is the dominant interaction driving the lattice stability. As a result, the significantly lower CP potential well serves to increase its composite free energy of formation and

thereby broadening the co-assembly regime. The origin of this deeper potential well can be further understood through visualization of the ligand corona about each particle (insets of Figure 5.2(b-d)). Switching to the polycatenar ligand results in the formation of a dimple in the corona at the faces of each cube. This dimple enables the plates to sit slightly closer to the cube as compared to a flat corona limit. Bringing the plate closer to the cube has the additional benefit of further enhancing the face-edge contacts discussed previously. Thus, switching to our preferred ligand creates an emergent lock-and-key type binding between cubes and plates through the interplay between the shape of each particle's respective ligand shell, ultimately resulting in the lower well depth as compared to OA. For these reasons, theoretical calculations would favor the usage of the polycatenar ligand over oleic acid for co-assembly and we select design parameters in stoichiometry and temperature based on the computed phase diagram in Figure 5.1(b).

5.3   Monte Carlo Simulation

To verify the morphology predicted via thermodynamic perturbation calculations, we employ Monte Carlo simulations of triangular nanoplates and nanocubes using the HOOMD-blue simulation engine [83]. We selected several plate fractions ($\phi_{plate} = [0.20, 0.40, 0.60, 0.80]$) and inverse temperatures ($\varepsilon = [6, 7, 8, 9]$) and ran simulations at statepoints defined by these parameters. Our Monte Carlo simulations attempt translational and rotational moves of particles according to the Metropolis criterion. We implemented the above potential of mean force for the particles decorated by the polycatenar ligand by using a square well potential between particles, where the interaction strengths are scaled by the relative well-depths of the various interaction types and the surrounding ligand corona determines the interaction ranges.

76

In each simulation, N=1728 particles were placed into a 3D periodic box, with ϕ_{plate} stoichiometry and inverse temperature of ε. Gravitational force was applied in the z-direction to push particles to the bottom of the simulation box in to model self-assembly at the interface, and walls were placed at the top and bottom of the simulation box to prevent particles from passing through the periodic boundary at in the z-direction. Initially, particles were simulated for 1M timesteps with no potential applied to randomize them from their initial configuration. Next, particles were simulated for 20M timesteps with a small oscillation implemented around ε to simulate thermal annealing; this oscillation allows for the breaking up of kinetic traps and the eventual equilibration of the simulation, noted by a flattening of the total energy of the system.

We then characterized the morphology of our system by analyzing the radial distribution function (implemented in Freud [86]) of the bottom layer of particles in the simulation box. Simulations in confinement were initially attempted where particles were initialized into a 3D box but quickly compressed into a quasi-2D single layer, where the layer thickness was that of a single cube height, but such simulations were inundated by kinetic traps where plates could not force themselves into the space between cubes, and therefore were not representative of the planned experimental approach. To better capture the experiments, we opted for the gravity-driven simulation approach where plates and cubes are free to move in and out of the bottom layer. Snapshots of the bottom layer of the simulation box were rendered using Ovito [161] and can be found in Figure 5.3.

In Figure 5.4, we demonstrate the contribution to g(r) as we modulate the system parameters. Pie charts indicate the major contributions to the final assembly in the bottom layer by computing the contributions of the PP, CP and CC peaks to
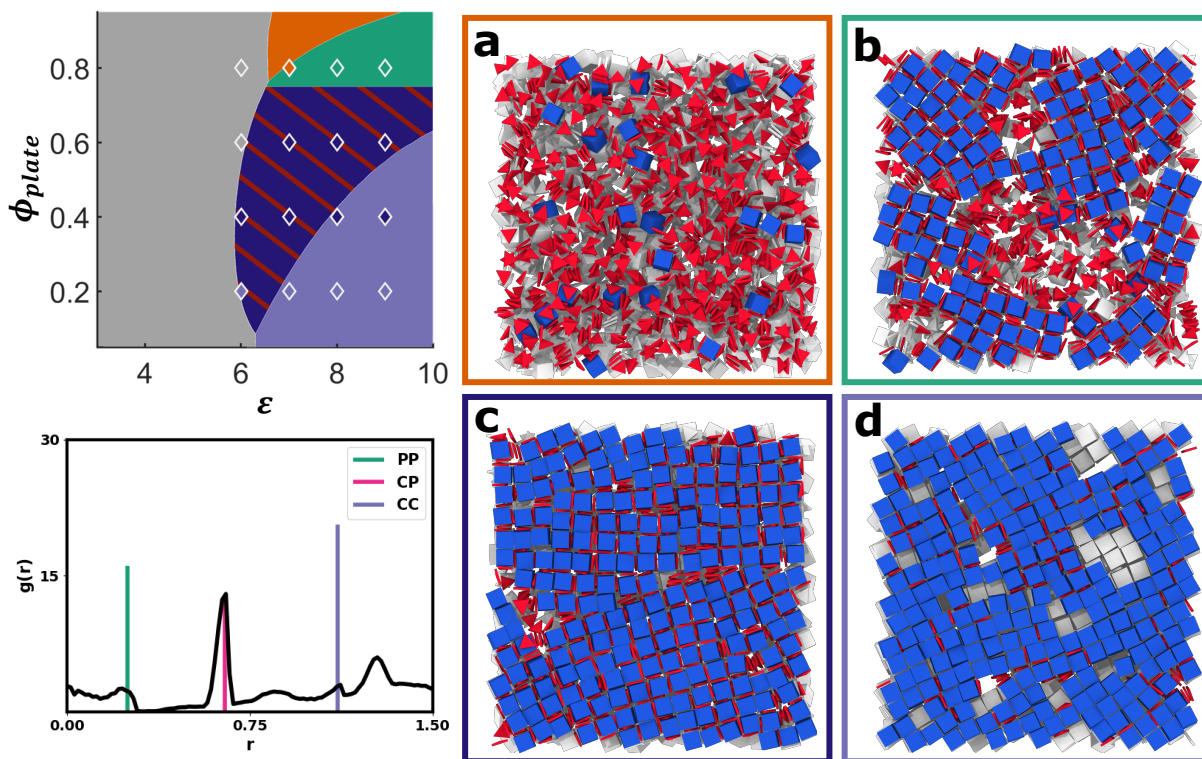
Figure 5.3: Results of Monte Carlo simulations for various (ϕ_{plate}, ε). The theoretical phase diagram is overlaid by diamonds representing the matching phase (top left). We include snapshots of the bottom layer of the simulation box (right) representing statepoints of (0.8, 7.0) (a), (0.8, 8.0) (b), (0.6, 7.0) (c) and (0.2, 8.0) (d). Grey particles indicate particles not included in the bottom layer. Colored outlines represent the phases that best match the snapshot. We demonstrate that the radial distribution function can identify peaks corresponding to PP, CP and CC interactions (green, magenta and purple peaks) ($g(r)$ shown for (0.6, 7.0)).

the summed peak height. In the cases of (0.8, 6.0), (0.8, 7.0) and (0.6, 6.0) no long-range assembly occurs and peak contribution is dominated by phase separated PP interactions. We observe places where co-assembly is the dominant contributor (CP>50%) as well as places where two phases make up comparable percentages of the sum of peak heights. Overall, these charts allow us to reliably determine the morphology for different combinations of ϕ_{plate} and ε and gives us confidence that the theory can reliable predict the accurate thermodynamic phases.
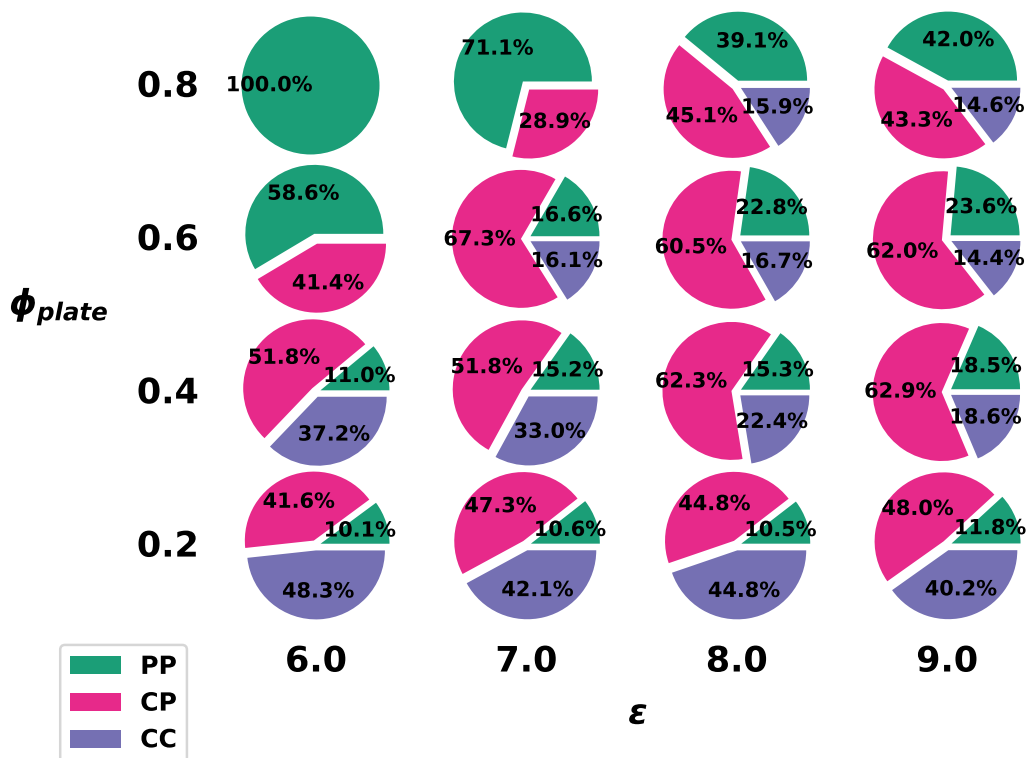
Figure 5.4: We demonstrate the various contributions to the final assembly by computing the contribution of peaks at PP, CP and PP respectively for various (ϕ_{plate}, ε). Dominant phases are identified by comparing their relative contributions to the sum of peak heights.

5.4 Interfacial Assembly

To best follow the theory laid out above, the size of each NC component was op-timized to be complementary to each other, where the PbTe cubes have edge lengths of 17.7 ± 1.1 nm and the LaF$_3$ triangular plates have edge lengths of 25.4 ± 2.1 nm and are about 2 nm thick. The liquid-air interfacial assembly method was employed to assemble all films for these studies [124]. First, for the case of single-component LaF$_3$ films, the orientation of the triangular plates can be effectively controlled by changing the polarity of the subphase, in a similar manner to previous results for other platelet NCs [82, 101].To achieve assembly with a columnar morphology, where the triangular plates are oriented parallel to the surface, a non-polar subphase is em-

ployed, such as tetraethylene glycol, as shown in Figure 5.5(b). When a more polar subphase, such as ethylene glycol, is selected, the triangular plates align perpendicular to the surface, shown in Figure 5.5(c). This phenomenon is attributed to repulsive interactions between the surface ligands and the polarity of the subphase. However, after ligand exchange with the larger, more hydrophobic polycatenar ligand, shown in Figure 5.1, the only morphology observed is parallel to the subphase, and multilayer films have an offset architecture, both of which are consistent with similar studies using this ligand on nanoplates [82].Successful ligand exchange is confirmed with both changes in assembly behavior as well as thermogravimetric analysis.
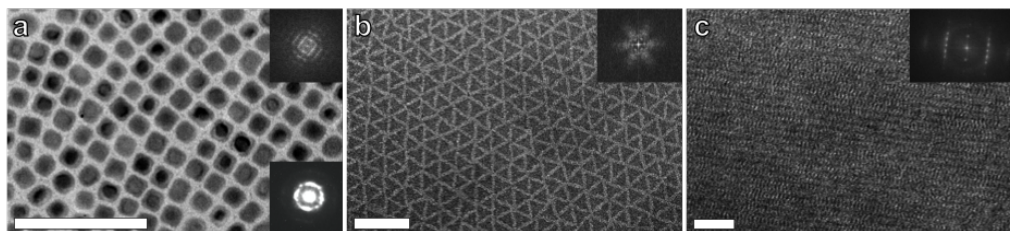
Figure 5.5: Single-component NCs self-assembled with oleic acid as the capping ligand. (a) PbTe with SAED inset in lower right corner, (b) LaF3 assembled on tetraethylene glycol, and (c) LaF3 assembled on ethylene glycol forming lamella morphology. Scale bars are 100 nm, FFT images are upper right corner insets.

Initial attempts at co-assembly of the cubes and triangular plates were initially unsuccessful when the native ligand, Oleic Acid (OA), was on the surfaces of the NCs. Limited co-assembly was observed, which provided initial evidence that the cubic PbTe could control the orientation of the LaF_3. However, for the majority of a sample, significant aggregation of the PbTe was observed, as well as the loss of NC morphology. While these effects were not taken into account when creating the model to guide these experimental efforts, they add to the difficulty of obtaining co-assembly with the limited co-assembly area shown in the phase diagram in Figure 5.1. Previous work has shown that polycatenar ligands can be effective protecting surface ligands for NCs [119], leading us to hypothesize that employing these ligands

would help to maintain NC morphology and prevent aggregation during mixing and assembly. Additionally, these ligands have been shown to bind preferentially to corners and edges of NC plates [82], as discussed above, which provided further motivation for their use, as having a larger density of ligands on the corners and edges of plates should increase their face-face interactions during assembly and guide a lock-and-key type mechanism for assembly.

Utilizing the polycatenar ligand on only the PbTe cubes did in fact provide improvements with NC stability as well as co-assembly. However, when the polycatenar ligand was grafted onto the surface of both components, true successful co-assembly was obtained, shown in Figure 5.6. This finding is consistent with previous results, as having ligands with similar tail groups minimizes repulsive forces [118], as well as confirming that having a non-uniform ligand corona around the NCs could guide as assembly more effectively. Additionally, it highlights that synthesizing NCs with complementary dimensions is not enough for successful co-assembly, and that optimizing the surface chemistry of each component is a critical variable. In this architecture, the PbTe cubes dictate the overall film morphology while the LaF3 fills interstitial space in-between the cubes, consistent with the predicted model. Energy dispersive X-ray spectroscopy confirms the dissimilar NC co-assembly is shown in Figure 5.6(c). After examining 450 PbTe cubes, it becomes clear that the majority of the cubes have at least one triangle assembled on each side. When three or four of the sides of a cube have triangles assembled on their edges, it is frequently observed that an additional triangle will assemble on at least one of the sides as well, which is the case 212 times out of 450. Importantly, for those counted, there were zero observed cubes without at least one triangle assembled next to it.

As stated earlier, the PbTe cubes dictate the overall film morphology when concen-
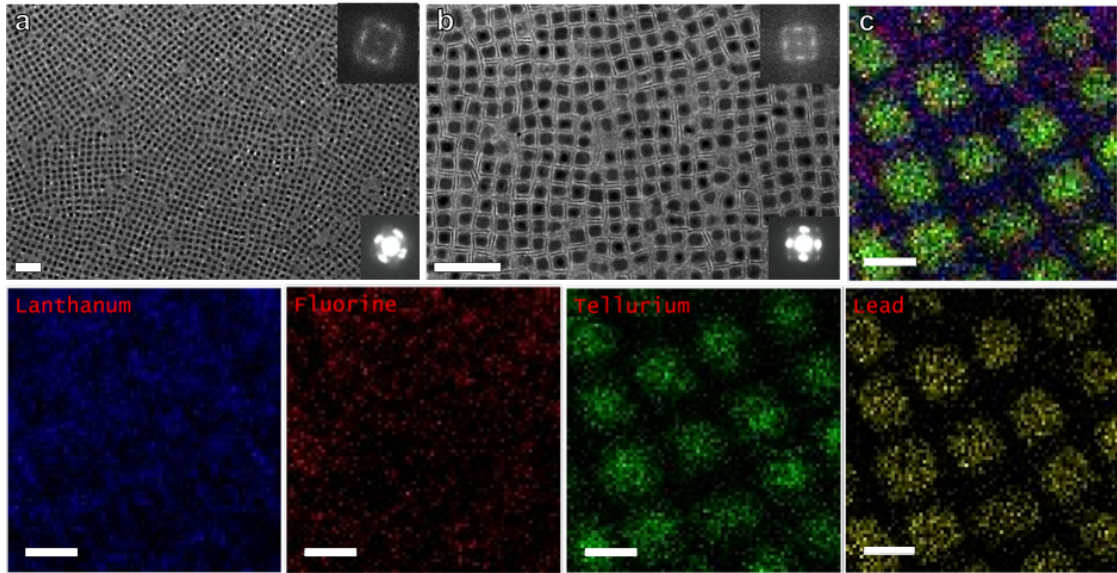
Figure 5.6: Co-assembly of PbTe and LaF$_3$ at various magnifications (a and b), scale bars are 100 nm with FFT insets in the upper right corners and small-angle SAED in the lower right corners. (c) EDS spectroscopy overlay, with each element listed, scale bars are 20 nm.

trations of the cubes are optimized for yielding a crystalline superlattice. However, it is also interesting to consider the case when there is a lower concentration of cubes, to fully investigate the impact of doping cubes into films that are overwhelmingly composed of triangles and to further test our model. As can be seen in Figure 5.7(b), in areas of a majority-cube superlattice where a grain boundary is present, or there is a gap between cubes in the film, the triangular plates can form strings, bridging the distance between the cubes. As the concentration of cubes decreases, shown in Figure 5.7(c, d), the cubes still cluster within a film of triangles, however in these cases again when there is a larger distance between cubes, the triangular plates form lamellar bridges. It is additionally observed that these lamellar strings can form without two cubes on either end, i.e. when there is only one cube on one side of the string, but these instances are significantly less common. Typically, these lamellar strings are composed of three or four plates, however longer strings are achievable as well, where a string of 13 plates is observed in Figure 5.7(c). In these exam-

ples, the cubes still assemble on top of a film of triangular plates, which due to the polycatenar ligand on their surfaces, assemble into architectures where one layer of triangular plates is offset from the layer on top of it, consistent with previous results [82]. The experimental results are compared to the predicted theory by plotting the data points onto the previously shown phase diagram, shown in Figure 5.7. Our theoretical model is in good agreement with the experimental results, particularly for the bullseye case for when the two NCs co-assemble successfully into a uniform lattice.
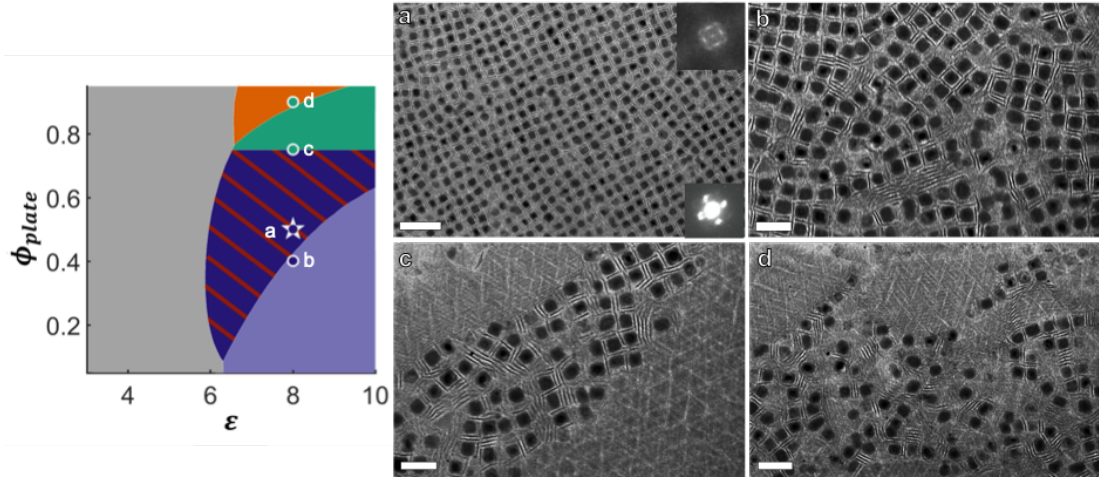
Figure 5.7: Comparison with the predicted phase diagram, where corresponding TEM images for a series of points are labeled within the diagram. (a) Represents the co-assembly with highest uniformity, a bullseye within the phase diagram, with FFT and small-angle SAED as insets in the upper and lower right corners. String morphologies in domains with fewer cubes than triangles can be clearly seen in panels (b-d) which match well with predicted phases. Scale bars are 100 nm for a and 50 nm for b-d.

Taking our developing design rules for co-assembly of anisotropic NCs and expanding them, combinations of two plate NCs were explored. In the previous example, assembly of the triangular plates is guided by the cubes due to the strong face-face interactions. The case for two two-dimensional materials is unique as the thickness of each edge is only 2 nm, which greatly reduces the area for NC-NC interactions when both plates assemble parallel to the substrate. Without a three-dimensional

material, neither NC should guide the assembly of the other, rather this type of co-assembly should be more similar to doping. Nevertheless, successful co-assembly of two anisotropic plate materials has been elusive, as differences in material composition, size, or shape lead to phase segregation.

GdF_3:Yb/Er (20/2 mol %) rhombic plates were chosen to combine with the previous LaF3 plates, as they have complementary shapes. These rhombic plates are 25.4 nm ($\pm$ 2.4 nm) by 23.6 nm ($\pm$1.9 nm) on their long and short sides, respectively. Similar to the previous study, initial attempts at co-assembly were unsuccessful with the native ligand, OA, on the surface of the NCs, as both of the plates phase segregate and exhibit mixed orientations with most subphase choices. Excess OA was added to the solutions, as the presence of extra free ligand in NC solutions has aided assembly in previous studies. However, phase segregation was still the dominant morphology of the obtained films. Again, to align the NCs and enhance co-assembly the polycatenar ligand was grafted to the surfaces of both the GdF_3 and LaF_3 and the resulting films are shown in Figure 5.8(a, b). In these films, both components are distributed throughout the assemblies. For the case where there are more LaF_3 triangular plates present, the crystallinity of their assembly is undisturbed by the presence of the GdF_3 plates. While the polycatenar ligand is large enough to shield some of the van der Waals forces between the NCs, clustering of similar NCs is still present in the films. Often groupings of two or three GdF_3 plates will assemble in the films, leading us to believe that there are still attractions between NCs of the same composition.

These groupings provide an opportunity for substitutional doping of one larger anisotropic NC for two smaller ones. In Figure 5.8(c, d), we show that the size of the LaF_3 triangular plates can be tuned such that two triangular plates better size-

match one rhombic plate. These smaller LaF$_3$ triangular plates have edge lengths of 14.9 $\pm$ 0.7 nm. Using this strategy, substitutional doping can be achieved for this system, where the film morphology is dictated by the rhombic plates, as highlighted by the FFT insets. Interestingly, the triangular plates can also fill in void space between grain boundaries within the film, as shown by Figure 5.8(d). This is the first example of substitutional doping with two anisotropic materials, a key step in advancing assembly choices of nanoscale building blocks.
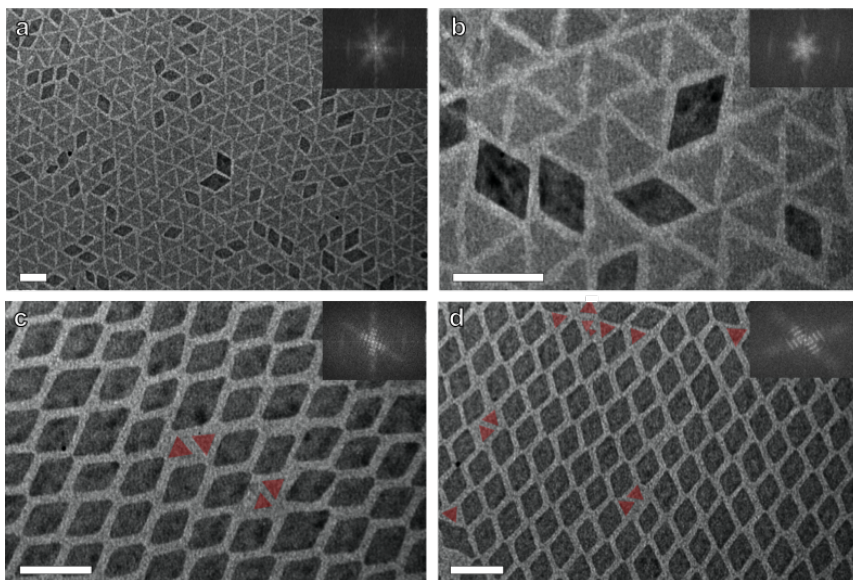
Figure 5.8: Co-assembly of GdF$_3$ rhombic plates with LaF$_3$ triangular plates: (a and b) with larger triangular plates where assembly can be dictated by the concentrations of each component, and (c and d) where smaller triangular plates are used in assembly for substitutional doping into film morphologies of the rhombic plates. FFTs are upper right insets, scale bars are 50 nm. False coloring has been added to c and d to highlight the doping.

5.5   Conclusions

In summary, we have employed a theory and simulation driven, inverse design approach for the selection of experimental design handles - stoichiometry, ligand type, and temperature - to drive the co-assembly of nanocubes and triangular nanoplates with strong phase segregation tendencies. We show that our theoretically predicted phase diagram can be employed to guide computational and experimental selections

of parameters across a large phase space to specifically target the co-assembly region of interest, with good agreement across theory, simulations, and experiments, as shown in Figures 5.3 and 5.7. Dissecting the underlying driving forces contributing to co-assembly reveals why the polycatenar ligand can enhance both lattice yield and stability and extension of this design principle to another system produced a similar success in co-assembly behaviors. These results suggest that co-assembly of binary systems can be achieved via the usage of ligand shells as a handle for tuning the relative degree of attraction/repulsion between particles. Specifically, enhancements in attraction is achieved through selecting for ligand shells exhibiting emergent lock-and-key interaction motifs that prevents phase segregations that commonly plague previous attempts at non-complementary shape co-assembly. This theory-guided design strategy opens a potential path forward for the inverse design of the co-crystallization of other binary shape systems that can vary the stoichiometry of each component, a large step towards precisely designed metamaterials.

CHAPTER VI

Conclusions and Outlook

6.1 Summary of Results

In summary, we have demonstrated that nanomaterial assembly is a complex process which is complicated by many interacting anisotropy axes which include nanoparticle core shape, patchy decoration and ligand bulkiness. Each study in this dissertation showed an example of a specific material system where fundamental understanding of particle attributes allowed for the development of design principles to guide the assembly into a desired final morphology. These design principles have implications for the inverse design process where they could be used to target and design materials with complex crystalline order.

In the first study (Ch. 2), we demonstrated that densely packed polyhedra can be used as a way of obtaining topologically ordered structures that are stabilized by the contacts formed in the densest packing structure, and that this behavior is useful in stabilizing structures against thermal fluctuation. This work showed that this phenomena is generalizable to densely packed structures where their topology can be characterized in a similar fashion (such as edge, face and vertex contacts in the densest packing). Finally, given that such complex shapes can indeed be synthesized experimentally, our work provides a roadmap for how such shapes could be used

to create structures with topological order that is stable in the presence of thermal fluctuations.

In the second study (Ch. 3), we showed that patchy polygons make up a very large and complex materials space, where there exist many unique ways to pattern their edges with attractive ligands. We developed rules to show how binary pairs of these polygons can be used to access different types of morphologies including terminating structures, fibers, lattices and rings. These rules can be used separately or in combination to develop open, low-coordination structures which are known to possess photonic and other novel material properties via hierarchical self-assembly approaches. Additionally, we showed that structures with tunable pore size are possible by utilizing a rule for lattice formation and controlling the number of patches on both particles. The experimental approach for the process described in this work is ongoing, as fabrication of particles with patches on targeted edges is a new and challenging problem.

In the third study (Ch. 4), we showed that ligands of varying bulkiness partition themselves on anisotropic nanoparticles to locations of high curvature in order to increase their entropy. We demonstrated a scaling theory, which allowed for the prediction of ligand partitioning on anisotropic shapes, where the ligands can have different bulkiness. We then showed that simulations of nanoplates with such ligand distribution mirror the experimental results, and that ligand bulkiness plays a role in how nanoplates stack layer-by-layer.

In the fourth study (Ch. 5), we used what we learned about ligand partitioning from the previous work and we undertook an inverse design approach to assemble nanocubes and triangular nanoplates. In this work, the goal was to create an ordered co-assembly of these two species which normally phase separate when there are no

ligands attached to them. To do this, we exploited the knowledge of ligand parti-
tioning to develop phase diagrams of stoichiometry and temperature, and were able
to determine that longer ligands improved the co-assembly conditions by expanding
the range of stoichiometry and temperatures where co-assembly was possible. Fi-
nally, upon using simulations to verify the calculated phase diagram, we provided
stoichiometric values and temperatures to our experimental collaborator who was
able to successfully achieve the ordered co-assembly.

6.2   Concluding Remarks

Design principles have been used in previous works to understand the complicated
multi-dimensional design phase space inherent in anisotropic self-assembly. This
dissertation sought to expand upon those principles in order to target very specific
materials, from dense topological packings to interfacial tilings of unary and binary
systems of anisotropic particles. One can take these sets of design principles and now
consider how they might interplay with each other, such as we showed in Chapters
4 and 5, where ligand architecture is shown to play a role in both unary and binary
systems. Such overlaying of design rules gives us strong leverage over the design space
of both hard and patchy particles and could be utilized in inverse design approaches
to assemble exotic structures whose constituent nanoparticle attributes cannot be
predicted from simple observation.

BIBLIOGRAPHY

BIBLIOGRAPHY

[1] Sharon C. Glotzer and Michael J. Solomon. Anisotropy of building blocks and their assembly into complex structures. *Nature Materials*, 6(8):557562, Aug 2007.

[2] Elizabeth R. Chen, Daphne Klotsa, Michael Engel, Pablo F. Damasceno, and Sharon C. Glotzer. Complexity in surfaces of densest packings for families of polyhedra. *Phys. Rev. X*, 4:011024, Feb 2014.

[3] Greg van Anders, Daphne Klotsa, Andrew S. Karas, Paul M. Dodd, and Sharon C. Glotzer. Digital Alchemy for Materials Design: Colloids and Beyond. *ACS Nano*, 9:9542–9553, 2015.

[4] Fan Li, David P. Josephson, and Andreas Stein. Colloidal assembly: the road from particles to colloidal molecules and crystals. *Angewandte Chemie*, 50(2):360–388, Jan 2011.

[5] Joel Henzie, Michael Grünwald, Asaph Widmer-Cooper, Phillip L. Geissler, and Peidong Yang. Self-assembly of uniform polyhedral silver nanocrystals into densest packings and exotic superlattices. *Nat. Mater.*, 11:131–137, 2012.

[6] Ching-Wen Liao, Yeh-Sheng Lin, Kaushik Chanda, Yen-Fang Song, and Michael H. Huang. Formation of diverse supercrystals from self-assembly of a variety of polyhedral gold nanocrystals. *Journal of the American Chemical Society*, 135(7):2684–2693, 2013.

[7] Younan Xia, Yujie Xiong, Byungkwon Lim, and Sara E. Skrabalak. Shape-controlled synthesis of metal nanocrystals: Simple chemistry meets complex physics? *Angew. Chem., Int. Ed.*, 48(1):60–103, 2009.

[8] Andrea Tao, Prasert Sinsermsuksakul, and Peidong Yang. Tunable plasmonic lattices of silver nanocrystals. *Nat. Nanotechnol.*, 2:435–440, 2007.

[9] Daan Frenkel. Entropy-driven phase transitions. *Physica A: Statistical Mechanics and its Applications*, 263(1-4):26–38, Feb 1999.

[10] Greg van Anders, Daphne Klotsa, N. Khalid Ahmed, Michael Engel, and Sharon C. Glotzer. Understanding shape entropy through local dense packing. *Proc. Natl. Acad. Sci. U.S.A.*, 111:E4812–E4821, 2014.

[11] Rose K. Cersonsky, Greg van Anders, Paul M. Dodd, and Sharon C. Glotzer. Relevance of packing to colloidal self-assembly. *Proceedings of the National Academy of Sciences of the United States of America*, 115(7):1439–1444, Feb 2018.

[12] Zhenli Zhang and Sharon C. Glotzer. Self-assembly of patchy particles. *Nano Letters*, 4(8):1407–1413, Aug 2004.

[13] Greg van Anders, N. Khalid Ahmed, Ross Smith, Michael Engel, and Sharon C. Glotzer. Entropically patchy particles: Engineering valence through shape entropy. *ACS Nano*, 8:931–940, 2014.

[14] Aleks Reinhardt and Daan Frenkel. DNA brick self-assembly with an off-lattice potential. *Soft matter*, 12(29):6253–6260, Jul 2016.

[15] Aleks Reinhardt, John S. Schreck, Flavio Romano, and Jonathan P. K. Doye. Self-assembly of two-dimensional binary quasicrystals: a possible route to a DNA quasicrystal. *Journal of Physics. Condensed Matter*, 29(1):014006, Jan 2017.

[16] Rachelle M Choueiri, Elizabeth Galati, Héloïse Thérien-Aubin, Anna Klinkova, Egor M. Larin, Ana Querejeta-Fernández, Lili Han, Huolin L. Xin, Oleg Gang, Ekaterina B. Zhulina, Michael Rubinstein, and Eugenia Kumacheva. Surface patterning of nanoparticles with polymer patches. *Nature*, 538(7623):79–83, Oct 2016.

[17] Elizabeth Galati, Moritz Tebbe, Ana Querejeta-Fernández, Huolin L. Xin, Oleg Gang, Ekaterina B. Zhulina, and Eugenia Kumacheva. Shape-specific patterning of polymer-functionalized nanoparticles. *ACS Nano*, 11(5):4995–5002, May 2017.

[18] Jianyuan Zhang, Peter J. Santos, Paul A. Gabrys, Sangho Lee, Caroline Liu, and Robert J. Macfarlane. Self-assembling nanocomposite tectons. *Journal of the American Chemical Society*, 138(50):16228–16231, Dec 2016.

[19] Zhenli Zhang, Aaron S. Keys, Ting Chen, and Sharon C. Glotzer. Self-assembly of patchy particles into diamond structures through molecular mimicry. *Langmuir: the ACS Journal of Surfaces and Colloids*, 21(25):11547–11551, Dec 2005.

[20] C. Casagrande, P. Fabre, E. Raphaël, and M. Veyssié. Janus beads: Realization and behaviour at water/oil interfaces. *Europhysics Letters (EPL)*, 9(3):251–255, Jun 1989.

[21] Xingchen Ye, Jun Chen, Michael Engel, Jaime A. Millan, Wenbin Li, Liang Qi, Guozhong Xing, Joshua E. Collins, Cherie R. Kagan, Ju Li, Sharon C Glotzer, and Christopher B. Murray. Competition of shape and interaction patchiness for self-assembling nanoplates. *Nature Chemistry*, 5(6):466–473, Jun 2013.

[22] Jaime A. Millan, Daniel Ortiz, Greg van Anders, and Sharon C. Glotzer. Self-assembly of archimedean tilings with enthalpically and entropically patchy polygons. *ACS Nano*, 8(3):2918–2928, Mar 2014.

[23] Susanne Wagner and Gerhard Kahl. Structure and equation-of-state of a disordered system of shape anisotropic patchy particles. *Molecular physics*, pages 1–8, Mar 2019.

[24] E. G. J. Wijnhoven and W. L. Vos. Preparation of photonic crystals made of air spheres in titania. *Science*, 281(5378):802–804, Aug 1998.

[25] Qiang Gao, Xing Li, Guo-Hong Ning, Hai-Sen Xu, Cuibo Liu, Bingbing Tian, Wei Tang, and Kian Ping Loh. Covalent organic framework with frustrated bonding network for enhanced carbon dioxide storage. *Chemistry of Materials*, 30(5):1762–1768, Mar 2018.

[26] S. M. Kuznicki, V. A. Bell, S. Nair, H. W. Hillhouse, R. M. Jacubinas, C. M. Braunbarth, B. H. Toby, and M. Tsapatsis. A titanosilicate molecular sieve with adjustable pores for size-selective adsorption of molecules. *Nature*, 412(6848):720–724, Aug 2001.

[27] Wenxiang Zhang, Liming Zhang, Haifeng Zhao, Bin Li, and Heping Ma. A two-dimensional cationic covalent organic framework membrane for selective molecular sieving. *Journal of Materials Chemistry A*, 2018.

[28] Pablo F. Damasceno, Michael Engel, and Sharon C. Glotzer. Predictive self-assembly of polyhedra into complex structures. *Science*, 337(6093):453457, Jul 2012.

[29] Daphne Klotsa, Elizabeth R. Chen, Michael Engel, and Sharon C. Glotzer. Intermediate crystalline structures of colloids in shape space. *Soft matter*, 14(43):8692–8697, 2018.

[30] Robert J. Macfarlane, Byeongdu Lee, Matthew R. Jones, Nadine Harris, George C. Schatz, and Chad A. Mirkin. Nanoparticle superlattice engineering with DNA. *Science*, 334(6053):204–208, Oct 2011.

[31] William Zygmunt, Erin G. Teich, Greg van Anders, and Sharon C. Glotzer. Topological order in densely packed anisotropic colloids. *Physical Review E*, 100(3):032608, Sep 2019.

[32] Eric Dennis, Alexei Kitaev, Andrew Landahl, and John Preskill. Topological quantum memory. *J. Math. Phys.*, 43(9):4452–4505, 2002.

[33] Daan Frenkel. Order through entropy. *Nat. Mater.*, 14:9–12, 2015.

[34] Yugang Zhang, Fang Lu, Daniel van der Lelie, and Oleg Gang. Continuous phase transformation in nanocube assemblies. *Phys. Rev. Lett.*, 107:135701, Sep 2011.

[35] Oleg Gang and Yugang Zhang. Shaping phases by phasing shapes. *ACS Nano*, 5(11):8459–8465, 2011.

[36] Yi Peng, Feng Wang, Ziren Wang, Ahmed M. Alsayed, Zexin Zhang, Arjun G. Yodh, and Yilong Han. Two-step nucleation mechanism in solid–solid phase transitions. *Nat Mater*, 14:101–108, 2015.

[37] Chrisy Xiyu Du, Greg van Anders, Richmond S. Newman, and Sharon C. Glotzer. Shape-driven colloidal crystal–crystal transitions. *Proc. Natl. Acad. Sci. U.S.A.*, 114:E3892–E3899, 2017.

[38] C. L. Kane and T. C. Lubensky. Topological boundary modes in isostatic lattices. *Nature Physics*, 10(1):39–45, 2014.

[39] Johannes Loehr, Michael Loenne, Adrian Ernst, Daniel de Las Heras, and Thomas M. Fischer. Topological protection of multiparticle dissipative transport. *Nature Communications*, 7:11745, Jun 2016.

[40] Johannes Loehr, Daniel de las Heras, Adam Jarosz, Maciej Urbaniak, Feliks Stobiecki, Andreea Tomita, Rico Huhnstock, Iris Koch, Arno Ehresmann, Dennis Holzinger, and Thomas M. Fischer. Colloidal topological insulators. *Communications Physics*, 1(1):4, Dec 2018.

[41] Emil Prodan and Camelia Prodan. Topological phonon modes and their role in dynamic instability of microtubules. *Physical Review Letters*, 103(24):248101, Dec 2009.

[42] S. Hossein Mousavi, Alexander B. Khanikaev, and Zheng Wang. Topologically protected elastic waves in phononic metamaterials. *Nature Communications*, 6:8682, Nov 2015.

[43] Pai Wang, Ling Lu, and Katia Bertoldi. Topological phononic crystals with one-way elastic edge waves. *Physical Review Letters*, 115(10):104302, Sep 2015.

[44] Cheng He, Xu Ni, Hao Ge, Xiao-Chen Sun, Yan-Bin Chen, Ming-Hui Lu, Xiao-Ping Liu, and Yan-Feng Chen. Acoustic topological insulator and robust one-way sound transport. *Nature physics*, 12(12):1124–1129, Aug 2016.

[45] Emil Prodan, Kyle Dobiszewski, Alokik Kanwal, John Palmieri, and Camelia Prodan. Dynamical majorana edge modes in a broad class of topological mechanical systems. *Nature Communications*, 8:14587, Feb 2017.

[46] Jin-Wu Jiang and Harold S. Park. Strain tunable phononic topological bandgaps in two-dimensional hexagonal boron nitride. *Journal of applied physics*, 125(8):082511, Feb 2019.

[47] Ling Lu, John D. Joannopoulos, and Marin Soljačić. Topological photonics. *Nature photonics*, 8(11):821–829, Nov 2014.

[48] Joshua A. Anderson, M. Eric Irrgang, and Sharon C. Glotzer. Scalable metropolis monte carlo for simulation of hard shapes. *Computer Physics Communications*, 204:21–30, Jul 2016.

[49] Joshua A. Anderson and Sharon C. Glotzer. The Development and Expansion of HOOMD-Blue Through Six Years of GPU Proliferation. 2013.

[50] Jens Glaser, Trung Dac Nguyen, Joshua A. Anderson, Pak Lui, Filippo Spiga, Jaime A. Millan, David C. Morse, and Sharon C. Glotzer. Strong scaling of general-purpose molecular dynamics simulations on GPUs. *Comput. Phys. Commun.*, 192:97–107, 2015.

[51] Michael Engel, Joshua A. Anderson, Sharon C. Glotzer, Masaharu Isobe, Etienne P. Bernard, and Werner Krauth. Hard-disk equation of state: First-order liquid-hexatic transition in two dimensions with three simulation methods. *Phys. Rev. E*, 87:042134, Apr 2013.

[52] Daan Frenkel. New monte carlo method to compute the free energy of arbitrary solids. application to the fcc and hcp phases of hard spheres. *J. Chem. Phys.*, 81(7):3188–3193, 1984.

[53] Amir Haji-Akbari, Michael Engel, and Sharon C. Glotzer. Phase diagram of hard tetrahedra. *J. Chem. Phys.*, 135(19):194101, 2011.

[54] Alexei Kitaev and John Preskill. Topological entanglement entropy. *Phys. Rev. Lett.*, 96:110404, Mar 2006.

[55] Joost de Graaf, René van Roij, and Marjolein Dijkstra. Dense regular packings of irregular nonconvex particles. *Phys. Rev. Lett.*, 107:155501, Oct 2011.

[56] Umang Agarwal and Fernando A. Escobedo. Mesophase behaviour of polyhedral particles. *Nature Materials*, 10(3):230–235, Mar 2011.

[57] Ran Ni, Anjan Prasad Gantapara, Joost de Graaf, Rene van Roij, and Marjolein Dijkstra. Phase diagram of colloidal hard superballs: from cubes via spheres to octahedra. *Soft Matter*, 8:8826–8834, 2012.

[58] Pablo F. Damasceno, Michael Engel, and Sharon C. Glotzer. Crystalline Assemblies and Densest Packings of a Family of Truncated Tetrahedra and the Role of Directional Entropic Forces. *ACS Nano*, 6(1):609–614, 2012.

[59] Anjan P. Gantapara, Joost de Graaf, René van Roij, and Marjolein Dijkstra. Phase diagram and structural diversity of a family of truncated cubes: Degenerate close-packed structures and vacancy-rich states. *Phys. Rev. Lett.*, 111:015501, Jul 2013.

[60] Curt Waltmann, Nathan Horst, and Alex Travesset. Capping Ligand Vortices as "atomic Orbitals" in Nanocrystal Self-Assembly. *ACS Nano*, 11(11):11273–11282, 2017.

[61] Tommy Waltmann, Curt Waltmann, Nathan Horst, and Alex Travesset. Many Body Effects and Icosahedral Order in Superlattice Self-Assembly. *Journal of the American Chemical Society*, 140(26):8236–8245, 2018.

[62] Michael H. Huang and Po-Heng Lin. Shape-controlled synthesis of polyhedral nanocrystals and their facet-dependent properties. *Advanced Functional Materials*, 22(1):14–24, 2012.

[63] Michael Taylor, Luca Francesconi, Miklós Gerendás, Ali Shanian, Carl Carson, and Katia Bertoldi. Low porosity metallic periodic structures with negative poisson's ratio. *Advanced Materials*, 26(15):2365–2370, Apr 2014.

[64] Viet Hung Ho, Duc Tam Ho, Soon-Yong Kwon, and Sung Youb Kim. Negative poisson's ratio in periodic porous graphene structures. *physica status solidi (b)*, 253(7):1303–1309, Jul 2016.

[65] Connor R. Bilchak, Eileen Buenning, Makoto Asai, Kai Zhang, Christopher J. Durning, Sanat K. Kumar, Yucheng Huang, Brian C. Benicewicz, David W. Gidley, Shiwang Cheng, Alexei P. Sokolov, Matteo Minelli, and Ferruccio Doghieri. Polymer-grafted nanoparticle membranes with controllable free volume. *Macromolecules*, 50(18):7111–7120, Sep 2017.

[66] Wojciech Rżysko, Damian Nieckarz, and Paweł Szabelski. Modeling of the 2D self-assembly of tripod-shaped functional molecules with patchy interaction centers. *Adsorption*, 25(1):75–85, Jan 2019.

[67] Tiara Ann Maula, Harold Hatch, Vincent K. Shen, Srinivas Rangarajan, and Jeetain Mittal. Designing molecular building blocks for the self- assembly of complex porous networks. *Mol. Syst. Des. Eng.*, 2019.

[68] Nikoletta Pakalidou, Junju Mu, Andrew J Masters, and Carlos Avendano. Engineering porous two-dimensional lattices via self- assembly of non-convex hexagonal platelets. *Mol. Syst. Des. Eng.*, 2019.

[69] Zhan-Wei Li, Yu-Wei Sun, Yan-Hui Wang, You-Liang Zhu, Zhong-Yuan Lu, and Zhao-Yan Sun. Kinetics-controlled design principles for two-dimensional open lattices using atom-mimicking patchy particles. *Nanoscale*, 12(7):4544–4551, Feb 2020.

[70] Carina Karner, Christoph Dellago, and Emanuela Bianchi. Design of patchy rhombi: From close-packed tilings to open lattices. *Nano Letters*, 19(11):7806–7815, Nov 2019.

[71] Carina Karner, Christoph Dellago, and Emanuela Bianchi. Hierarchical self-assembly of patchy colloidal platelets. *Soft matter*, 16(11):2774–2785, Mar 2020.

[72] Y Sun and Y Xia. Triangular nanoplates of silver: synthesis, characterization, and use as sacrificial templates for generating triangular nanorings of gold. *Advanced Materials*, 15(9):695699, May 2003.

[73] Yujie Xiong, Joseph M. McLellan, Jingyi Chen, Yadong Yin, Zhi-Yuan Li, and Younan Xia. Kinetically controlled synthesis of triangular and hexagonal nanoplates of palladium and their SPR/SERS properties. *Journal of the American Chemical Society*, 127(48):17118–17127, Dec 2005.

[74] Elena V. Shevchenko, Dmitri V. Talapin, Nicholas A. Kotov, Stephen O'Brien, and Christopher B. Murray. Structural diversity in binary nanoparticle superlattices. *Nature*, 439(7072):55–59, Jan 2006.

[75] Leonard R. MacGillivray. Design rules: a net and archimedean polyhedra score big for self-assembly. *Angewandte Chemie*, 51(5):1110–1112, Jan 2012.

[76] Robert J. Macfarlane, Byeongdu Lee, Matthew R. Jones, Nadine Harris, George C. Schatz, and Chad A. Mirkin. Nanoparticle superlattice engineering with dna. *Science*, 334(6053):204208, Oct 2011.

[77] Daniel Morphew, James Shaw, Christopher Avins, and Dwaipayan Chakrabarti. Programming hierarchical self-assembly of patchy particles into colloidal crystals via colloidal molecules. *ACS Nano*, 12(3):2355–2364, Mar 2018.

[78] Lucia Baldauf, Erin G. Teich, Greg van Anders, Peter Schall, and Laura Rossi. Shape and interaction decoupling for colloidal pre-assembly, 2019.

[79] Aaron Santos, Jaime Andres Millan, and Sharon C. Glotzer. Facetted patchy particles through entropy-driven patterning of mixed ligand SAMS. *Nanoscale*, 4(8):2640–2650, Apr 2012.

[80] Matthew N. O'Brien, Martin Girard, Hai-Xin Lin, Jaime A. Millan, Monica Olvera de la Cruz, Byeongdu Lee, and Chad A. Mirkin. Exploring the zone of anisotropy and broken symmetries in DNA-mediated nanoparticle crystallization. *Proceedings of the National Academy of Sciences of the United States of America*, 113(38):10485–10490, Sep 2016.

[81] Fang Lu, Thi Vo, Yugang Zhang, Alex Frenkel, Kevin G. Yager, Sanat Kumar, and Oleg Gang. Unusual packing of soft-shelled nanocubes. *Sci. Adv.*, 5(5):eaaw2399, May 2019.

[82] Katherine C. Elbert, Thi Vo, Nadia M. Krook, William Zygmunt, Jungmi Park, Kevin G. Yager, Russell J. Composto, Sharon C. Glotzer, and Christopher B. Murray. Dendrimer ligand directed nanoplate assembly. *ACS Nano*, 13(12):14241–14251, Dec 2019.

[83] Joshua A. Anderson, Jens Glaser, and Sharon C. Glotzer. HOOMD-blue: A python package for high-performance molecular dynamics and hard particle monte carlo simulations. *Computational Materials Science*, page 109363, Nov 2019.

[84] Jiwen Liu and Erik Luijten. Rejection-free geometric cluster algorithm for complex fluids. *Physical Review Letters*, 92(3):035504, Jan 2004.

[85] Daniel W. Sinkovits, Stephen A. Barr, and Erik Luijten. Rejection-free monte carlo scheme for anisotropic particles. *The Journal of Chemical Physics*, 136(14):144111, Apr 2012.

[86] Vyas Ramasubramani, Bradley D. Dice, Eric S. Harper, Matthew P. Spellings, Joshua A. Anderson, and Sharon C. Glotzer. freud: A software suite for high throughput analysis of particle simulation data, 2019.

[87] Solomon W. Golomb. *Polyominoes: puzzles, patterns, problems, and packings*, volume 16. Princeton University Press, 1996.

[88] Sung-Min Kang, Chang-Hyung Choi, Jongmin Kim, Su-Jin Yeom, Daeyeon Lee, Bum Jun Park, and Chang-Soo Lee. Capillarity-induced directed self-assembly of patchy hexagram particles at the air-water interface. *Soft matter*, 12(27):5847–5853, Jul 2016.

[89] André H. Gröschel, Felix H. Schacher, Holger Schmalz, Oleg V Borisov, Ekaterina B. Zhulina, Andreas Walther, and Axel H. E. Müller. Precise hierarchical self-assembly of multicompartment micelles. *Nature Communications*, 3:710, Feb 2012.

[90] Y. Limon Duparcmeur, A. Gervois, and J. P. Troadec. Dense periodic packings of regular polygons. *Journal de Physique I*, 5(12):1539–1550, 1995.

[91] Ting I. N. G. Li, Rastko Sknepnek, Robert J Macfarlane, Chad A Mirkin, and Monica Olvera de la Cruz. Modeling the crystallization of spherical nucleic acid nanoparticle conjugates with molecular dynamics simulations. *Nano Letters*, 12(5):2509–2514, May 2012.

[92] Thi Vo, Venkat Venkatasubramanian, Sanat Kumar, Babji Srinivasan, Suchetan Pal, Yugang Zhang, and Oleg Gang. Stoichiometric control of DNA-grafted colloid self-assembly. *Proceedings of the National Academy of Sciences of the United States of America*, 112(16):4982–4987, Apr 2015.

[93] Qianqian Shi, Kae Jye Si, Debabrata Sikdar, Lim Wei Yap, Malin Premaratne, and Wenlong Cheng. Two-dimensional bipyramid plasmonic nanoparticle liquid crystalline superstructure with four distinct orientational packing orders. *ACS Nano*, 10(1):967–976, Jan 2016.

[94] Michael A. Boles, Michael Engel, and Dmitri V. Talapin. Self-assembly of colloidal nanocrystals: From intricate structures to functional materials. *Chemical Reviews*, 116(18):11220–11289, Sep 2016.

[95] Xingchen Ye, Joshua E. Collins, Yijin Kang, Jun Chen, Daniel T. N. Chen, Arjun G. Yodh, and Christopher B. Murray. Morphologically controlled synthesis of colloidal upconversion nanophosphors and their shape-directed self-assembly. *Proceedings of the National Academy of Sciences of the United States of America*, 107(52):22430–22435, Dec 2010.

[96] Gurvinder Singh, Henry Chan, Artem Baskin, Elijah Gelman, Nikita Repnin, Petr Král, and Rafal Klajn. Self-assembly of magnetite nanocubes into helical superstructures. *Science*, 345(6201):1149–1153, Sep 2014.

[97] Sabrina Disch, Erik Wetterskog, Raphaël P Hermann, Denis Korolkov, Peter Busch, Peter Boesecke, Olivier Lyon, Ulla Vainio, German Salazar-Alvarez, Lennart Bergström, and Thomas Brückel. Structural diversity in iron oxide nanoparticle assemblies as directed by particle morphology and orientation. *Nanoscale*, 5(9):3969–3975, May 2013.

[98] Fang Lu, Kevin G. Yager, Yugang Zhang, Huolin Xin, and Oleg Gang. Superlattices assembled through shape-induced directional binding. *Nature Communications*, 6:6912, Apr 2015.

[99] Ruipeng Li, Kaifu Bian, Tobias Hanrath, William A. Bassett, and Zhongwu Wang. Decoding the superlattice and interface structure of truncate PbS nanocrystal-assembled supercrystal and associated interaction forces. *Journal of the American Chemical Society*, 136(34):12047–12055, Aug 2014.

[100] Yuping Wang, Peter J. Santos, Joshua M Kubiak, Xinheng Guo, Margaret S. Lee, and Robert J. Macfarlane. Multistimuli responsive nanocomposite tectons for pathway dependent self-assembly and acceleration of covalent bond formation. *Journal of the American Chemical Society*, 141(33):13234–13243, Aug 2019.

[101] Taejong Paik, Dong-Kyun Ko, Thomas R. Gordon, Vicky Doan-Nguyen, and Christopher B. Murray. Studies of liquid crystalline self-assembly of GdF nanoplates by in-plane, out-of-plane SAXS. *ACS Nano*, 5(10):8322–8330, Oct 2011.

[102] Benjamin T. Diroll, Katie M. Weigandt, Davit Jishkariani, Matteo Cargnello, Ryan J. Murphy, Lawrence A. Hough, Christopher B. Murray, and Bertrand Donnio. Quantifying "softness" of organic coatings on gold nanoparticles using correlated small-angle x-ray and neutron scattering. *Nano Letters*, 15(12):8008–8012, Dec 2015.

[103] Jessy L. Baker, Asaph Widmer-Cooper, Michael F. Toney, Phillip L. Geissler, and A. Paul Alivisatos. Device-scale perpendicular alignment of colloidal nanorods. *Nano Letters*, 10(1):195–201, Jan 2010.

[104] Yixuan Yu, Dian Yu, and Christine A. Orme. Reversible, tunable, electric-field driven assembly of silver nanocrystal superlattices. *Nano Letters*, 17(6):3862–3869, Jun 2017.

[105] Ajay Singh, Niall J. English, and Kevin M. Ryan. Highly ordered nanorod assemblies extending over device scale areas and in controlled multilayers by electrophoretic deposition. *The Journal of Physical Chemistry. B*, 117(6):1608–1615, Feb 2013.

[106] Michael A. Boles and Dmitri V. Talapin. Self-assembly of tetrahedral CdSe nanocrystals: effective "patchiness" via anisotropic steric interaction. *Journal of the American Chemical Society*, 136(16):5868–5871, Apr 2014.

[107] Xingchen Ye, Chenhui Zhu, Peter Ercius, Shilpa N Raja, Bo He, Matthew R. Jones, Matthew R Hauwiller, Yi Liu, Ting Xu, and A. Paul Alivisatos. Structural diversity in binary superlattices self-assembled from polymer-grafted nanocrystals. *Nature Communications*, 6:10052, Dec 2015.

[108] Andrea Castelli, Joost de Graaf, Sergio Marras, Rosaria Brescia, Luca Goldoni, Liberato Manna, and Milena P. Arciniegas. Understanding and tailoring ligand interactions in the self-assembly of branched colloidal nanocrystals into planar superlattices. *Nature Communications*, 9(1):1141, Mar 2018.

[109] Artsiom Antanovich, Anatol Prudnikau, Anna Matsukovich, Alexander Achtstein, and Mikhail Artemyev. Self-assembly of CdSe nanoplatelets into stacks of controlled size induced by ligand exchange. *The Journal of Physical Chemistry C*, 120(10):5764–5775, Mar 2016.

[110] Wei Zhou, Meng Yao, Lin Guo, Yueming Li, Jinghong Li, and Shihe Yang. Hydrazine-linked convergent self-assembly of sophisticated concave polyhedrons of beta-ni(OH)(2) and NiO from nanoplate building blocks. *Journal of the American Chemical Society*, 131(8):2959–2964, Mar 2009.

[111] Ju Wu, Fang Duan, Yan Zheng, and Yi Xie. Synthesis of bi2 WO6 nanoplate-built hierarchical nest-like structures with visible-light-induced photocatalytic activity. *The Journal of Physical Chemistry C*, 111(34):12866–12871, Aug 2007.

[112] Xingchen Ye, Jun Chen, M. Eric Irrgang, Michael Engel, Angang Dong, Sharon C. Glotzer, and Christopher B. Murray. Quasicrystalline nanocrystal superlattice with partial matching rules. *Nature Materials*, 16(2):214–219, 2017.

[113] M. S. Wertheim. Fluids with highly directional attractive forces. i. statistical thermodynamics. *Journal of statistical physics*, 35(1-2):19–34, Apr 1984.

[114] M. S. Wertheim. Fluids with highly directional attractive forces. II. thermodynamic perturbation theory and integral equations. *Journal of statistical physics*, 35(1-2):35–47, Apr 1984.

[115] M. S. Wertheim. Fluids with highly directional attractive forces. III. multiple attraction sites. *Journal of statistical physics*, 42(3-4):459–476, Feb 1986.

[116] M. S. Wertheim. Fluids with highly directional attractive forces. IV. equilibrium polymerization. *Journal of statistical physics*, 42(3-4):477–492, Feb 1986.

[117] Katherine C. Elbert, Davit Jishkariani, Yaoting Wu, Jennifer D. Lee, Bertrand Donnio, and Christopher B. Murray. Design, self-assembly, and switchable wettability in hydrophobic, hydrophilic, and janus dendritic ligandgold nanoparticle hybrid materials. *Chemistry of Materials*, 29(20):8737–8746, Oct 2017.

[118] Davit Jishkariani, Katherine C. Elbert, Yaoting Wu, Jennifer D Lee, Michiel Hermes, Da Wang, Alfons van Blaaderen, and Christopher B. Murray. Nanocrystal core size and shape substitutional doping and underlying crystalline order in nanocrystal superlattices. *ACS Nano*, 13(5):5712–5719, May 2019.

[119] Katherine C. Elbert, Jennifer D. Lee, Yaoting Wu, and Christopher B. Murray. Improved chemical and colloidal stability of gold nanoparticles through dendron capping. *Langmuir: the ACS Journal of Surfaces and Colloids*, 34(44):13333–13338, Nov 2018.

[120] Nadia M. Krook, Jamie Ford, Manuel Marchal, Patrice Rannou, Jeffrey S. Meth, Christopher B. Murray, and Russell J. Composto. Alignment of nanoplates in lamellar diblock copolymer domains and the effect of particle volume fraction on phase behavior. *ACS macro letters*, 7(12):1400–1407, Dec 2018.

[121] Rhiannon K. Iha, Karen L. Wooley, Andreas M. Nyström, Daniel J. Burke, Matthew J. Kade, and Craig J. Hawker. Applications of orthogonal "click" chemistries in the synthesis of functional soft materials. *Chemical Reviews*, 109(11):5620–5686, Nov 2009.

[122] Taejong Paik, Ann-Marie Chacko, John L. Mikitsh, Joseph S. Friedberg, Daniel A. Pryma, and Christopher B. Murray. Shape-controlled synthesis of isotopic yttrium-90-labeled rare earth fluoride nanocrystals for multimodal imaging. *ACS Nano*, 9(9):8718–8728, Sep 2015.

[123] Angang Dong, Xingchen Ye, Jun Chen, Yijin Kang, Thomas Gordon, James M. Kikkawa, and Christopher B. Murray. A generalized ligand-exchange strategy enabling sequential surface functionalization of colloidal nanocrystals. *Journal of the American Chemical Society*, 133(4):998–1006, Feb 2011.

[124] Angang Dong, Jun Chen, Patrick M. Vora, James M. Kikkawa, and Christopher B. Murray. Binary nanocrystal superlattice membranes self-assembled at the liquid-air interface. *Nature*, 466(7305):474–477, Jul 2010.

[125] Igor Coropceanu, Michael A. Boles, and Dmitri V. Talapin. Systematic mapping of binary nanocrystal superlattices: the role of topology in phase selection. *Journal of the American Chemical Society*, 141(14):5728–5740, Apr 2019.

[126] M. Daoud and J. P. Cotton. Star shaped polymers : a model for the conformation and its concentration dependence. *Journal de Physique*, 43(3):531–538, 1982.

[127] M. Daoud and J. F. Joanny. Conformation of branched polymers. *Journal de Physique*, 42(10):1359–1371, 1981.

[128] Bruno H. Zimm and Walter H. Stockmayer. The dimensions of chain molecules containing branches and rings. *The Journal of Chemical Physics*, 17(12):1301–1314, Dec 1949.

[129] G. R. Dobson and M. Gordon. Configurational statistics of highly branched polymer systems. *The Journal of Chemical Physics*, 41(8):2389–2398, Oct 1964.

[130] Paul J. Flory. *Principles of polymer chemistry*. Cornell University Press, 1953.

[131] Pierre-Gilles De Gennes and Pierre-Gilles Gennes. *Scaling concepts in polymer physics*. Cornell university press, 1979.

[132] Yuwei Shan, Yingguo Li, Di Huang, Qingjun Tong, Wang Yao, Wei-Tao Liu, and Shiwei Wu. Stacking symmetry governed second harmonic generation in graphene trilayers. *Science Advances*, 4(6):eaat0074, Jun 2018.

[133] Babji Srinivasan, Thi Vo, Yugang Zhang, Oleg Gang, Sanat Kumar, and Venkat Venkatasubramanian. Designing DNA-grafted particles that self-assemble into desired crystalline structures using the genetic algorithm. *Proceedings of the National Academy of Sciences of the United States of America*, 110(46):18431–18435, Nov 2013.

[134] Teng Huang, Qiang Zhao, Junyan Xiao, and Limin Qi. Controllable self-assembly of PbS nanostars into ordered structures: close-packed arrays and patterned arrays. *ACS Nano*, 4(8):4707–4716, Aug 2010.

[135] Yulian Liu, Kerong Deng, Jun Yang, Xiaotong Wu, Xiaokun Fan, Min Tang, and Zewei Quan. Shape-directed self-assembly of nanodumbbells into superstructure polymorphs. *Chemical Science*, 11(16):4065–4073, 2020.

[136] Qian Wang, Zongpeng Wang, Zhe Li, Junyan Xiao, Hangyong Shan, Zheyu Fang, and Limin Qi. Controlled growth and shape-directed self-assembly of gold nanoarrows. *Science Advances*, 3(10):e1701183, Oct 2017.

[137] Maowei Jiang and Xiaogang Peng. Anisotropic Fe3O4/Mn3O4 hybrid nanocrystals with unique magnetic properties. *Nano Letters*, 17(6):3570–3575, Jun 2017.

[138] Zewei Quan, Hongwu Xu, Chenyu Wang, Xiaodong Wen, Yuxuan Wang, Jinlong Zhu, Ruipeng Li, Chris J Sheehan, Zhongwu Wang, Detlef-M Smilgies, Zhiping Luo, and Jiye Fang. Solvent-mediated self-assembly of nanocube superlattices. *Journal of the American Chemical Society*, 136(4):1352–1359, Jan 2014.

[139] Yasutaka Nagaoka, Rui Tan, Ruipeng Li, Hua Zhu, Dennis Eggert, Yimin A. Wu, Yuzi Liu, Zhongwu Wang, and Ou Chen. Superstructures generated from truncated tetrahedral quantum dots. *Nature*, 561(7723):378–382, Sep 2018.

[140] Milena P. Arciniegas, Mee R. Kim, Joost De Graaf, Rosaria Brescia, Sergio Marras, Karol Miszta, Marjolein Dijkstra, René van Roij, and Liberato Manna. Self-assembly of octapod-shaped colloidal nanocrystals into a hexagonal ballerina network embedded in a thin polymer film. *Nano Letters*, 14(2):1056–1063, Feb 2014.

[141] Karol Miszta, Joost de Graaf, Giovanni Bertoni, Dirk Dorfs, Rosaria Brescia, Sergio Marras, Luca Ceseracciu, Roberto Cingolani, Ren van Roij, Marjolein Dijkstra, and Liberato Manna. Hierarchical self-assembly of suspended branched colloidal nanocrystals into super-lattice structures. *Nature Materials*, 10(11):872–876, Sep 2011.

[142] Zihao Ou, Ziwei Wang, Binbin Luo, Erik Luijten, and Qian Chen. Kinetic pathways of crystallization at the nanoscale. *Nature Materials*, 19(4):450–455, Apr 2020.

[143] Elena V. Shevchenko, Dmitri V. Talapin, Christopher B. Murray, and Stephen O'Brien. Structural characterization of self-assembled multifunctional binary nanoparticle superlattices. *Journal of the American Chemical Society*, 128(11):3620–3637, Mar 2006.

[144] Zhuoying Chen and Stephen O'Brien. Structure direction of II-VI semiconductor quantum dot binary nanoparticle superlattices by tuning radius ratio. *ACS Nano*, 2(6):1219–1229, Jun 2008.

[145] Taejong Paik and Christopher B. Murray. Shape-directed binary assembly of anisotropic nanoplates: a nanocrystal puzzle with shape-complementary building blocks. *Nano Letters*, 13(6):2952–2956, Jun 2013.

[146] Andrea Castelli, Joost de Graaf, Mirko Prato, Liberato Manna, and Milena P. Arciniegas. Tic-tac-toe binary lattices from the interfacial self-assembly of branched and spherical nanocrystals. *ACS Nano*, 10(4):4345–4353, Apr 2016.

[147] Xingchen Ye, Jaime A. Millan, Michael Engel, Jun Chen, Benjamin T. Diroll, Sharon C. Glotzer, and Christopher B. Murray. Shape alloys of nanorods and nanospheres from self-assembly. *Nano Letters*, 13(10):4980–4988, Oct 2013.

[148] Taejong Paik, Benjamin T Diroll, Cherie R. Kagan, and Christopher B. Murray. Binary and ternary superlattices self-assembled from colloidal nanodisks and nanorods. *Journal of the American Chemical Society*, 137(20):6662–6669, May 2015.

[149] Yunan Gao, Mark C. Weidman, and William A. Tisdale. CdSe nanoplatelet films with controlled orientation of their transition dipole moment. *Nano Letters*, 17(6):3837–3843, Jun 2017.

[150] Jinjie Hao, Yanzhao Yang, Fenghua Zhang, Zhijie Yang, and Jingjing Wei. Faceted colloidal au/fe3 o4 binary supracrystals dictated by intrinsic lattice structures and their collective optical properties. *The Journal of Physical Chemistry C*, 124(27):14775–14786, Jul 2020.

[151] Yuchi Yang, Biwei Wang, Xiudi Shen, Luyin Yao, Lei Wang, Xiao Chen, Songhai Xie, Tongtao Li, Jianhua Hu, Dong Yang, and Angang Dong. Scalable assembly of crystalline binary nanocrystal superparticles and their enhanced magnetic and electrochemical properties. *Journal of the American Chemical Society*, 140(44):15038–15047, Nov 2018.

[152] Yaoting Wu, Siming Li, Natalie Gogotsi, Tianshuo Zhao, Blaise Fleury, Cherie R. Kagan, Christopher B. Murray, and Jason B. Baxter. Directional carrier transfer in strongly coupled binary nanocrystal superlattice films formed by assembly andin situ ligand exchange at a liquidair interface. *The Journal of Physical Chemistry C*, 121(8):4146–4157, Mar 2017.

[153] Mehdi B. Zanjani and Jennifer R. Lukes. Shape- and structure-based phonon bandgap tuning with nanocrystal superlattices. *The Journal of Physical Chemistry C*, 119(29):16889–16896, Jul 2015.

[154] Diego Mendez-Gonzalez, Sonia Melle, Oscar G Calderón, Marco Laurenti, E Cabrera-Granado, Ana Egatz-Gómez, Enrique López-Cabarcos, Jorge Rubio-Retama, and Elena Díaz. Control of upconversion luminescence by gold nanoparticle size: from quenching to enhancement. *Nanoscale*, 11(29):13832–13844, Aug 2019.

[155] Matteo Cargnello, Aaron C Johnston-Peck, Benjamin T. Diroll, Eric Wong, Bianca Datta, Divij Damodhar, Vicky V. T. Doan-Nguyen, Andrew A. Herzing, Cherie R. Kagan, and Christopher B. Murray. Substitutional doping in nanocrystal superlattices. *Nature*, 524(7566):450–453, Aug 2015.

[156] Ya-Wen Zhang, Xiao Sun, Rui Si, Li-Ping You, and Chun-Hua Yan. Single-crystalline and monodisperse LaF3 triangular nanoplates from a single-source precursor. *Journal of the American Chemical Society*, 127(10):3260–3261, Mar 2005.

[157] Tomer Lewi, Hayden A. Evans, Nikita A. Butakov, and Jon A. Schuller. Ultrawide thermo-optic tuning of PbTe meta-atoms. *Nano Letters*, 17(6):3940–3945, Jun 2017.

[158] Steven N Girard, Jiaqing He, Xiaoyuan Zhou, Daniel Shoemaker, Christopher M. Jaworski, Ctirad Uher, Vinayak P Dravid, Joseph P. Heremans, and Mercouri G. Kanatzidis. High performance na-doped PbTe-PbS thermoelectric materials: electronic density of states modification and shape-controlled nanostructures. *Journal of the American Chemical Society*, 133(41):16588–16597, Oct 2011.

[159] Da Wang, Michiel Hermes, Ramakrishna Kotni, Yaoting Wu, Nikos Tasios, Yang Liu, Bart de Nijs, Ernest B. van der Wee, Christopher B. Murray, Marjolein Dijkstra, and Alfons van Blaaderen. Interplay between spherical confinement and particle shape on the self-assembly of rounded cubes. *Nature Communications*, 9(1):2228, Jun 2018.

[160] Ye Tian, Julien R. Lhermitte, Lin Bai, Thi Vo, Huolin L Xin, Huilin Li, Ruipeng Li, Masafumi Fukuto, Kevin G. Yager, Jason S. Kahn, Yan Xiong, Brian Minevich, Sanat K. Kumar, and Oleg Gang. Ordered three-dimensional nanomaterials using DNA-prescribed and valence-controlled material voxels. *Nature Materials*, Jan 2020.

[161] Alexander Stukowski. Visualization and analysis of atomistic simulation data with OVITO-the Open Visualization Tool. *Modelling and Simulation in Materials Science and Engineering*, 18(1), Jan 2010.